

**Application of Ground Penetrating Radar in Delineating
Zones of Gold Mineralization at the Subenso-North
Concession of Newmont Ghana Gold Limited**

by

MANU EVANS, B.Sc (Hons) PHYSICS

**A Thesis Submitted to the Department of Physics,
Kwame Nkrumah University of Science and Technology
in partial fulfillment of the requirements for the degree**

of



MASTER OF SCIENCE (GEOPHYSICS)

College of Science

© Department of Physics

August, 2011

Abstract

Ground penetrating radar (GPR) survey was conducted over the Subenso-north gold deposit a property of Newmont Ghana Gold Ltd. (NGGL) to delineate fractures which are possible gold hosting structures. The Mala GPR equipment with 25 and 50 MHz rough terrain antennae frequencies were used to conduct the survey. The Maximum exploration depth of approximately 925 ns corresponding to 50 m was probed. The survey was conducted over a 1 km square block with a total of 21 profiles with a 50 m profile interval. The profiles were in the direction of north-west - south-east. The common offset data collection mode was used. This technique allowed the collection of useful geologic data, for example the upper duracrust which overlain the thick saprolite was imaged with an average thickness between 0 m and 8 m. Different radar responses were also obtained from the saprolite indicating the presence of highly weathered zones where complete oxidation includes all of the saprolite. Two sets of inferred structural patterns were established. The structural patterns were S1 and S2 . The S1 inferred structures were found between the depth range of (12 m and 42 m) and the S2 also between (31 m and 48 m) for 25 MHz RTA. 50 MHz RTA also recorded S1 structures at the depth range of (14 m and 34 m) and that of the S2 at the depth range of (27 m and 38 m). These sets of inferred structures are potential zones of gold mineralization.

Contents

Declaration	i
Abstract	ii
List of Tables	viii
List of Figures	xiv
List of Symbols and Acronyms	xv
Acknowledgements	xvi
1 Introduction	1
1.1 Research Problem Definition	5
1.2 Objectives of the Research	6
1.3 Justification of the Objectives	6
1.4 Location and Accessibility	7
1.5 Physiographic Settings and Climate	8
1.6 Vegetation and Occupation of Inhabitants	10
1.7 Structure of the Thesis	10
2 Geological Settings	12

2.1	Regional Geology	12
2.1.1	The Birimian Rock System	14
2.1.2	Tarkwaian Rock System	15
2.1.3	The Sefwi Gold Belt	16
2.1.4	Birimian-Hosted Gold Mineralization	18
2.1.5	Tarkwaian-Hosted Gold Mineralization	19
2.2	Local Geology	19
2.2.1	Geology of the Survey Site (Subenso-North Prospect)	19
2.2.2	Subenso Style Gold Mineralization	23
2.2.3	Subenso Weathered Lithologies	24
2.2.4	Subenso Gold Mineralization	25
3	Theoretical Background of the Ground Penetrating Radar Technique	26
3.1	Fundamental Theory of Ground Penetrating Radar	26
3.2	Fundamentals of Electromagnetic Wave Propagation	26
3.3	Basic Wave Properties	27
3.3.1	Maxwell's Equations	27
3.3.2	Constitutive Equations	28
3.4	Reflection and Refraction of Electromagnetic Waves	33
3.5	Ground Penetration Radar Resolution	40
3.6	Scattering Attenuation of GPR Waves	42
3.7	Propagation Dispersion of GPR Waves	44
3.8	Dielectric Properties of Geological Materials	45
3.9	Ground Penetrating Radar Surveys	49
3.9.1	Common-Offset Reflection Survey	49

3.9.2	Multi-offset Common Midpoint/Wide-Angle Reflection and Refraction	
	Velocity Sounding Survey	50
3.9.3	Transillumination Surveys	50
3.10	Noise sources that could Preclude the Use of GPR	51
4	MATERIALS AND METHODS	52
4.1	Site Description	52
4.1.1	Equipment for the GPR Survey	54
4.1.2	Measurement Parameters	55
4.1.3	GPR Data Processing and Presentation	57
4.1.3.1	Data/Trace Editing	58
4.1.3.2	Dewow Filtering	59
4.1.3.3	Time-Zero Correction	59
4.1.3.4	Velocity Analysis and Depth Conversion	60
4.1.3.5	Background Removal	61
4.1.4	Time Gain	62
5	RESULTS AND DISCUSSION	63
5.1	Interpretation of Field Results	63
5.1.1	GPR Results from 25 MHz RTA Antenna	63
5.1.1.1	Traverse 1: Line 2000E/3000N	63
5.1.1.2	Traverse 2: Line 2050E/2000N	66
5.1.1.3	Traverse 3: Line 2100E/3000N	66
5.1.1.4	Traverse 4: Line 2150E/2000N	69
5.1.1.5	Traverse 5: Line 2200E/3000N	69
5.1.1.6	Traverse 6: Line 2250E/2000N	71

5.1.1.7	Traverse 7: Line 2300E/3000N	74
5.1.1.8	Traverse 8: Line 2350E/2000N	74
5.1.1.9	Traverse 9: Line 2400E/3000N	77
5.1.1.10	Traverse 10: Line 2450E/2000N	77
5.1.1.11	Traverse 11: Line 2500E/3000N	80
5.1.1.12	Traverse 12: Line 2550E/2000N	80
5.1.1.13	Traverse 13: Line 2600E/3000N	83
5.1.1.14	Traverse 14: Line 2650E/2000N	83
5.1.1.15	Traverse 15: Line 2700E/3000N	86
5.1.1.16	Traverse 16: Line 2750E/2000N	86
5.1.2	Results of 50 MHz Antenna	89
5.1.2.1	Traverse 1: Line 2000E/3000N	91
5.1.2.2	Traverse 2: Line 2050E/2000N	91
5.1.2.3	Traverse 2: Line 2100E/3000N	94
5.1.3	Interpretation of Inferred S2 Structures Hosting Gold Mineralization for 25 MHz RTA	95
5.1.3.1	Interpretation of Inferred S2 Structural Depth Run for 25 MHz RTA	95
5.1.4	Correlating GPR Results with Chargeability and Resistivity Results	97
6	CONCLUSION AND RECOMMENDATIONS	101
6.1	Conclusion	101
6.2	Recommendations and Outlook	103
	Bibliography	103

A		109
A.1	Ground Penetrating Radar Profile Images For 50 MHz RTA	109
A.1.1	Traverse 3: Line 2150E/2000N	111
A.1.2	Traverse 4: Line 2200E/3000N	111
A.1.3	Traverse 5: Line 2250E/2000N	114
A.1.4	Traverse 6: Line 2300E/3000N	114
A.1.5	Traverse 7: Line 2350E/2000N	117
A.1.6	Traverse 9: Line 2450E/2000N	117
A.1.7	Traverse 10: Line 2500E/3000N	120
A.1.8	Traverse 11: Line 2550E/2000N	120
A.1.9	Traverse 12: Line 2600E/3000N	123
A.1.10	Traverse 13: Line 2650E/2000N	123
A.1.11	Traverse 14: Line 2700E/3000N	125
A.2	Interpretation of inferred S1 structural depth run for 25 MHz RTA	127
A.3	Interpretation of inferred S2 structural depth run for 50 MHz RTA	129
B		134
B.1	Used Software	134

List of Tables

3.1 Attenuation and relative permittivity of subsurface material measured at 100 MHz (Daniels, 1996)	48
--	----

KNUST



List of Figures

1.1	Location map of Subenso-North gold deposit (modified after Cees; (2006))	8
1.2	Location map of Subenso-North showing contours and drainage (modified after Cees; 2006)	9
2.1	Geological map of South-Western Ghana showing the various gold belts (after Kesse (1985)).	17
2.2	Geological map of Subenso-North concession (modified after (Cees, 2006))	23
2.3	Typical section through the Subenso style mineralization (modified after (Roland, 2004))	24
3.1	Changes of direction of propagation of radar wave as described by Snell's law.	34
3.2	Illustration of the critical angle of incidence θ_c	36
3.3	Illustration of the behaviour of EM waves at an interface	37
3.4	Typical plot of the reflection coefficient versus the angle of incidence. θ_B is the Brewster angle Mala (2011)	39
3.5	Geometry for determining the range resolution, δr , and the lateral resolution δl Source: Mala (2011)	40
3.6	Normalized scattering cross-section as function of normalized wavelength (Skolnik, 1970)	43

3.7	Estimate of the scattering attenuation as a function of frequency for a medium with 10 scatterers per cubic meter. Each scatterer has the radius 0.1 m (modified from (Mala, 2011))	44
4.1	Map of Subenso-North gold deposit showing the surveyed area ABCD with profile lines (courtesy Newmont Ghana Ltd geophysics department)	53
4.2	MALA GPR equipment used for the survey: A is XV monitor, B is Control unit, C is the RTA	55
4.3	GPR data collection in a continuous mode operation: A is the XV Monitor, B is the control unit and, C is the 100 MHz RTA antenna	56
4.4	Raw unprocessed GPR data from the Newmont's Subenso-north concession	57
4.5	Typical processing flow sequence for 2 D-monostatic common-offset, reflection mode GPR data. (modified after (Hary, 2009))	58
4.6	dewow filter correction on a 100 MHz GPR section	59
4.7	Example of time-zero correction on a 25 MHz RTA GPR section (the top gap in fig 4.6 has been adjusted to the zero level on the time axis	60
4.8	Velocity adaptation by hyperbola (marked A) fitting	61
4.9	GPR data after background removal	62
5.1	Radar Section of profile 2000E/3000N	64
5.2	Inferred structures hosting mineralization of profile 2000E/3000N	64
5.3	Radar Section of profile 2050E/2000N	65
5.4	Inferred structures hosting mineralization of profile 2050E/2000N	65
5.5	Radar Section of profile 2100E/3000N	67
5.6	Inferred structures hosting mineralization of profile 2100E/3000N	67
5.7	Radar Section of profile 2150E/2000N	68

5.8	Inferred structures hosting mineralization of profile 2150E/2000N	68
5.9	Radar Section of profile 2200E/3000N	70
5.10	Inferred structures with potential of hosting gold mineralization of profile 2200E/3000N	70
5.11	Radar Section of profile 2250E/2000N	72
5.12	Inferred structures with potential of hosting gold mineralization of profile 2250E/2000N	72
5.13	Radar Section of profile 2300E/3000N	73
5.14	Inferred structures with potential of hosting gold mineralization of profile 2300E/300N	73
5.15	Radar Section of profile 2350E/2000N	75
5.16	Inferred structures with potential of hosting gold mineralization of profile 2350E/2000N	75
5.17	Radar Section of profile 2400E/3000N	76
5.18	Inferred structures with potential of hosting gold mineralization of profile 2400E/3000N	76
5.19	Radar Section of profile 2450E/2000N	78
5.20	Inferred structures with potential of hosting gold mineralization of profile 2450E/2000N	78
5.21	Radar Section of profile 2500E/3000N	79
5.22	Inferred structures with potential of hosting gold mineralization of profile 2500E/3000N	79
5.23	Radar Section of profile 2550E/2000N	81
5.24	Inferred structures with potential of hosting gold mineralization of profile 2550E/2000N	81

5.25 Radar Section of profile 2600E/3000N	82
5.26 Inferred structures with potential of hosting gold mineralization of profile 2600E/3000N	82
5.27 Radar Section of profile 2650E/2000N	84
5.28 Inferred structures with potential of hosting gold mineralization of profile 2650E/2000N	84
5.29 Radar Section of profile 2700E/3000N	85
5.30 Inferred structures with potential of hosting gold mineralization of profile 2700E/3000N	85
5.31 Radar Section of profile 2750E/2000N	88
5.32 Inferred structures with potential of hosting gold mineralization of profile 2750E/2000N	88
5.33 Radar Section of profile 2000E/3000N	90
5.34 Inferred structures with potential of hosting gold mineralization of profile 2000E/3000N	90
5.35 Radar Section of profile 2050E/000N	92
5.36 Inferred structures with potential of hosting gold mineralization of profile 2050E/2000N	92
5.37 Radar Section of profile 2100E/3000N	93
5.38 Inferred structures with potential of hosting gold mineralization of profile 2100E/3000N	93
5.39 A contour grid of inferred S2 structures for 25 MHz RTA	96
5.40 Local grid of Subenso-north chargeability results (Source: Geophysics section Newmont Ghana Gold Ltd, 2011)	98

5.41	Local grid of Subenso-north resistivity results (Source: Geophysics section Newmont Ghana Gold Ltd, 2011)	99
A.1	Radar section of profile 2150E/2000N	110
A.2	Inferred structures hosting mineralization of profile 2150E/2000N	110
A.3	Radar section of profile 2200E/3000N	112
A.4	Inferred structures hosting mineralization of profile 2200E/3000N	112
A.5	Radar section of profile 2250E/2000N	113
A.6	Inferred structures hosting mineralization of profile 2250E/2000N	113
A.7	Radar section of profile 2300E/3000N	115
A.8	Inferred structures hosting mineralization of profile 2300E/3000N	115
A.9	Radar section of profile 2350E/2000N	116
A.10	Inferred structures hosting mineralization of profile 2350E/2000N	116
A.11	Radar section of profile 2450E/2000N	118
A.12	Inferred structures hosting mineralization of profile 2450E/2000N	118
A.13	Radar section of profile 2500E/3000N	119
A.14	Inferred structures hosting mineralization of profile 2500E/3000N	119
A.15	Radar section of profile 2550E/2000N	121
A.16	Inferred structures hosting mineralization of profile 2550E/2000N	121
A.17	Radar section of profile 2600E/3000N	122
A.18	Inferred structures hosting mineralization of profile 2600E/3000N	122
A.19	Radar section of profile 2650E/2000N	124
A.20	Inferred structures hosting mineralization of profile 2650E/2000N	124
A.21	Radar section of profile 2700E/3000N	126
A.22	Inferred structures hosting mineralization of profile 2700E/3000N	126

A.23 A contour grid of inferred S1 structures for 25 MHz RTA	128
A.24 A contour grid of inferred S2 structures for 50 MHz RTA	130
A.25 A contour grid of inferred S1 structures for 50 MHz RTA	131
A.26 Trend of an inferred S2 structure hosting gold mineralization for 25 MHz RTA	132
A.27 Trend of an inferred S1 structure hosting gold mineralization for 25 MHz RTA	132
A.28 Trend of an inferred S2 structure hosting gold mineralization for 50 MHz RTA	133
A.29 Trend of an inferred S1 structure hosting gold mineralization for 50 MHz RTA	133

KNUST



List of Symbols and Acronyms

σ	electric conductivity	θ_1	angle of incidence
E	Electric field strength	θ_2	angle of refraction
H	Magnetic field intensity	θ_c	critical angle
J	Electric current density	P	Poynting vector
D	Electric displacement	θ_b	Brewster angle
B	Magnetic flux density	W	Pulse width
q	Electric charge density	f_c	center frequency
t	time	B	Bandwidth of GPR system
ϵ	Electric permittivity	λ_c	center wavelength
μ	Magnetic permeability	ϵ_{ef}	effective permittivity
∇	spatial vector derivative	σ_{ef}	effective conductivity
k	wave number	ϵ_T	complex permittivity
ω	angular frequency	R	reflection coefficient
v	velocity of electromagnetic wave	GPR	Ground Penetrating Radar
δ_{skin}	skin depth	TE	Transverse Electric
Q	quality factor	TM	Transverse Magnetic
μ_0	permeability of free space	IP	Induce polarization
μ_r	relative permeability	TEM	Transient Electromagnetic
ϵ_0	permittivity of free space	f_t	transition frequency
ϵ_r	relative permittivity		

Acknowledgments

My first and foremost appreciation goes to the Almighty God for His unending mercies and grace towards me throughout the duration of this work. I am highly indebted to my supervisor Dr. Kwasi Preko for his motivation, encouragement and criticism that helped to improve this work. I say God let His face shine upon you wherever you go. I wish to thank Prof. S K Danuor for his encouragement and motivation. I sincerely thank Mr. Vandycke Asare for the training that he gave me on the GPR equipment as well as all the lecturers in the Physics Department, Mr R.M. Noye, Mr. A.A. Aning, Mr. D.D. Wemegah and Dr. M.K.E. Donkor for the knowledge imparted to me. This work would not have been possible without the support of Newmont Ghana Gold Ltd (NGGL) in the provision of logistics and field assistance. My thanks go to Mr. Thomasi Tsiboah (Exploration Geophysicist, Africa Region NGGL) for granting me the permission to carry out the survey on their property. Mr. Kwaku Takyi-Kyeremeh, Mr. Alfred Agyei Berko, Mr. Sarfo Kantanka (Geologists) (all at NGGL) are also thanked for their unflinching support. Many thanks also go to Mr. Amono Parker Benjamin (Geophysics Technician, KNUST) and Worlanyo Ablordeppye for their support during data collection. I thank my course mates: Isaac Coffie Sonful, Peter Kuffour, Frederick and Elizabeth Von-Kiti for the shared knowledge and companionship. My final thanks go to My Sweet Mum Cecilia Arye, Mr. Benard Anto Arye, Kwame Manu and all my family members. I really appreciate your support both physical and spiritual.

CHAPTER 1

Introduction

In recent years, mineral exploration especially gold in Ghana has been on the increase, as a result of favorable investment climate created by the government by Act 437-the investment code of 1981 (Kesse, 1985). This code is perhaps in the best interest of the country, to encourage and promote large scale investments in the exploration, exploitation and processing of mineral resources of the country. The use of Geophysical methods in mineral exploration in Ghana is not widespread. Most mining companies after undertaking geochemical sampling (stream sediments and soil sampling) move in to drill the geochemical anomalies without necessarily employing the services of a Geophysicist.

One of the mining companies in Ghana which use the geophysical tools to aid targeting of gold deposit in Ghana is the Newmont Ghana Gold Limited. The Newmont Ghana Geophysical crew has embarked on a number of surveys in ground magnetic, induce polarization, 3-D resistivity, transient electromagnetic (TEM) and ground gravity measurements in the search of economic gold deposits. The Gravity, Magnetic and Resistivity methods have been extensively used on the major Gold belts of Ghana. Surveys have been conducted on the Ashanti belt (Tepa, Subriso and Sabronum etc. all in the Ashanti Region), Sefwi Belt (Kenyase, Sefwi Bekwai, and Sefwi Bodi etc), Kibi- Winneba belt and the Lawra Belt (Wa, Dorimon, Nadoli etc.). Other contracted exploration companies like Goanna Exploration from Australia have carried out a lot of IP/Resistivity surveys in Ghana.

Extensive Geophysical works are still on going in parts of Ghana mainly for the search of economic Gold deposits. Among the numerous geophysical methods which the Newmont Ghana Gold Ltd uses for its exploration works, the GPR method has become elusive and has never been used on any of Newmont's concessions in Ghana.

Ground penetrating radar is a nondestructive geophysical method that produces a continuous cross-sectional profile or record of subsurface features, without drilling, probing, or digging. GPR profiles are used for evaluating the location and depth of buried objects and to investigate the presence and continuity of natural subsurface conditions and features.

GPR operates by transmitting pulses of ultra high frequency radio waves (microwave electromagnetic energy) down into the ground through a transducer or antenna. The transmitted energy is reflected from various buried objects or distinct contacts between different earth materials depending on their dielectric contrasts. As a technique for probing visually opaque dielectric media, subsurface radar has been used successfully in a wide variety of operations.

The long range applications of subsurface radar can involve distances of many hundreds of meters. In general, the frequencies involved have been between 10 MHz to 1 GHz for different resolutions of subsurface materials. Much of the long-range radar probing work has been carried out by academic establishments and research organizations.

Davis et al. (1984) carried out a number of surveys, both from the surface and from boreholes, to map geological structures. Geophysical Survey Systems Incorporated (GSSI) radar was modified and used to map the depth of bedrock to 25 m, the groundwater table and variations in soil strata. These authors have also investigated permafrost.

Cagnoli and Russel (2000), carried out a GPR survey to collect subsurface images of the basaltic base surge deposits in the Ubehebe hydrovolcanic field, Death Valley National Park, California. Antennae frequencies of 50, 100 and 200 MHz were used. This survey revealed that, the GPR technique could image the lower stratigraphic boundary of the pyroclastic deposits and its thickness.

Carlos da Silva et al. (2004) used Resistivity and GPR as an integrated approach to image fractures present in crystalline aquifer. In a case study in Caicara farm-NE Brazil, combined interpretation of geophysical images (Resistivity and GPR) and field structural geologic data revealed that the fractured bedrock aquifer composed of three sets of discontinuities. These are NS-dipping sub-horizontal joints parallel to the ductile fabric of the country rocks which are probably release joints, NE-dipping sub-horizontal fractures, oblique to ductile trend and sub-vertical fractures which are orthogonally distributed along N-S and E-W directions.

(Slater and Tina Niemi, 2003) embarked on research which aimed at locating a major active fault that traverses Aqaba City in Jordan by the application of GPR technique. Measurements over an exposed (trenched) cross fault outside of the City revealed a radar signature which consisted of linear events and horizontal offset/flexured reflectors both showing a geometric correlation with known faults at a central site.

Leucci (2006) investigated the cavity and fractures under the main Church in Botrugno (Lecce, Italy) by the contribution of ground penetrating radar and electrical resistivity tomography. The GPR analysis revealed the high electromagnetic (EM) energy attenuation (almost surely due to the presence of water filling the subsoil and the pavement). Despite the EM energy attenuation, the processing and interpretation of GR data pointed out the presence of voids and fractures under the main Church.

Work by Bishop et al. (1980) resulted in probing the Antinuclear icecap in Iceland to a depth of 600 m using a 2 MHz radiation transmitted from a 60 m resistively loaded wire antennas.

Ulriksen (1982) in a thesis submitted to the Lund University of Technology and subsequently published by GSSI, describes a number of investigations in Sweden of sand, gravel, peat, rock, fresh water, ice and snow. Using GSSI radar he found that in homogeneous materials like peat, excellent determination of depth and included objects was achieved.

Leggo and Leech (1983) described work carried out to investigate the feasibility of using radar to detect voids and cavities. Using ISSI radar, two backfield mine shafts and a test site of horizontal cavities were investigated. The conclusion was that subsurface exploration using radar was feasible in many sites in the UK but more research was needed in the interpretation of the results. The use of GPR in engineering, archeology and surface environmental geological studies is well documented and highly effective, (Pilon (1992); Conyers and Goodman (1998); Noon et al. (2000)). However, applications of the technique in crystalline rocks have been primarily devoted to delineating cracks for engineering applications or nuclear waste storage facilities. (Grasmueck (1996); Holloway (1992); Olsson et al. (1992)). Direct application in hard rock mining has been conducted for the past 30 years, but scientific publication of this effort is limited or has been relegated to the dust bin. Identification of mineralized zones, in granitic rocks for example, has been somewhat elusive (Lees, 1998).

It is based on this premise that, GPR has been proposed as an alternative geophysical tool for delineating gold mineralization zones at the Subenso north concession of Newmont Ghana Gold Limited. The results of the GPR measurements will be interpreted and together with the resistivity and chargeability results derive the maximum information about the trend of

gold mineralization at the study site.

1.1 Research Problem Definition

In many areas in the world where geophysical prospecting works are carried out by mining companies, the ground based GPR technique has been relegated to the dust bin. Scientific publications on the use of GPR application on hard crystalline granitic rocks, for locating mineralized zones have received less attention by many researchers and mineral prospectors. This situation constitutes a problem in predicting whether the GPR method is capable of delineating zones of gold mineralization or not. In this study, it is hypothesized that ground base GPR method could give a better underground image in delineating zones of gold mineralization in hard crystalline rock formations at the Subenso north gold deposit within the Sefwi gold belt of Ghana.

The justification for this hypothesis is that, gold mineralization in the Subenso concession is hosted in the breccia unit. On the other hand the breccia unit is also sandwiched between sedimentary basin and the volcanic belt. Due to the high dielectric contrast between the sedimentary rock formation and the volcanic rock formation, it is highly possible for the radar waves to image the transition zones where mineralization occurs.

Furthermore, the gold mineralization which is located at depth outcrops to the surface as secondary gold mineralization. The saprolite can be considered as the area where the secondary gold mineralization occurs. Since mineralization in the Ahafo area is structure controlled, the possible regions where the gold mineralization occurs are the structures within the saprolite formation. In view of this, the radar waves will be able to delineate

the various structures hosting the gold mineralization at the Subenso-north concession of Newmont Ghana Gold Ltd.

1.2 Objectives of the Research

The main objective of this research is to map possible structures that host gold mineralization at a more affordable cost. The research is, however, conducted with the following additional objectives in mind:

- To validate the GPR technique as efficient and appropriate for mineral exploration.
- To confirm the already mapped zones of gold mineralization by the Newmont Ghana gold limited.
- Obtain the necessary information on the mineralization potential of the overburden saprolite in the Subenso-north concession of Newmont Ghana Gold Ltd.

1.3 Justification of the Objectives

The historical importance of mining in the economic development of Ghana is considerable and well documented, with the country's colonial name Gold Coast reflecting the importance of the mining sector. Gold dominates the mining sector and Ghana is the second most important producer of gold after South Africa in Africa (Akabzaa and Darimani, 2001). Among the numerous natural resources that Ghana is endowed with, gold is the mineral which renders much support to the country's economy (Akabzaa and Darimani, 2001). It

is clear to state that, Ghana's economy is dependent on the foreign exchange earnings from which the gold sector is a major contributor. It is based on this premise that this work has proposed an alternative method for exploring gold deposits on the major gold belts in Ghana.

Furthermore, the continued expansion in the demand for metals of all kinds and the enormous increase in the use of petroleum products since the turn of the century have led to the development of many geophysical techniques of ever increasing sensitivity for the detection and mapping of the unseen deposits and structures (Telford et al., 1990). The Newmont Ghana Gold Ltd has carried out geophysical survey on the Subenso-north concession by the following methods: Gravity, Magnetic, IP/Resistivity (both 3-D and gradient array) and Transient Electromagnetic methods. The aforementioned methods are more costly to the company for just reconnaissance survey and based on that, there is therefore the need to find alternative methods and techniques that will aid in the discovery of this important mineral at a lower cost and effective as the other methods.

1.4 Location and Accessibility

The Subenso North gold deposit is located between Teekyere and Adroba in the Brong Ahafo region of Ghana and about 300 km northwest of Accra. Road access to the project site is via bitumen sealed road from Accra to Sunyani through Kumasi. The main town in the area is Teekyere which is located just by the road side about 2.5 km from Duayaw Nkwanta from Bechem Junction off Sunyani road. About 1 km to the south of the deposit and almost parallel to the strike is a feeder road which connects two main towns in the area, Teekyere on the south and Adroba on the north.

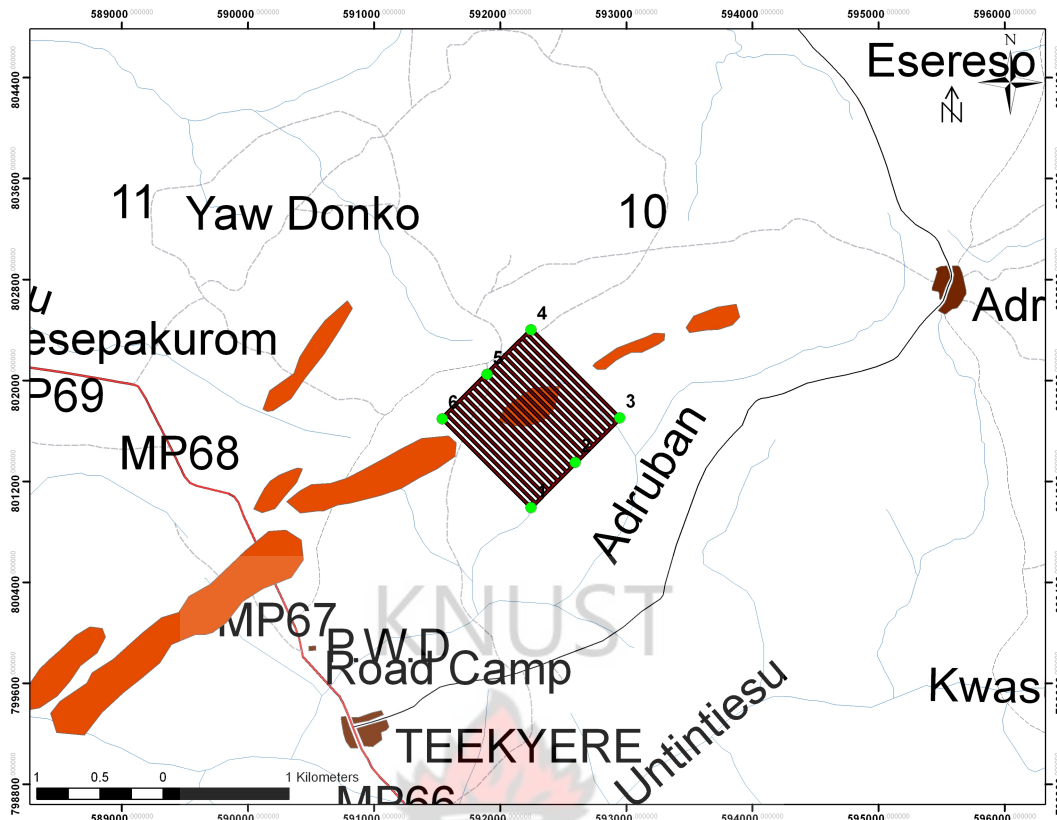


Figure 1.1: Location map of Subenso-North gold deposit (modified after Cees; (2006))

1.5 Physiographic Settings and Climate

The Project area comprises low rounded hills with elevations ranging from 291 m to 326 m above mean sea level. Seasonal streams and tributaries of the Tano River basin drain the broad, relatively flat valleys. The Ahafo Project Area falls within the wet semi-equatorial climatic zone of Ghana and is characterized by an annual maximum rainfall pattern occurring in the months of May to July and from September to October. The climate of the area is determined by movement of air masses which differ in air moisture and relative stability rather than temperature (Newmont, 2007).

The two air masses, namely the southwest monsoon and the northeast trade winds, come into contact along the Inter-Tropical Convergence Zone (ITCZ). The ITCZ which passes

over the area twice yearly is responsible for the annual succession of seasons. The northern air masses locally called "Harmattan" coming from the sub-tropical Azores anticyclone and its extension over the Sahara Desert bring hot and dry weather in December, January, and February (Newmont, 2008b). Mean annual rainfall for the Project area is between 1354 and 1400 mm (Newmont, 2008a). Typically, minimal rainfall is experienced from December to the end of February, with January as the driest month. Mean monthly temperatures within the area range from 23.9 to 28.4 °C.

In general, March is the hottest month of the year with a mean temperature of 27.8 °C. August is the coolest month with a mean temperature of 24.6 °C (Newmont, 2009). The rainy season is characterized by humid conditions. This is particularly so during the night, when 95 to 100 % humidity is possible. During the Harmattan season however, humidity drops to as low as 25 % (Newmont, 2009).

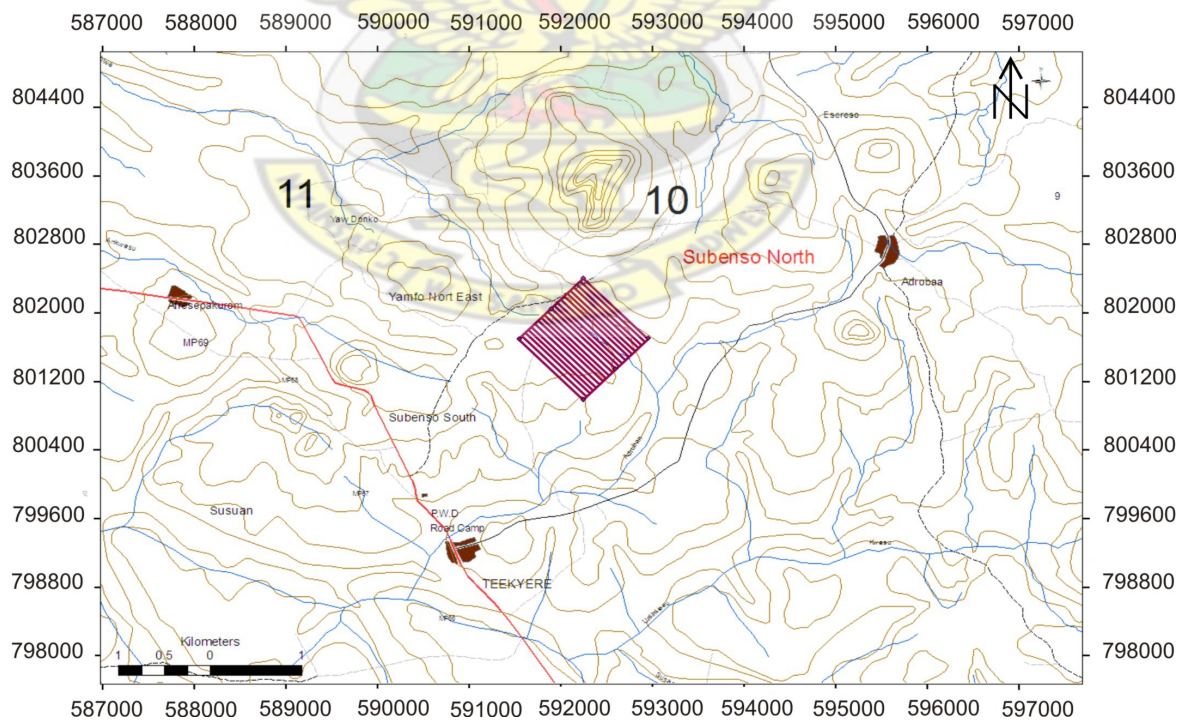


Figure 1.2: Location map of Subenso-North showing contours and drainage (modified after Cees; 2006)

1.6 Vegetation and Occupation of Inhabitants

Vegetation in the Project area is composed of a mixture of natural plant communities in early stages of ecological succession, crops, and plantations, patches of second growth forest, and riparian communities along rivers and streams. The natural vegetation in the Project area has been extensively fragmented as a result of agricultural activities, fire, and removal of timber and, consequently, has little resemblance to the native forest communities once typical of the region. Following extensive nation-wide fires in 1983, areas previously dominated by trees and shrubs have been taken over by dense stands of elephant grass (Newmont, 2006). The Project area consists primarily of subsistence farms with small-scale commercial farming intermingled with areas of forest regrowth and remnants of secondary forest. The major agricultural land uses are cocoa, teak plantation, food crop and rice farming.

1.7 Structure of the Thesis

The Thesis work has six (6) chapters with each chapter addressing a main heading. Chapter one introduces the subject matter, outlining the background of the research, objectives of the research, justification of the objectives of the research, location and accessibility of the research area, physiographic settings, climate as well as the vegetation and occupation of inhabitants of the research area.

Chapter two gives the general overview of the geological settings of the study area. It reviews both the regional and local geology of the study area.

Chapter three outlines the main fundamental theory behind the GPR technology, taking into

account the history behind the application of GPR.

Chapter four gives an overview of the method used in carrying out the thesis work. This chapter also outlines the processing steps employed in the data processing.

Chapter five analyses the various radar sections for the profiles. Interpretations to the radar sections are also given in this chapter. Finally, this chapter correlate the GPR results with the chargeability and resistivity results of the study area.

Chapter six draws conclusions from the research and makes recommendations for future works to be embarked on.



CHAPTER 2

Geological Settings

2.1 Regional Geology

Regionally, Ghana is broadly divided into four (4) main geotectonic units. Each unit is associated with a particular mineral deposit. The West African Cratonic area which covers the western half of the country is made up of two (2) formations: the Birimian and the Tarkwaian (Kesse, 1985). On the regional structure elements only carry gold mineralization if they are developed within the zone of the auriferous chemical sediments; those outside the zone tend to be barren. Gold mineralization in Ghana is reported to consist of three main types:

- Reef, vein or lode type
- Auriferous quartz pebble conglomerates and
- Recent alluvial and eluvial deposits associated with the rocks of these two systems.

The most striking feature of the geology of Ghana is the parallel disposition of evenly spaced belts of folded Birimian metalavas. The belt is 40 km to 50 km, the distance between individual belts is approximately 90 km and the belts generally trend northeasterly. They consist of lava flows that are separated by basins containing metasedimentary granitoids in

different proportions. Sediments between belts consist of volcanoclastic (pyroclastics and epiclastic) and volcano rocks which are derived from volcanoes of the belt.

Auriferous quartz-pebble conglomerates within the Tarkwaian system are exposed in the Tarkwa area. The Tarkwaian is clastic sedimentary rock deposited in an elongated basin and is the second largest source of gold in Ghana. The gold deposits are fossil placer deposits the mineralization that remobilized may represent detrital gold weathered out of the mineralized Birimian Rocks. The Tarkwaian rocks occur in two well defined and one smaller north easterly aligned belts. The main belt, lying immediately east of the main Prestea-Obuasi Birimian zone, extends from near the coast to the south of Tarkwa about 250 km to the northeast where it terminates at the edge of the voltaian basin. The main Tarkwaian belt has an average width of 16 km. It is believed that the Tarkwaian Banket series was deposited in a braided stream channel environment beyond from the primary vein and lode-type deposits in the underlying Birimian (Kesse, 1985). Another belt of similar rocks occurs in west central Ghana near Banda, and smaller occurrences exist to the north and south of Bibiani and Kibi. The reef, vein or lode type of gold deposit is associated with the rocks of the Birimian system and has played a dominant role in the gold industry of Ghana.

The auriferous quartz veins have been the most important source of gold in Ghana, and occur as intrusive veins in phyllites and greenstones within the Birimian system (Kesse, 1985). Gold may be free or contained within sulphide of pyrite and arsenopyrite. The quartz veins containing economic concentrations of gold are usually fractured and shattered and readily disintegrate on weathering. Sulphide ores within Birimian rocks usually consisting of tuffaceous argillites have also proved to be important sources of gold mineralization in Ghana. These are associated with dissemination and the stringers of pyrite and arsenopyrite. The styles of gold mineralization differ among rock system. Birimian deposits are epigenetic

gold quartz vein deposit-type associated with disseminated sulphides in fractured and sheared zones. Tarkwaian gold on the other hand is the Paleoplacer Banket conglomerates of the Witwatersrand-type (Dzigbodi-Adjima, 1992).

2.1.1 The Birimian Rock System

The rocks of the Birimian System deposited upon an unknown Archean (Liberian) basement underlie nearly one-sixth of the total area of Ghana. They crop out in areas to the north, west and southern parts of the country. The Birimian has been folded, metamorphosed and in places assimilated by granitoid bodies. The folding is intense with dips commonly on the order of 30 °-90 ° along a NE-SW axis and of 70 °-90 ° being more common than shallow dips (Kesse, 1985).

The metamorphism has generally been termed "low-grade" greenschist facies. Kesse (1985), however, points out that metamorphism to amphibolites facies is common and grades, up to granulite facies, have been observed in several localities. Faulting tends to follow the strike of the folds and also trends perpendicular to the latter. Jointing in these rocks has many orientations, but most commonly is parallel to fold and fault directions and in north-south direction (Kesse, 1985).

The Birimian rocks have been intruded by granitoids during the later stages of the Eburnean orogeny at or after the end of the Birimian deposition. In terms of mineral deposits, the Birimian rocks are the most important in Ghana for minerals such as gold, diamond, bauxite, manganese and iron are all associated with this System. Just to mention a few, the following are some of the gold belts which are associated with the Birimian rocks:

1. Prestea belt
2. Akropong belt
3. Obuasi belt
4. Sefwi belt
5. Tokosea and Bibiani belts

Most Ghanaian Birimian gold occurrences and mines are concentrated in narrow 'corridors' of 10-15 km width in the transition zone between volcanic belts and sedimentary basins, as are the chemical facies and regionally extensive shear zones at the volcanics-sediment interface. Birimian gold in Ghana is present as two major types: (1) the disseminated sulphide type which is generally lithofacies controlled, i.e. controlled by chemical sediments, and to a lesser extent by selvages of gold-quartz veins; and (2) the quartz vein type which is exclusively structure controlled (Leube et al., 1990).

2.1.2 Tarkwaian Rock System

Rocks of the Tarkwaian System are concentrated mainly at the south-western part of Ghana in the Tarkwa area where they outcrop in a northeast-southwest trending belt. The Tarkwaian rocks consist of thick series of argillaceous and arenaceous sediments (mainly arenaceous) in the lower members of the System. In Ghana, the Tarkwaian is considered to be of shallow water continental origin derived from the Birimian and associated granitoids (Junner, 1935). It is believed that the rocks were deposited in elongated intracratonic rift basins bordered by granite-greenstone belts of the Birimian System. The Tarkwaian is thought to rest

unconformably on the Birimian, though in some places, the Birimian and the Tarkwaian are interfolded due to the post-Tarkwaian orogenic activity (Junner, 1935).

2.1.3 The Sefwi Gold Belt

The Sefwi Belt is a 40-60 km wide typical Birimian volcanic belt, striking 220 km in Ghana and extends SW to the coast in La Cote d'Ivoire. It is located north of, and parallel to, the prolific Ashanti Gold Belt, which hosts many of Ghana's active producing gold mines. The Sefwi Belt is dominated by mafic volcanics, metasediments and intrusive granitoids. The belt is sandwiched between adjacent sedimentary basins (Sunyani Basin to the west and the Kumasi Basin to the east) and the shared margins are highly faulted and sheared. These northeast trending marginal faults are traceable along the full length of the belt. In addition, there are major prospective faults within the interior of the belt that splay off and link the marginal fault structures that are associated with gold mineralization. Late east-northeast trending crosscutting oblique lineaments are seen in regional data sets and are seen to be represented by similarly oriented structures at the deposit level which are also associated with gold mineralization. The overall structural fabric of the belt strike in NE - SW. The Sefwi belt is shown in Figure 2.1.

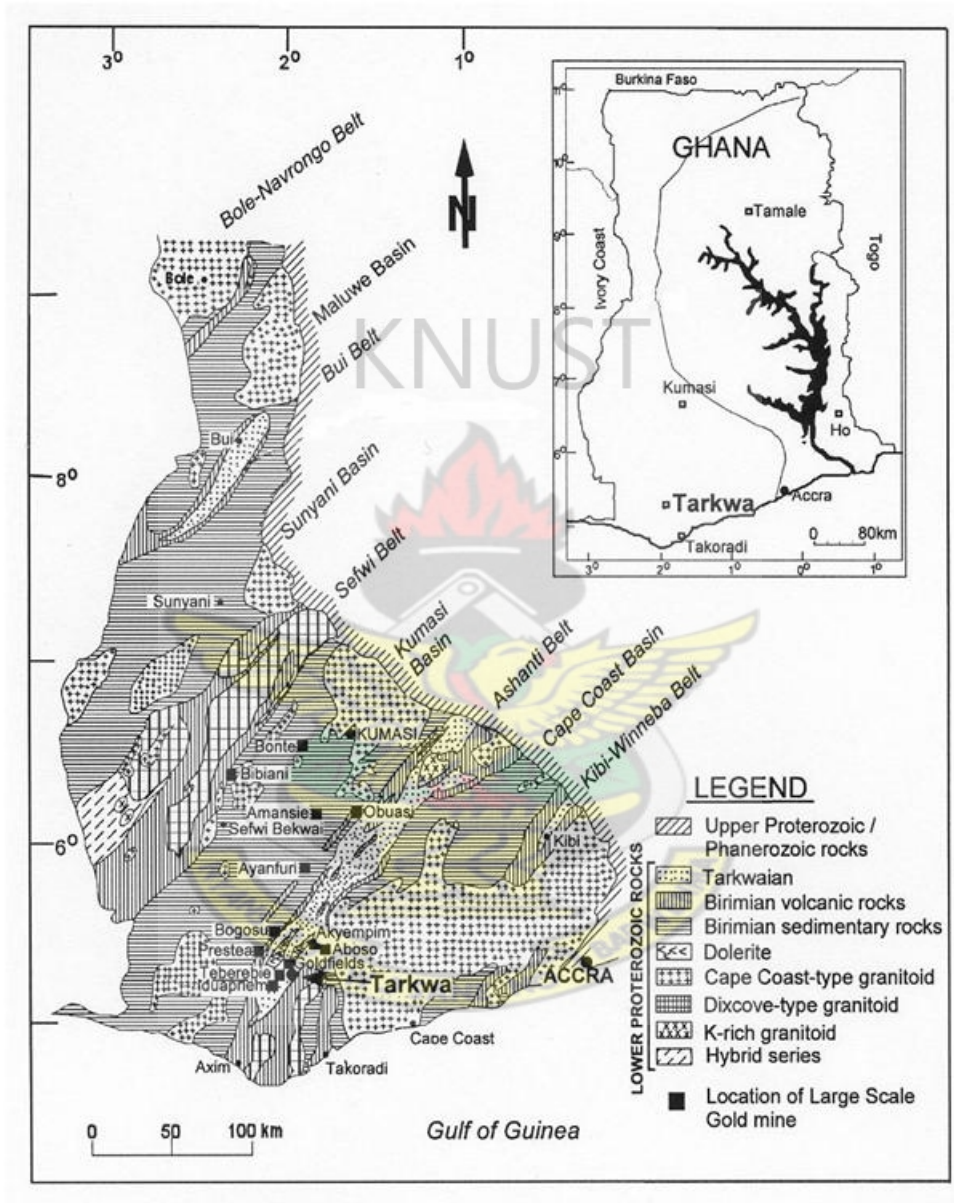


Figure 2.1: Geological map of South-Western Ghana showing the various gold belts (after Kesse (1985)).

2.1.4 Birimian-Hosted Gold Mineralization

Two main types of Birimian-hosted economic gold mineralization are recognized in Ghana (Hirdes and Leube, 1989);

- quartz-vein type and
- Disseminated sulphide type.

The quartz veins are located in fault zones which mostly occur at the margins of the volcanic belts and strike parallel to the regional geological trend. The quartz vein type deposits are generally regarded as epigenetic (Junner (1935); Kesse (1985); Leube et al. (1990)). The most prominent deposits are situated along the north-western flank of the 'Ashanti' belt (Figure 2.1). On a regional scale, the vast majority of Birimian gold deposits occur aligned, and along the flanks of the volcanic belt. The transitional zones along the flanks of the volcanic belts are characterized by the presence of other chemical sediments, namely sulphides; Fe-Ca-Mg Carbonates and rocks rich in carbon (Leube et al., 1990).

This chemical facies probably constitute the most favorable regional exploration guide for gold deposits in the Birimian. Sulphides in the Birimian of Ghana do not form known base metal deposits of economic grade. They consist of pyrite and arsenopyrite which generally occur in a disseminated form. A major mineralogic difference between the two types of mineralization is the presence of free gold in quartz veins type deposits, while gold in the disseminated sulphide type deposits is mostly submicroscopic and hosted in arsenopyrite and pyrite (Leube and Hirdes, 1986).

2.1.5 Tarkwaian-Hosted Gold Mineralization

Economic gold mineralization of the Tarkwaian group in Ghana is restricted quartz-pebble conglomerates. The quartz-pebbles are usually embedded in sand sized quartz veins, displaying mortar texture which is due to recrystallization after sedimentation (Kesse, 1985). The matrix of the conglomerate mainly consists of “black sand” minerals such as hematite, magnetite and Fe-Ti-oxides. The intimate association of gold with conglomerates, its spatial relationship with sedimentological parameters (e.g. paleo-transport directions), the silver depleted nature of the gold, typical for transported gold, as well as the absence of any significant relationship between gold mineralization and cross-cutting quartz vein and the sulphidized haloes, dykes and faults support a paleoplacer origin for the Tarkwaian gold. A prominent quartz vein type of gold here is often spatially associated with dykes and cross-cuts the conglomerates and quartzites and is derived from a source external to the Tarkwaian. Arsenopyrite which is prominent in the Birimian-hosted gold mineralization is notably absent from the conglomerate ores.

2.2 Local Geology

2.2.1 Geology of the Survey Site (Subenso-North Prospect)

Three discrete geological zones are recognized within the Ahafo Project, relating to currently-identified mineralization styles. The Ahafo district currently consists of 12 discrete deposits, localized along multiple northeast-striking structural zones. Several additional exploration targets remain to be tested. All of the “shear zone“ type deposits appear to be

part of the same mineralized system. As with many deposits located in tropical climates, a saprolite zone, typically between 5 and 50 m thick, is developed at the surface. The saprolite zone gives way at depth to a sulphide zone within which gold mineralization occurs in structurally-controlled zones of hydrothermal alteration. Most of the Ahafo deposits remain open both along strike and down dip. Excellent potential exists for connecting some of the deposits into single pits and for discovery of additional deposits.

The Subenso concession of Newmont Ghana Gold Limited is divided into two main zones. They are: Subenso-north deposit and Subenso-south deposit (Figure 2.2). The Subenso South deposit is about 12 km east-northeast of Sunyani. The main Kumasi-Sunyani Highway traverses the south-western portion of the deposit area. It is classified as a Subenso-style deposit. The deposit has dimensions of approximately 1400 m x 250 m, and has been tested to be almost 300 m in depth. Mineralization remains open at depth. In the southern portion of Subenso South, mineralization occurs within a series of parallel shear zones. In the central portion of Subenso South, mineralization is confined to a hanging wall and a parallel, stronger, footwall zone, both of which are constrained by footwall and hanging wall shears. The dominant footwall zone broadens at depth and thins towards surface where the geochemical expression is generally subdued relative to the other Sefwi deposits. The shear zone steepens to the north; this is attributed to over-steepening caused by an inferred parallel thrust fault structure to the west. The structure also broadens at depth at the northern end of the deposit where it comprises the largest mineralized pod in the Subenso Main deposit.

Small-scale duplex structures with a sense of convergence that is east over west are observed in drill-cores. The duplexes may mirror larger duplex structures, which are considered to be the cause of the apparent lenticular shape of the mineralized pods at depth. A high-grade core of mineralization is present in Subenso South, constrained to

hydrothermally altered rocks showing brittle/ductile deformation with later quartz veining. Ductile tight to isoclinal folding is also present, adjacent to both the footwall and hanging wall shear zones in this area. Moderately to strongly foliated metapelites and metavolcanic rocks of the Birimian succession occur in the footwall of the deposit. The hanging wall consists of granodioritic to dioritic composition rocks belonging to the Dixcove suite. The granitoid/volcano-sedimentary contact has been extensively mylonitized, producing additional rock types that are the result of plastic deformation, and mixing of the granitoid and volcano sedimentary units. Tectonic and dilatent breccias formed from these pre-existing units during latter brittle faulting. Late-stage porphyry dikes cross-cut the earlier lithologies. Overlying the deposit is a layer of duracrust that can reach 8 m in thickness. Saprolite can be well-developed, forming a 20 m to 50 m thick zone over the primary bedrock units. Gold mineralization is hosted in the breccia units. Elevated gold grades can form zones of one to 40 m width that assay over 5 g/t Au grade. Lower-grade (0.5 g/t to 1.5 g/t Au) halo-type mineralization as wide as 10 m in the hanging wall granitoids is not well developed.

Mineralization appears to be controlled by the intersection of the tectonic breccia zones with cross-cutting north-south-trending structures. Other zones are clearly related to sharp changes in dip or strike associated with structures deflecting around granitoid bodies. Still others appear to be controlled by small left jogs in the brittle fault zones or by combinations of all factors. A zone of duracrust-hosted mineralization has also been defined, which consists of reworked saprolite that forms a thin blanket on the surface of the deposit. Strong alteration is focused in, and directly adjacent to, the tectonic breccias in one or more multiple zones from 1 m to 45 m wide. Moderate alteration forms a halo around the strongly altered zone between 2 m and 40 m wide. Weak alteration is formed as a broad halo around the other alteration zones, displaying weak bleaching and minor calcite veining. Alteration intensity

can be a reasonable predictor of gold grades, with the more intense alteration associated with elevated grades.

The Subenso North deposit is located about 1500 m northeast of Subenso South deposit. It displays very similar characteristics to Subenso South, and is considered to simply be a northern extension of it, but separated by a zone of lower-grade, sub-economic mineralization. It is classified as a Subenso-style deposit. The deposit has dimensions of 1400 x 3-25 m and has been tested to a vertical depth of 140 m. The deposit remains open at depth. Structural controls to the mineralization at Subenso North are essentially the same as at Subenso South. The footwall and hanging wall shears are, however, better defined, the mineralization more tightly constrained, and the resulting grades slightly higher. This is thought to be in part due to the higher metamorphic grade of the host rocks in the north, which approach amphibolites facies, and in part due to their competency.

Aeromagnetic data suggests that, to the north, the shear zone changes strike towards the northeast, and that it is also offset to the east, most likely by transfer faults. The drilling density is, however, low in this area. Porphyry dykes (and sills) are present in both Subenso North and Subenso South, where they respectively crosscut and parallel the S2 orientation. An additional intrusive has been intersected immediately adjacent to the footwall shear in the northeast. Limited gold remobilization and enrichment appears to have occurred on the margins of these intrusive, but the contacts are generally sharp with occasional evidence of shear fabric and they are interpreted to be late-stage events and to post-date mineralization (Source: Newmont Geology Department Report)

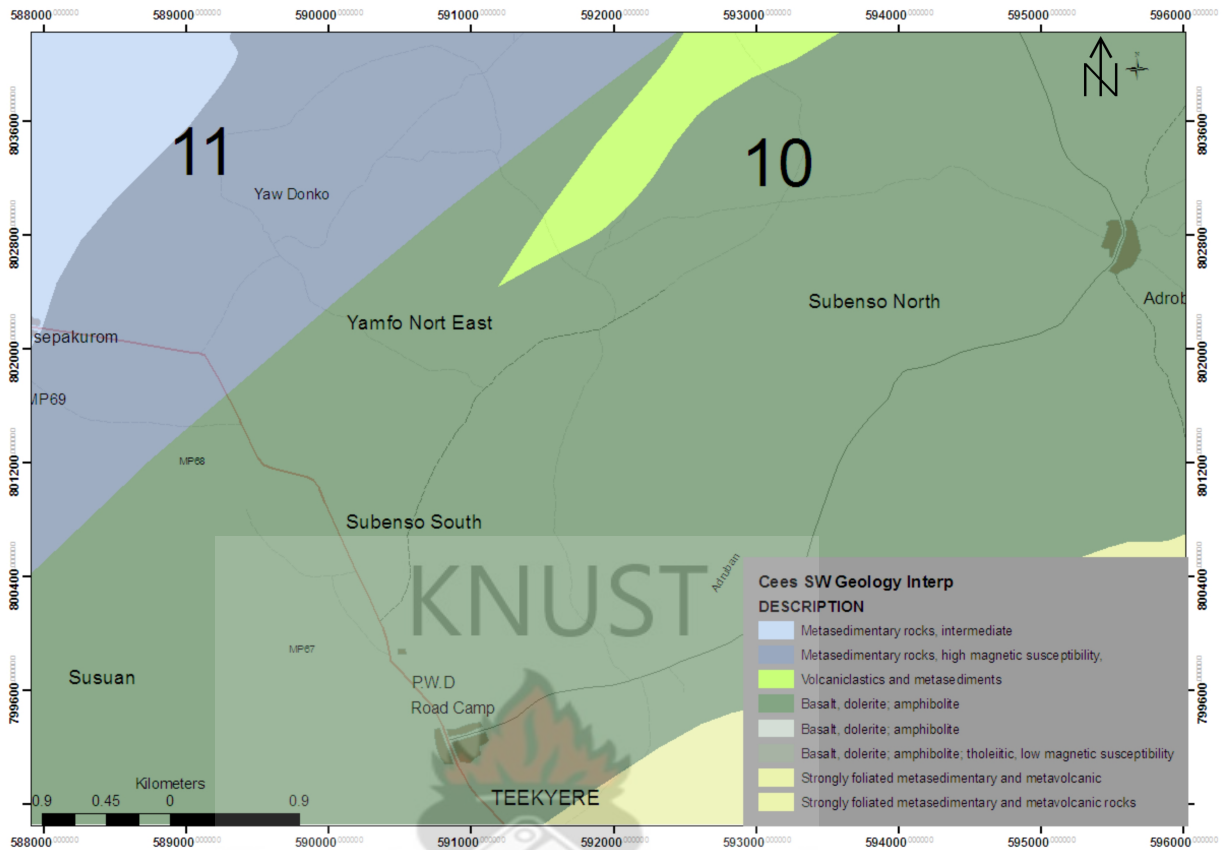


Figure 2.2: Geological map of Subenso-North concession (modified after (Cees, 2006))

2.2.2 Subenso Style Gold Mineralization

Subenso style deposits identified to-date from south to north include Yamfo South, Yamfo central, Teekyere, Subenso South, Yamfo Northeast and Subenso North. The deposits are distinguished by been hosted primarily in (meta) volcano-sedimentary units, with only minor associated granitoid and mylonitic units. The deposits are localized along the northern limb of a northeast-trending, northerly-plunging anticlinorium in multiple northeast-trending, southwest dipping structural zones (Roland, 2004).

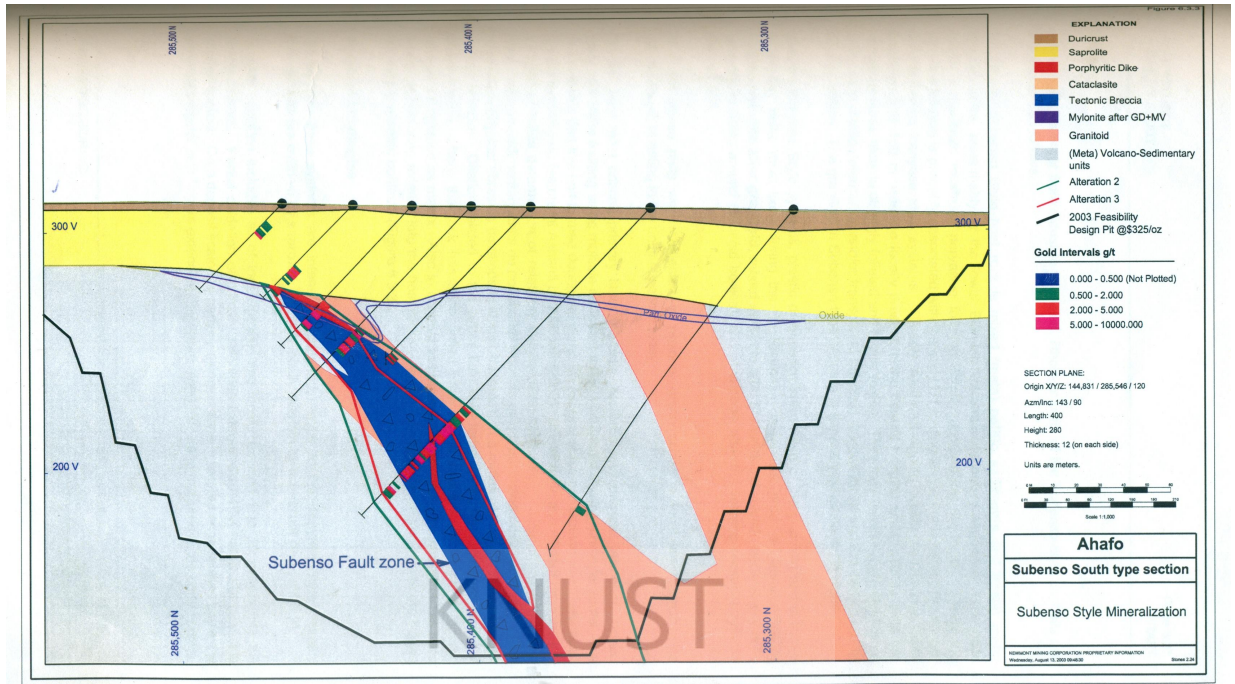


Figure 2.3: Typical section through the Subenso style mineralization (modified after (Roland, 2004))

2.2.3 Subenso Weathered Lithologies

In every exploration work, it is highly relevant to know the various lithologies of the system under investigation. Roland (2004) underscored that, the Subenso style systems are intensely weathered. Primary lithologic units are overlain by saprolite, which is locally overlain by duracrust (Figure 2.3). Complete oxidation includes all of saprolite, and locally extends 1 to 10 m into the primary bedrock. Partial oxidation of primary sulphides extends 0 to 15 m below the complete oxidation contact. On a deposit scale the partially oxidized zone is flat, but on a detailed scale it is extremely irregular with fingers extending downward along joints and fractures in the primary rock.

2.2.4 Subenso Gold Mineralization

Gold mineralization in the Subenso Style system is focused in strongly altered tectonic and connected dilatent breccias, which typically contain >5 g/t gold grades over widths of 1 to 40 m. The tectonic breccia provided plumbing to the systems and permeable host rock, while the dilatent breccias provided discontinuous permeable host and are only mineralized if connected to a tectonic breccia feeder zone. Since the predominant host lithologies are plastic in nature (absorbing deformation with movement on the foliation planes), very limited fracturing extends beyond the tectonic breccia zones. Therefore lower grade 0.5 to 2 g/t halos are narrow (0 to 10 m) and ore to waste contacts are very sharp. The higher grade and generally thicker ore zones in Subenso Style deposits are controlled by a more complex set of structural interactions. Some of the zones appear to be controlled by the intersection of the tectonic breccia zones with cross-cutting north-south trending structures. Other zones are clearly related to sharp changes in dip or strike associated with structures deflecting around granitoid bodies. Still others appear to be controlled by small left jogs in the brittle fault zones or by combinations of all factors (Roland, 2004)

CHAPTER 3

Theoretical Background of the Ground Penetrating Radar Technique

3.1 Fundamental Theory of Ground Penetrating Radar

Ground penetrating radar profiles are similar in appearance to seismic reflection profiles, except that GPR data is acquired using transient electromagnetic (EM) energy reflection instead of acoustic energy and thus provide a greater resolution. A short pulse of high-frequency EM energy (10-1000 MHz) is transmitted into the ground. When the signal encounters a contrast in the material properties, some of the energy is reflected back to the surface due to a change in the bulk electrical properties of different subsurface lithologies. The interface between these two layers may be characterized by bedrock contact, organic-rich sediments, ground water table, and changes in sediment grain size, mineralogy, and packing (Davies and Annan,1989).

3.2 Fundamentals of Electromagnetic Wave Propagation

The GPR technology uses electromagnetic waves to investigate the subsurface. In the following, all material properties will be treated as linear and isotropic, i.e., independent

of direction. While not strictly true, this is an approximation that will keep the mathematics reasonable and still, as experience shows, give useful results.

3.3 Basic Wave Properties

3.3.1 Maxwell's Equations

Maxwell's equations describe the interaction between electric and magnetic fields and the corresponding coupled process propagating as a three-dimensional, polarized, vector wave field, known as electromagnetic radiation (Balanis, 1989): in Modroo and Olhoeft (2004) (2004). The equations in vector form are

$$\nabla \times \mathbf{E} = -\frac{\partial(\mathbf{B})}{\partial(t)} \quad (3.1)$$

$$\nabla \times \mathbf{H} = \mathbf{J} + \frac{\partial(\mathbf{D})}{\partial(t)} \quad (3.2)$$

$$\nabla \cdot \mathbf{D} = q \quad (3.3)$$

$$\nabla \cdot \mathbf{B} = 0 \quad (3.4)$$

where \mathbf{E} is the electric field strength vector [volt/m], \mathbf{H} is the magnetic field intensity vector [ampere/m], \mathbf{J} is the electric current density vector (flux) in $(A m^{-2})$, \mathbf{D} is the electric displacement current vector in $(C m^{-2})$, \mathbf{B} is the magnetic flux density vector $(T m^{-2})$, q

is the electric charge density ($C m^{-3}$), t is time (s), and ∇ is the spatial vector derivative operator.

3.3.2 Constitutive Equations

Constitutive relationships are the means of describing a materials response to electromagnetic magnetic (EM) fields. For GPR, the electrical and magnetic properties are of importance. Constitutive equations (eqn (3.5) , (3.6), (3.7)) provide a macroscopic (or average behaviour) description of EM fields (Harry, 2009).

$$\mathbf{J} = \sigma \mathbf{E} \quad (3.5)$$

$$\mathbf{D} = \varepsilon \mathbf{E} \quad (3.6)$$

$$\mathbf{B} = \mu \mathbf{H} \quad (3.7)$$

where σ is the electrical conductivity, ε is dielectric permittivity and μ is magnetic permeability. Electrical conductivity σ characterizes free charge movement (creating electric current) when an electric field is present. Resistance to charge flow leads to energy dissipation. Dielectric permittivity ε characterizes displacement of charge constrained in material structure to the presence of electric field. Charge displacement results in energy storage in the material. Magnetic permeability μ describes how intrinsic atomic and molecular magnetic moments respond to a magnetic field. For simple materials, distorting

intrinsic magnetic moments store energy in the material (Harry, 2009) From equation (3.1) through (3.7) one can derive the electromagnetic wave equation for the electric field:

$$\nabla^2 \mathbf{E} - \mu\epsilon \frac{\partial^2 \mathbf{E}}{\partial t^2} - \mu\sigma \frac{\partial \mathbf{E}}{\partial t} = 0 \quad (3.8)$$

The wave equation for the magnetic flux density is exactly the same, just substituted \mathbf{B} for \mathbf{E} in Equation (3.8)

$$\nabla^2 \mathbf{B} - \mu\epsilon \frac{\partial^2 \mathbf{B}}{\partial t^2} - \mu\sigma \frac{\partial \mathbf{B}}{\partial t} = 0 \quad (3.9)$$

Note, however that the two expressions, (3.8) and (3.9), of the wave equation are not independent. If we find the electric field vector \mathbf{E} from eqn (3.8) we must return to Maxwell's equations to find the magnetic flux density \mathbf{B} and vice versa. The resulting combination of the \mathbf{E} and \mathbf{B} fields is known as transversal wave. \mathbf{E} and \mathbf{B} are perpendicular to each other as well as the direction of propagation, i.e., they form a right-handed orthogonal set. The vector

$$\mathbf{P} = \mathbf{E} \times \mathbf{B}$$

\mathbf{P} is known as the Poynting vector and gives the direction of the wave propagation. The magnitude of the Poynting vector is equal to the local energy flow per unit area (Mala, 2011). Now, the vector amplitudes \mathbf{E} and \mathbf{B} are not confined to real values. For real valued \mathbf{E} and \mathbf{B} the wave is said to be linearly polarized, i.e., the fields has a constant direction.

For complex vector amplitudes the waves are elliptically polarized. This means that the electric and magnetic field vectors trace an ellipse. They are still perpendicular to each other. Elliptical polarization can be physically realized by superimposing two linearly polarized waves with different polarization direction and phase. To understand the properties

of electromagnetic wave propagation, we consider a single-frequency, linearly polarized, EM plane wave travelling in the z direction; we can derive, from Maxwell's equations, the following expressions for the complex electric \mathbf{E} and magnetic \mathbf{B} field vectors (Knight, 2001)

$$\mathbf{E}(z, t) = \mathbf{E}(Z)e^{-i\omega t} \quad (3.10)$$

Substituting (3.10) into (3.8) and rearranging we get

$$\nabla^2 \mathbf{E} + K^2 \mathbf{E} = 0 \quad (3.11)$$

which is the Helmholtz equation describing the plane wave harmonic solution to (3.8). The propagation constant

$$K^2 = \omega^2 \mu \epsilon + i \omega \mu \sigma \quad (3.12)$$

contains all information about the attenuation and velocity of the wave. The solution to equation (3.11) is

$$\mathbf{E} = \mathbf{E}_0 e^{-i(\omega t - kz)} \quad (3.13)$$

The square root of the propagation constant is known as the wave number, k . The wave number can be expressed as

$$k = a + ib \quad (3.14)$$

Using expressions (3.13) and (3.14) the solution takes the form

$$\mathbf{E} = \mathbf{E}_0 e^{-i(\omega t - az)} e^{-bz} \quad (3.15)$$

where b is the attenuation coefficient. The first exponential represents un-attenuated wave

propagation and the second exponential accounts for the attenuation of the wave with depth. In this expression the velocity and attenuation are decoupled from each other. The velocity of the electromagnetic wave can be found by comparing the first exponential with the equation describing a general harmonic wave travelling with phase velocity v in the z -direction:

$$a = a_0 e^{-i\omega(t - \frac{z}{v})} \quad (3.16)$$

The phase velocity is

$$v = \frac{\omega}{a} \quad (3.17)$$

and the attenuation of the wave expressed as dB/m is

$$B = 20b \log_{10}(e) \quad (3.18)$$

The skin depth, i.e., the depth at which the amplitude of the wave has decreased to $1/e$ of its original value is a common measure of the attenuation

$$\delta_{skin} = \frac{1}{b} \quad (3.19)$$

The skin depth should not be confused with the depth of penetration which is also system dependent. In order to find the value of the velocity and attenuation expressed in the known physical parameters ϵ , σ , and μ , we combine (3.12) and (3.14) and solve for a and b separately. The resulting expressions are

$$a = \omega \sqrt{\frac{\mu\epsilon}{2}} \sqrt{\left(\sqrt{\left(\frac{\sigma}{\omega\epsilon}\right)^2 + 1} + 1 \right)} \quad (3.20)$$

$$b = \omega \sqrt{\frac{\mu\varepsilon}{2}} \sqrt{\left(\sqrt{\left(\frac{\sigma}{\omega\varepsilon}\right)^2 + 1} - 1\right)} \quad (3.21)$$

The quotient $\sigma/\omega\varepsilon$ plays an important role in the behavior of the expression for a and b. It is known as the loss tangent, $\tan(\delta)$ of the medium. The loss tangent is equal to the inverse of the quality factor Q (Mala, 2011)

$$\tan(\delta) = \frac{1}{Q} = \frac{\sigma}{\omega\varepsilon} \quad (3.22)$$

The wave behaviour occurs at high frequencies, i.e., when the loss tangent is small. If we assume that $\tan(\delta) \ll 1$, then the expressions for the face coefficient and the attenuation coefficient can be significantly simplified:

$$a = \omega \sqrt{\varepsilon\mu} \quad (3.23)$$

$$b = \frac{\sigma}{2} \sqrt{\frac{\mu}{\varepsilon}} \quad (3.24)$$

Combining equations (3.17) and (3.23) with the relations, $\mu = \mu_0\mu_r$ and $\varepsilon = \varepsilon_0\varepsilon_r$, we find the well known simplified expression for the radar wave velocity v as

$$v = \frac{c}{\sqrt{(\varepsilon_r\mu_r)}} \quad (3.25)$$

with c being the velocity of light in vacuum. Using equations (3.18) and (3.24) the simplified expression for the attenuation becomes

$$B = 20\log_{10}(e) = 20\frac{\sigma}{2} \sqrt{\frac{\mu}{\varepsilon}} \log_{10}(e) = 1636.01\sigma \sqrt{\frac{\mu_r}{\varepsilon_r}} \quad (3.26)$$

The above expression for the attenuation is independent of frequency. This is the effect of the approximation, $\tan(\delta) \ll 1$. Further, even under this approximation we know that physical parameters are all intrinsically frequency dependent. The transition frequency indicated is the frequency at the wave behavior turns into diffusive behavior. The transition from diffusion to propagation behaviour occurs when the electric currents change from conduction (free charge)-dominant to displacement (constrained charge) current-dominant behavior. For a simple material, the transition frequency f_t is defined as follows: (Harry, 2009).

$$f_t = \frac{\sigma}{2\pi\epsilon} \quad (3.27)$$

The resonance of water molecules limits the frequency spectrum usable for GPR. Water has a relaxation frequency of about 10 GHz, but effects can be seen at much lower frequencies. The frequency range between the transition frequency and the onset of appreciable water relaxation effect is often referred to as the GPR plateau.

3.4 Reflection and Refraction of Electromagnetic Waves

The standard GPR method uses information contained in the radiation scattered back towards the receiver by inhomogeneities in the ground. A brief review of the mechanisms that cause this backscattering is therefore in order. Whenever a radar wave impinges on an object in the ground some of the energy is reflected by the object and some of the energy passes through it. The waves penetrating the object are also subject to refraction, i.e., bending of the ray paths. A wavefront travelling through a medium with varying velocity changes direction according to Snell's law, originally derived for geometrical optics. When an electromagnetic

wave passes through a boundary the wavefronts must match at the interface. If the velocity is different on the two sides of the interface the direction of propagation must change so that the velocities projected on the interface are the same. Or, in other words, the component along the interface of the propagation vector must be equal. As an example take a plane wave as illustrated in Figure 3.1. The plane wave, as discussed earlier, is the basic building block for more complex waves and illustrates Snell's law nicely. Equality of the along-interface component of the propagation vector gives (Mala, 2011).

$$k_1 \sin \theta_1 = k_2 \sin \theta_2 \quad (3.28)$$

where k_1 and k_2 are the wave numbers for the two media. θ_1 and θ_2 are the angles of incidence and refraction, respectively.

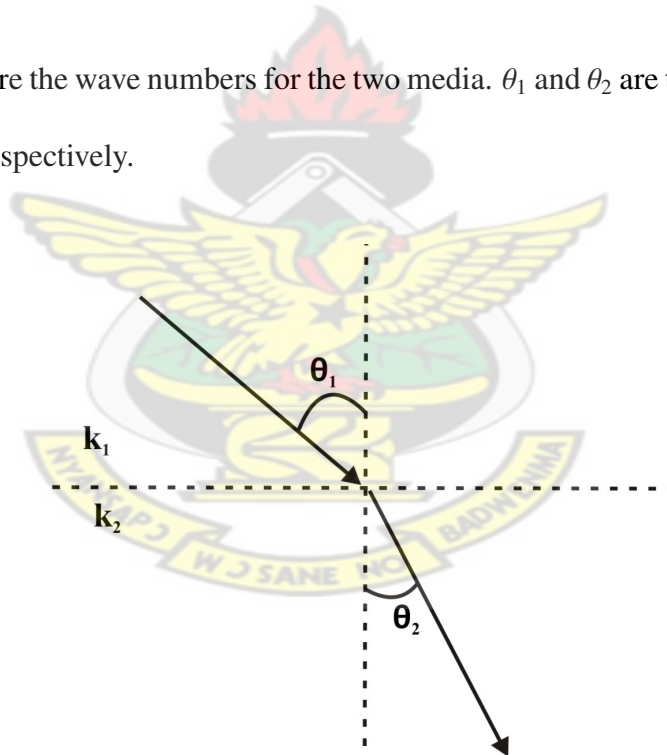


Figure 3.1: Changes of direction of propagation of radar wave as described by Snell's law.

For low loss materials the wave number is $k = \frac{\omega}{v}$ and Snell's law takes the form

$$\frac{\sin \theta_1}{v_1} = \frac{\sin \theta_2}{v_2} \quad (3.29)$$

For the special case of the air-ground interface Snell's law shows that because of the large velocity contrast all waves will be strongly refracted towards the normal and travel more or less vertically downward. One important consequence of the Snell's law is the existence of the critical angle (Figure 3.2). When a wave travels from a high velocity medium to a low velocity medium there are certain angles of refraction that are not possible in reality. These are angles larger than the critical angle see (Figure 3.2). The critical angle is the angle of refraction when the angle of incidence approaches 90 degrees, i.e., the term $\sin(\theta_1)$ in Snell's law approaches unity. The expression for the critical angle is then:

$$\theta_c = \frac{v_2}{v_1} \quad (3.30)$$

Waves travelling from a low velocity medium will be refracted along the interface when the angle of incidence equals the critical angle. For angles of incidence larger than the critical angle the situation becomes quite complicated. In the case $\sin(\theta_1)$ must be larger than 1, something that is not possible for real physical angles but it is possible on the complex plane. From a purely mathematical viewpoint $\sin(\theta_1)$ can only be larger than 1 if (θ_1) is complex. The physical interpretation of such a complex angle is that the horizontal (along the interface) velocity of the wave is less than the phase velocity of the medium. This is only possible if the fields decay exponentially away from the interface in medium 1. This wave is known as an evanescent wave and exists at boundaries and also near field sources.

So far we have only tackled the direction of the waves. When a wave hits an interface part of the energy is reflected and part is transmitted through the interface. The relation between the intensity of the reflected and transmitted fields is described by the Fresnel reflection coefficient. Figure (3.3) gives illustration of the situation.

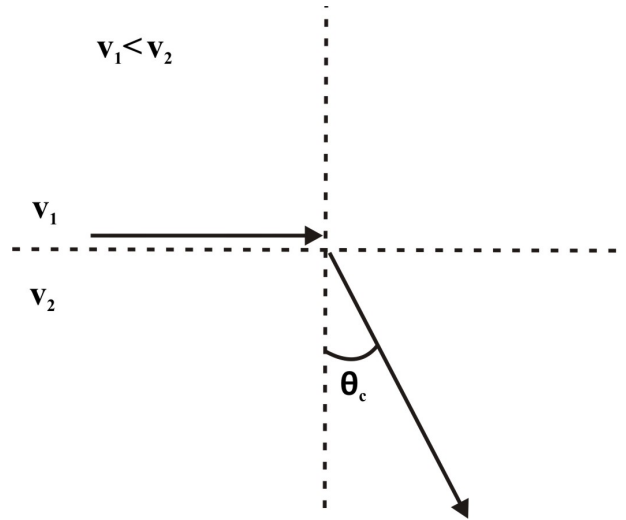


Figure 3.2: Illustration of the critical angle of incidence θ_c

where \mathbf{E}_i is the incident electric field. \mathbf{E}_r and \mathbf{E}_t are the reflected and transmitted fields, respectively. The electric field can in general have any direction perpendicular to the Poynting vector, as long as the triplet \mathbf{P} , \mathbf{E} and \mathbf{B} is an orthogonal set. A plane wave with oblique incidence can always be decomposed into two parts one with the electric field perpendicular to the plane of incidence and one with the magnetic field perpendicular to the plane of incidence. The first component is the TE-component, or the TE polarized wave, and the second is the TM-component, or TM polarized wave. TE and TM are abbreviations for Transverse Electric and Transverse Magnetic, respectively. The reason for this subdivision is that the Fresnel reflection coefficients are different for the propagation modes. For TE polarization the reflection coefficients are:

$$r_{TE} = \left(\frac{\mathbf{E}_r}{\mathbf{E}_i} \right)_{TE} = \frac{v_2 \cos(\theta_1) - v_1 \sqrt{1 - \left(\frac{v_2}{v_1} \right)^2 \sin^2(\theta_1)}}{v_2 \cos(\theta_1) + v_1 \sqrt{1 - \left(\frac{v_2}{v_1} \right)^2 \sin^2(\theta_1)}} \quad (3.31)$$

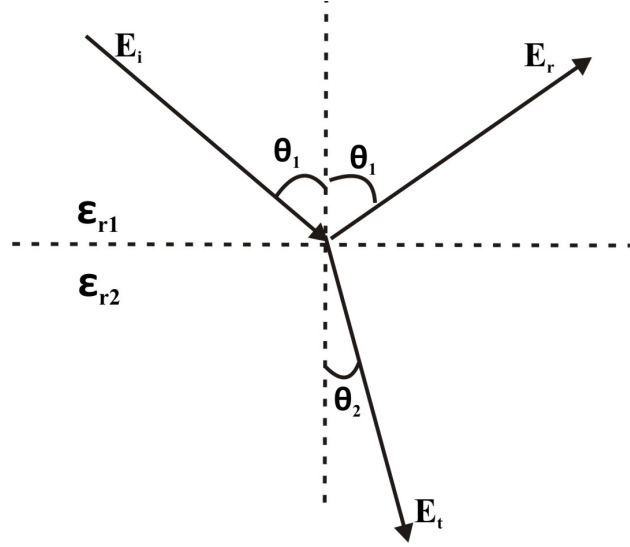


Figure 3.3: Illustration of the behaviour of EM waves at an interface

$$t_{TE} = \left(\frac{\mathbf{E}_r}{\mathbf{E}_i} \right)_{TE} = \frac{2v_2 \cos(\theta_1)}{v_2 \cos(\theta_1) - v_1 \sqrt{1 - \left(\frac{v_2}{v_1} \right)^2 \sin^2(\theta_1)}} \quad (3.32)$$

It may be convenient to express the above equations in terms of the angles of incidence and refraction. The refraction angle is real only for the case $\theta_1 \leq \theta_c$ and the following is restricted to that case. Using Snell's law and some trigonometric manipulation we get the following expressions for the reflection coefficients

$$r_{TE} = \left(\frac{\mathbf{E}_r}{\mathbf{E}_i} \right)_{TE} = \frac{v_2 \cos(\theta_1) - v_1 \cos(\theta_2)}{v_2 \cos(\theta_1) + v_1 \cos(\theta_2)} = \frac{\sin(\theta_2 - \theta_1)}{\sin(\theta_1 + \theta_2)} \quad (3.33)$$

$$t_{TE} = \left(\frac{\mathbf{E}_r}{\mathbf{E}_i} \right)_{TE} = \frac{2v_2 \cos(\theta_1)}{v_2 \cos(\theta_1) + v_1 \cos(\theta_2)} = \frac{2\cos(\theta_1)\sin(\theta_2)}{\sin(\theta_1 + \theta_2)} \quad (3.34)$$

From (3.33) we note that when $v_1 > v_2$ the reflection coefficient becomes negative, i.e., the reflected wave will have a polarity opposite that of the incident wave. Such polarity reversals can in many cases be important for the interpretation work and their presence in the data

should always be noted. For example if we consider the reflection from the ground surface, the radar wave velocity in air is always higher than in the ground, and the wave reflected from the air-ground interface will have an opposite polarity to the direct wave. For normal incidence, $\theta_1 = 0$, the following expressions apply:

$$r_{TE} = \left(\frac{\mathbf{E}_r}{\mathbf{E}_i} \right)_{TE} = \frac{v_2 - v_1}{v_2 + v_1} \quad (3.35)$$

$$t_{TE} = \left(\frac{\mathbf{E}_r}{\mathbf{E}_i} \right)_{TE} = \frac{2v_2}{v_1 + v_2} \quad (3.36)$$

For TM polarization the expressions are similar but only apply to magnitude of the electric field. The direction of the electric field will change the direction on reflection since the triplet P, E and E is an orthogonal set and the Poynting vector and the magnetic field vector are fixed. The reflection coefficient for TM polarization is Mala (2011).

$$r_{TM} = \left(\frac{\mathbf{E}_r}{\mathbf{E}_i} \right)_{TM} = \frac{v_1 \cos(\theta_1) - v_2 \sqrt{\left(1 - \left(\frac{v_2}{v_1}\right)^2 \sin^2(\theta_1)\right)}}{v_1 \cos(\theta_1) + v_2 \sqrt{\left(1 - \left(\frac{v_2}{v_1}\right)^2 \sin^2(\theta_1)\right)}} \quad (3.37)$$

$$t_{TM} = \left(\frac{\mathbf{E}_r}{\mathbf{E}_i} \right)_{TM} = \frac{2v_2 \cos(\theta_1)}{v_1 \cos(\theta_1) + v_2 \sqrt{\left(1 - \left(\frac{v_2}{v_1}\right)^2 \sin^2(\theta_1)\right)}} \quad (3.38)$$

$$r_{TM} = \left(\frac{\mathbf{E}_r}{\mathbf{E}_i} \right)_{TM} = \frac{v_1 \cos(\theta_1) - v_2 \cos(\theta_2)}{v_1 \cos(\theta_1) + v_2 \cos(\theta_2)} = \frac{\tan(\theta_1 - \theta_2)}{\tan(\theta_1 + \theta_2)} \quad (3.39)$$

$$t_{TM} = \left(\frac{\mathbf{E}_r}{\mathbf{E}_i} \right)_{TM} = \frac{2v_1 \cos(\theta_1)}{v_1 \cos(\theta_1) + v_2 \cos(\theta_2)} = \frac{2 \cos(\theta_1) \sin(\theta_2)}{\sin(\theta_1 + \theta_2) \cos(\theta_1 - \theta_2)} \quad (3.40)$$

The minimum in the TM reflection occurs at an angle known as the Brewster angle, this is the angle where $\theta_1 + \theta_2 = \pi/2$. This condition makes the denominator in (3.39) approach infinity and consequently the reflection coefficient goes towards zero. Solving for the Brewster angle we find that it is given by

$$\tan\theta_b = \frac{v_1}{v_2} \quad (3.41)$$

The reflection minimum associated with the Brewster angle occurs only for the TM mode, and is consequently most probable only visible in in-line survey configurations.

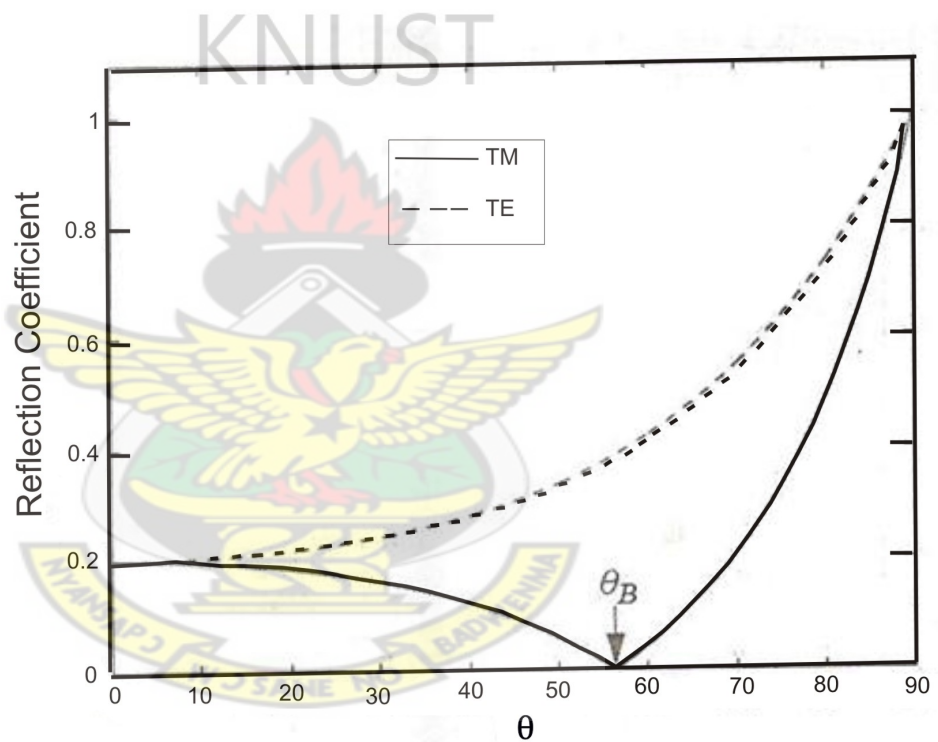


Figure 3.4: Typical plot of the reflection coefficient versus the angle of incidence. θ_B is the Brewster angle Mala (2011)

3.5 Ground Penetration Radar Resolution

The GPR method as implemented in the time domain transmits a temporally pulse and measures the time it takes for this pulse to travel to a target and back. If the velocity of the ground is known one can then convert the travel time to distance. We now need to establish what the resolving capacity of this distance determination is. Note that there are two different resolution measures that are relevant, the range resolution and the lateral resolution; this is illustrated in the Figure 3.5.

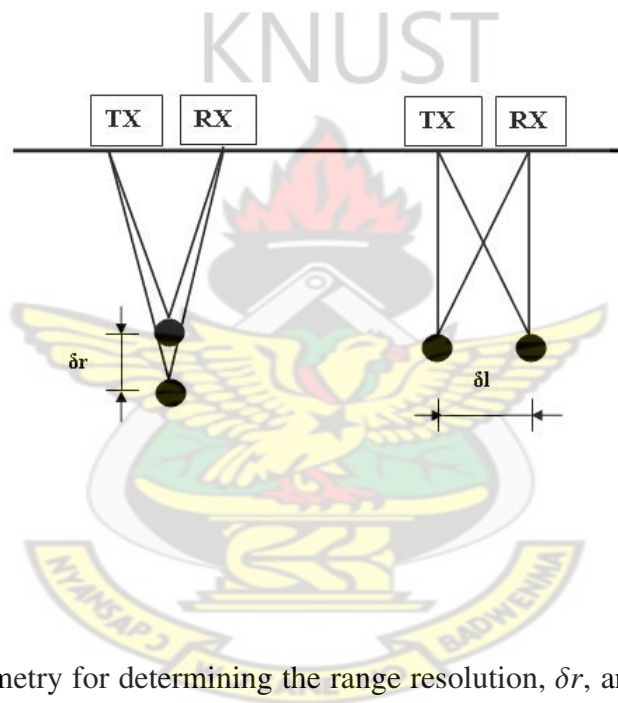


Figure 3.5: Geometry for determining the range resolution, δr , and the lateral resolution δl
Source: Mala (2011)

The response from the two targets will appear as two different, although possibly overlapping, reflections. Each reflection consists of a pulse with a certain pulse width, W , generally defined as the width of the pulse at half amplitude. Two such pulses are considered distinguishable from each other as the time between them is larger than $W/2$. The range and lateral resolution are simply the distance at which the travel time differences between the two ray paths (Figure 3.5) is equal to $W/2$. For the case of the range resolution the travel time

difference is then

$$\Delta t = \frac{2\delta r}{v} = \frac{W}{2} \quad (3.42)$$

assuming that the distance between transmitter and receiver is very small compared to the distance to the reflecting object. This is sometimes known as monostatic approximation for a bistatic system. Solving for the range resolution we get

$$\delta r \geq \frac{Wv}{4} \quad (3.43)$$

The travel time difference for the case of the lateral resolution is given by

$$\delta t = \frac{2(\sqrt{r^2 + \delta l^2} - r)}{v} \quad (3.44)$$

Here we assume that the target is a substantial distance from the object, so that $2(\sqrt{r^2 + \delta l^2} - r) > r$ and the travel time become

$$\delta t \approx \frac{\delta l^2}{vr} = \frac{W}{2} \quad (3.45)$$

solving for the lateral resolution we simply arrive at

$$\delta l \geq \sqrt{\frac{vrw}{2}} \quad (3.46)$$

For GPR the pulse width in time is related to the bandwidth in frequency, B. The bandwidth of a GPR system is normally approximately equal to the center frequency, f_c .

$$W = \frac{1}{B} = \frac{1}{f_c} \quad (3.47)$$

Center frequency and center wavelength are related as

$$\lambda_c = \frac{v}{f_c} \quad (3.48)$$

Combining (3.43), (3.46), (3.47) and (3.48) the range and lateral resolutions then becomes

$$\delta r = \frac{\lambda_c}{4} \quad (3.49)$$

$$\delta l = \sqrt{\frac{r\lambda_c}{2}} \quad (3.50)$$

The latter is in fact also the expression for the Fresnel zone for a monochromatic wave with wavelength, λ_c . The lateral resolution defines a zone of influence, a circle with radius $\delta/2$ within which all reflectors are indistinguishable.

3.6 Scattering Attenuation of GPR Waves

Ground penetrating radar signals are invariably transmitted through complicated media. The signals encounter heterogeneous electrical and magnetic properties on many scales. Smaller-scale heterogeneities generate weak or undetectable responses but their presence has an impact on the signals as they pass by. The heterogeneities extract energy as EM fields passes and scatter it in all direction (Harry, 2009). Figure 3.6 illustrates the effect of the wavelength on the scattering cross-section of a particle.

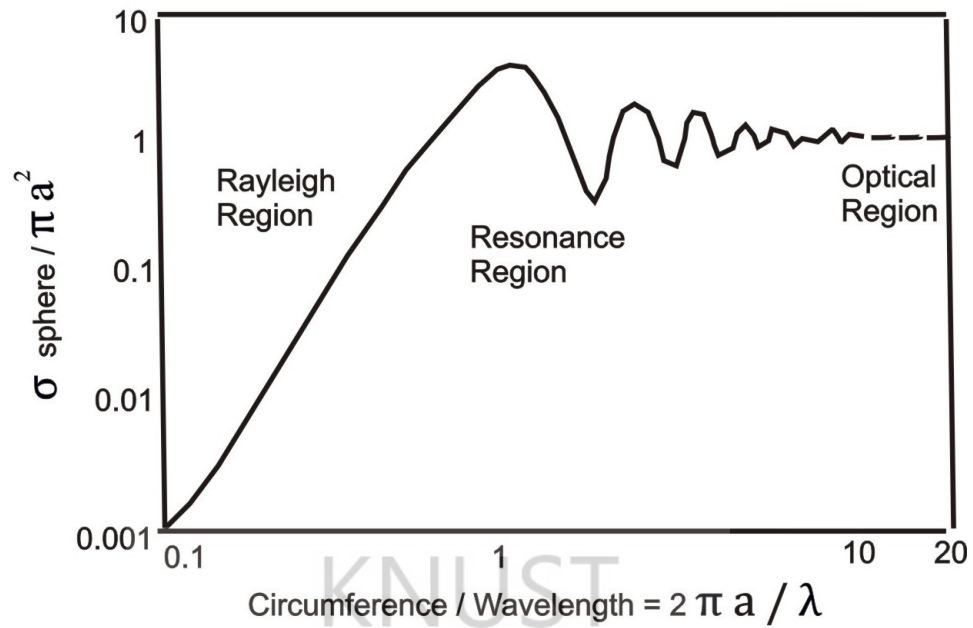


Figure 3.6: Normalized scattering cross-section as function of normalized wavelength (Skolnik, 1970)

For a medium with a random distribution of scatters the effect is that for larger wavelengths a radar wave that passes through this medium is only attenuated by Ohmic dissipation as described by equation (3.26). As the wave length approaches the dimension of the scatters an increasing amount of energy passes through the medium. This energy loss is said to be caused by scattering attenuation. The magnitude of the scattering attenuation can be estimated if one postulates some model for the distribution of scatters in the ground. (Figure 3.7) shows an example of the scattering attenuation. The actual values of the attenuation are not so interesting, what is important is the strong frequency dependence of this attenuation. In many cases it is probable that it is the scattering attenuation that limits the use of high frequency antennas (Mala, 2011)

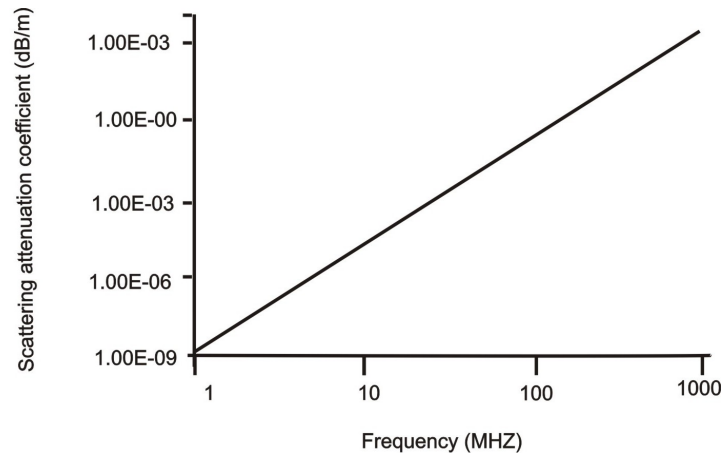


Figure 3.7: Estimate of the scattering attenuation as a function of frequency for a medium with 10 scatterers per cubic meter. Each scatterer has the radius 0.1 m (modified from (Mala, 2011))

3.7 Propagation Dispersion of GPR Waves

In practical GPR experiments one can often observe a change in the shape of the pulse as a function of travel time. This phenomenon is known as propagation dispersion and is caused by the frequency dependence of the velocity and attenuation. In all physical media, both velocity and attenuation increases with frequency. For GPR application the effect of attenuation variation is more pronounced than the effect of velocity variation. The effect of the dispersion is that different spectral components of the pulse travel at different rates. High frequency components travel faster but also decay faster. The net effect is that the pulse appears to move slower and have a lower frequency content the longer it has travelled in the ground (Mala, 2011).

3.8 Dielectric Properties of Geological Materials

Dielectric constant of the natural earth material is defined as the ability of a material to absorb, emit, scatter, and reflect a portion of electromagnetic field. It depends upon the physical properties of the material, which includes shape and size of the sample, humidity, temperature, frequency and the field of measurements. The dielectric properties of the subsurface are the primary control on both the amplitude and the arrival time of the received energy in a GPR survey.

What we image in a GPR survey is thus largely determined by the variation in dielectric properties of the subsurface. If we can image a contaminant with GPR, it is because of a contrast in dielectric properties between the contaminated region and the background “clean” geological materials. If we can determine the hydro-geologic structure or heterogeneity of the subsurface it is because there is a link between the imaged dielectric properties and the hydro-geologic properties of interest. A critical question therefore is, what controls the dielectric properties of materials in both clean and contaminated regions of the subsurface?

In general, the dielectric permittivity and the electrical conductivity are complex, frequency-dependent parameters that describe the microscopic electromagnetic properties of a material. The former accounts for mechanisms associated with charge, whereas the latter accounts for mechanisms associated with charge transport (Knight, 2001). The conductivity and dielectric permittivity are defined as,

$$\sigma(\omega) = \sigma'(\omega) + i\sigma''(\omega) \quad (3.51)$$

and

$$\varepsilon(\omega) = \varepsilon'(\omega) + i\varepsilon''(\omega) \quad (3.52)$$

where ω is angular frequency, $\varepsilon'(\omega)$ is the polarization term, $\varepsilon''(\omega)$ is a faradaic diffusion loss. A detailed discussion of the mechanisms governing these four parameters in Earth materials can be found in (Powers, 1997) and (Olhoeft, 1998). The total response of a material to an oscillating electric field will incorporate all of these mechanisms and can be described either in terms of a total complex permittivity or total complex conductivity. For the purposes of discussing the role of dielectric properties in radar, it is preferable to use the total complex permittivity $\varepsilon_T(\omega)$ given by

$$\varepsilon_T(\omega) = [\varepsilon'(\omega) - i\varepsilon''(\omega)] - \frac{i}{\omega}[\sigma'(\omega) + i\sigma''(\omega)] \quad (3.53)$$

When the right-hand side of this equation is rearranged, we can form a real part representing the ability of the material to store energy through polarization and an imaginary part representing the ability of the material to transport charge. The resulting real-valued, “effective” permittivity and conductivity are:

$$\varepsilon_{ef}(\omega) = \text{Re}\{\varepsilon_T(\omega)\} = \varepsilon'(\omega) + \frac{\sigma''(\omega)}{\omega} \quad (3.54)$$

and

$$\sigma_{ef}(\omega) = -\omega \text{Im}\{\varepsilon_T(\omega)\} = \sigma'(\omega) + \omega\varepsilon''(\omega) \quad (3.55)$$

It is commonly assumed that $\sigma''(\omega) = 0$ and that $\sigma'(\omega) = \sigma_D C$, the frequency independent direct current (D.C) conductivity of the material for notational simplicity, the (ω) designation will be dropped for the remainder of this review. The quantity commonly referred to as the

dielectric constant, is defined as

$$\epsilon_r = \frac{\epsilon_{ef}}{\epsilon_0} \quad (3.56)$$

Where ϵ_0 is the permittivity of free space. The expression for the EM wave velocity and reflection coefficient in a low-loss nonmagnetic medium can be written in terms of ϵ_r as follows (Knight, 2001):

$$v = \frac{c}{\sqrt{\epsilon_r}} \quad (3.57)$$

where c (the speed of light in free space) is equal to ($3 * 10^8 \text{ m s}^{-1}$). This formula assumes that the magnetic susceptibility of the rock is small, which is usually the case.

When electromagnetic wave is incident to a flat boundary of two different materials having the dielectric constant of ϵ_1 and ϵ_2 , the EM wave having the amplitude of 1 is reflected by the boundary and its amplitude is R . R is defined as a reflection coefficient of a boundary and is given by

$$R = \frac{\sqrt{\epsilon_1} - \sqrt{\epsilon_2}}{\sqrt{\epsilon_1} + \sqrt{\epsilon_2}} \quad (3.58)$$

where ϵ_1 and ϵ_2 are dielectric constants of medium 1 and medium 2 respectively

Table 3.1: Attenuation and relative permittivity of subsurface material measured at 100 MHz (Daniels, 1996)

Material	Attenuation (dB m ⁻¹)	Relative permittivity ϵ_r
Air	0	1
Asphalt: dry	2 – 15	2 – 4
Asphalt wet	2 – 20	6 – 12
Clay	10 – 100	2 – 40
Coal: dry	1 – 10	3.5 – 9
Coal: wet	2 – 20	8 – 25
Concrete: dry	2 – 12	4 – 10
Concrete: wet	10 – 25	10 – 20
Fresh water	0.1	80
Fresh water ice	0.1 – 2	4
Granite: dry	0.5 – 3	5
Granite: wet	2 – 5	7
Lime stone: dry	0.5 – 10	7
Lime stone: wet	10 – 25	8
Permafrost	0.1 – 5	4 – 8
Rock Salt: dry	0.01 – 1	4 – 7
Sand: dry	0.01 – 1	4 – 6
Sand: Saturated	0.03 – 0.3	10 – 30
Sand Stone: dry	2 – 10	2 – 3
Sand Stone wet	10 – 20	5 – 10
Seawater	1000	81
Seawater ice	10 – 30	4 – 8
Shale: saturated	10 – 100	6 – 9
Soil: firm	0.1 – 2	8 – 12
Soil: sandy dry	0.1 – 2	4 – 6
Soil: sandy wet	1 – 5	15 – 30
Soil: loamy dry	0.5 – 3	4 – 6
Soil: loamy wet	1 – 6	10 – 20
Soil: clayey dry	0.3 – 3	4 – 6
Soil: Clayey wet	5 – 30	10 – 15

3.9 Ground Penetrating Radar Surveys

Ground penetrating radar measurements fall into two categories, reflection and transillumination. Reflection surveys using a single transmitter and a single receiver are the most common, although multiple source and receiver configurations are used occasionally for some specialized applications.

3.9.1 Common-Offset Reflection Survey

Common-offset surveys deploy a single transmitter and receiver with a fixed offset or spacing between the units at each measurement location. The terminology for such a survey is single-fold common offset. The transmitting and receiving antennas have specific polarization character for the field generated and detected. The antennas are deployed in a fixed geometry and measurements made at regular station intervals. Data at uniform spacing are normally desired if advanced data processing and visualization techniques are to be applied. The objective of reflection surveys is to map subsurface reflectivity versus spatial position. Variations in reflection amplitude and time delay indicate variations in velocity, attenuation (α), and depth (Z). Ground penetrating radar reflection surveys are traditionally conducted on "straight" survey lines and systems are designed to operate in this fashion. The parameters defining a common-offset survey are GPR center frequency, the recording time window, the time sampling interval, the station spacing, the antenna spacing, the line separation spacing, and the antenna orientation (Harry, 2009)

3.9.2 Multi-offset Common Midpoint/Wide-Angle Reflection and Refraction Velocity Sounding Survey

The common midpoint (CMP) or wide-angle reflection and refraction (WARR) sounding mode of operation is the EM equivalent to seismic refraction and wide-angle reflection. Common midpoint soundings are primarily used to obtain an estimate of the radar signal velocity versus depth in the ground by varying the antenna spacing and measuring the change in the two-way travel time. Multi offset measurements can be performed at every station resulting in a multifold reflection survey. Two benefits are that CMP stacking can improve signal-to-noise ratio. Multifold GPR surveys are seldom performed because they are time consuming, more complex to analyze, and most of the cost effective benefit is obtained with well-designed, single-fold surveys (Harry, 2009)

3.9.3 Transillumination Surveys

Transillumination GPR measurements are less common. Most uses involve GPR measurements in boreholes for engineering and environmental studies (Olhoeft (1988); Olsson et al., (1992). Applications to image pillars and walls are increasing. In both cases, estimates of v and α are derived from signal travel time and amplitude measurements. The survey parameters are GPR frequency, station interval, time window, temporal sampling interval, and borehole spacing or wall/pillar thickness. Antenna orientation is seldom an issue since boreholes are usually slim, and the traditional electric dipole axis is aligned with the borehole. Some special borehole systems for larger diameter holes have been designed to have source and receiver directionality. For walls and pillars, maximizing vector-field coupling needs consideration. The ground response is measured at discrete points along the

survey line. Although field practice may be more erratic, data of this format are key to most systematic data processing and visualization. Systematically varying antenna separation varies the signal path in the ground while keeping the point of reflection fixed enabling wave properties to be estimated (Harry, 2009)

3.10 Noise sources that could Preclude the Use of GPR

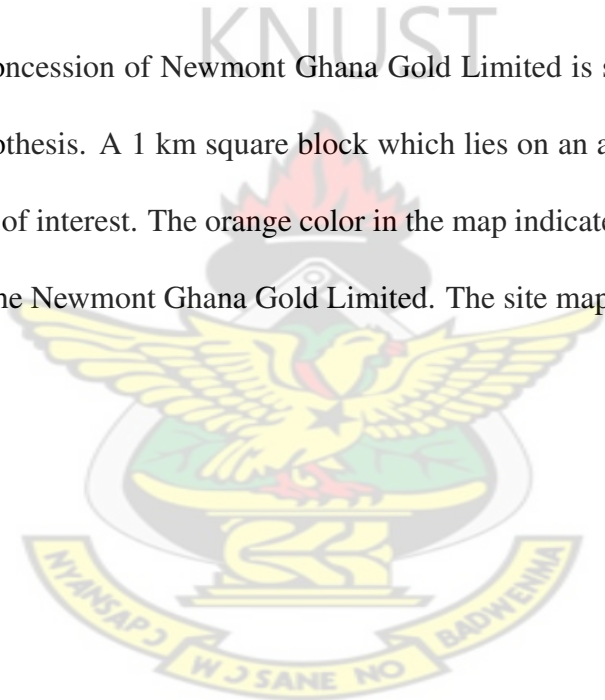
Recorded GPR signals during surveys can be masked by electromagnetic signals from nearby sources such as a radio transmitter or an electric power line located near the survey site; in such cases, external signals may saturate the sensitive receiver electronics. Radio transmitters are potential sources of interference and powerful radio signals can overwhelm receiver electronics (Oluwatosin, 2010). Mobile phones are increasingly becoming a ubiquitous form of interference; proximity to metal objects can also be disastrous for GPR survey. Reflections can come from objects away to the side (sideswipe) and may be very strong if metallic reflectors are involved. Surface features can produce strong sideswipe resulting from substantial radiation of energy along the ground/air interface if ground conductivity is high. Shielded antennas are very useful in such situations and are available in the 100 MHz frequency range and above (Oluwatosin, 2010).

CHAPTER 4

MATERIALS AND METHODS

4.1 Site Description

Subenso-north concession of Newmont Ghana Gold Limited is selected as the test area for the research hypothesis. A 1 km square block which lies on an already known gold deposit is our major area of interest. The orange color in the map indicates the various gold deposits explored for by the Newmont Ghana Gold Limited. The site map is shown in figure (4.1).



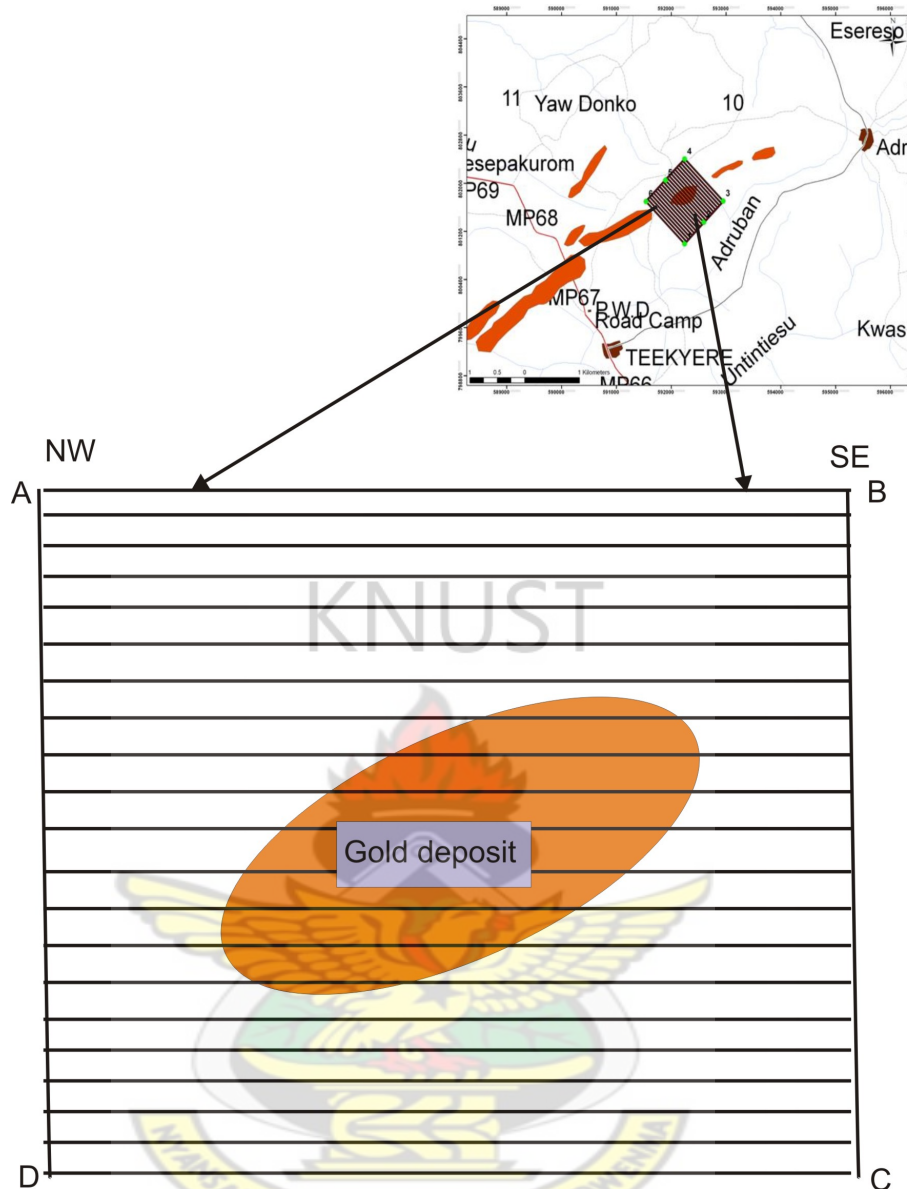


Figure 4.1: Map of Subenso-North gold deposit showing the surveyed area ABCD with profile lines (courtesy Newmont Ghana Ltd geophysics department)

Profiles lines were first demarcated across the deposit which strikes north-east south-west with a profile interval of 50 m. A total of twenty-one profile lines were surveyed. The profiles start with the base line of 2000E/3000N and end at 3000E/3000N.

4.1.1 Equipment for the GPR Survey

The RAMAC GPR system made by the MALA Company was used for this work. The system comprises the MALA ProEx control unit, the XV monitor and the antenna unit. The XV monitor is powered by a 12 V standard Li-Ion Batteries. For the sake of this work, the Rough Terrain Antenna (RTA) unshielded was used for the survey. The RTA was chosen because of its operational flexibility on rough terrain environments alongside its high penetration ability. The frequencies used were 25 MHz and 50 MHz rough terrain antenna (RTA). Each frequency was used separately to traverse all the twenty-one profile lines. The Rough Terrain Antenna (RTA) series from MALA affords flexibility required in low-frequency GPR surveying in rough terrains typical of outcrops.

The antenna design provides improved performance for deeper penetration and the flexible “snake“ like design allows the antenna to be maneuvered easily and efficiently through dense vegetation or most uneven of terrain without affecting ground contact, providing optimum results in the most difficult of environments; the most important benefit being that the operator does not have to clear an access path or route prior to the profile or survey. The RTA is an antenna of unshielded type, unwanted noise most often in form of air reflections can also occur in the data due to the fact that the antenna emits electromagnetic waves in any direction and also receive them from any direction (Oluwatosin, 2010). A hand held GPS was also employed to pick GPS coordinates on all the twenty-one profile at a distance spacing of 50 m along the traverse.



Figure 4.2: MALA GPR equipment used for the survey: A is XV monitor, B is Control unit, C is the RTA

4.1.2 Measurement Parameters

The parameters required for a particular survey is highly relevant, and the operator must have a genuine knowledge of the field under study. These parameters must be chosen in such a way that, both penetration and resolution of the radar wave are achieved. For the sake of this work, the following measurement parameters were critically looked at. Time window defines the total trace length of time the electromagnetic wave is transmitted. The time window does controls the depth and number of samples of the received reflected signals. The time window chosen for this work was on the range of 953.9 ns (50.25 m, 480 smp) for 25 MHz, 747.5 ns (39.42 m, 400 smp) for 50 MHz and 484.1 ns (25.28 m, 400 smp) for 100 MHz rough terrain antenna frequencies. The ground velocity was set to 100 m/ μ s. This velocity determines the speed of the moving electromagnetic wave in the ground/soil measured.

The acquisition mode is a measurement parameter that defines how the measurements are to

be gathered. Basically there are two types of acquisition mode: the time triggering mode and the distance mode. The time triggering mode was used for the survey with a sampling time interval of 2 seconds. The GPR data were collected in a constant offset mode. In a constant offset mode collection, the RTA receiver and transmitter which are at a fixed distance with a cable connecting them were dragged on the surface along each profile line. The average time used to cover 1 km profile line was 19 minutes and this gives an average speed of 0.053 km/min.



Figure 4.3: GPR data collection in a continuous mode operation: A is the XV Monitor, B is the control unit and, C is the 100 MHz RTA antenna

Sampling frequency defines the interval in which samples are taken over a trace length. The sampling frequency was set to 247.48 MHz for 25 MHz RTA and 494.96 MHz for 50 MHz RTA respectively. The number of stacks was set to 'auto stack'. This was done to increase the signal to noise ratio. The antenna separation for the various antenna frequencies used for the survey were; 6.2 m and 4.2 m for the 25 MHz and 50 MHz RTA respectively.

4.1.3 GPR Data Processing and Presentation

GPR signals are usually processed like seismic data although the two are slightly different. Generally, GPR data are treated a scalar although as an electromagnetic fields, they are vector quantities. In view of this, GPR signals may behave differently due to frequency dependent absorption and phase changes at reflection points. In the early days, much of the GPR data processing was done with the seismic data processing software. But due to technological advancements, however, GPR specific processing software is now available from packages offered by manufacturers of GPR or as add-ons for seismic processing software (Oluwatosin, 2010). For this work, REFLEXW (Sandmeier, 2011) was used for the data processing. Like the seismic reflection data, GPR data require processing aimed at sharpening the signal waveform by improving the signal to noise ratio of the radar profiles (Oluwatosin, 2010). The amount of processing depends on the quality of the field data obtained, and this can range from basic processing steps to a more complex application of data processing algorithms.

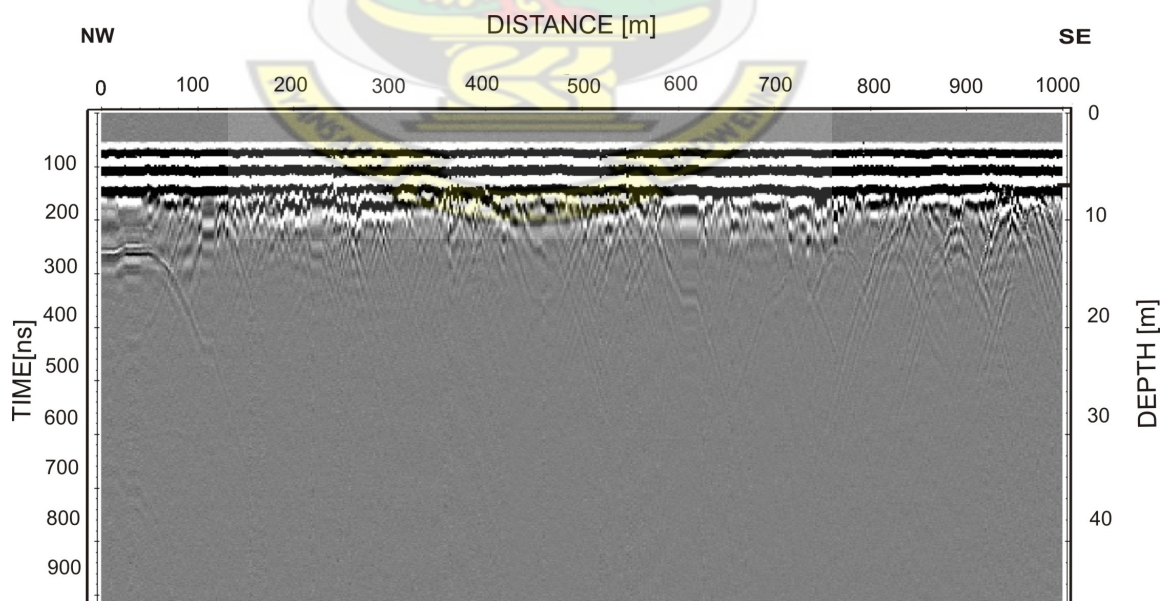


Figure 4.4: Raw unprocessed GPR data from the Newmont's Subenso-north concession

In raw unprocessed GPR data, beddings, bounding surfaces and hyperbolic reflection signatures are hardly visible figure (4.4).

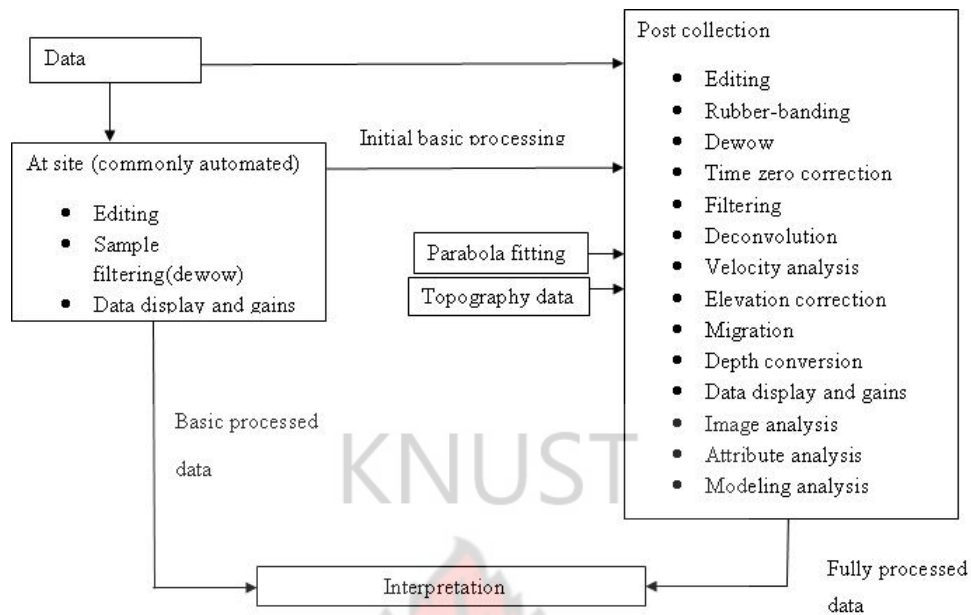


Figure 4.5: Typical processing flow sequence for 2 D-monostatic common-offset, reflection mode GPR data. (modified after (Hary, 2009))

4.1.3.1 Data/Trace Editing

Generally, data editing is the first step to be carried out during GPR data processing. Due to the large volume of the data acquired from the field, an effective maintenance of the data was ensured so as to achieve good-quality interpretation. The inevitable errors that occurred on the field of data acquisition were immediately sorted out and were deleted. The GPR data collected on all the profiles were displayed on the XV color monitor for immediate visual inspection and quality control.

4.1.3.2 Dewow Filtering

This is the removal of the initial DC signal component or DC bias, and subsequent decay of 'wow' or low-frequency signal trend present in the data (Dougherty et al., 1994): in Harry (2009). Wow is caused by the swamping or saturation of the recorded signal by early arrivals (i.e., ground/air wave) and/or inductive coupling effects and requires the subtraction of the DC bias from the signal and application of an optimized, low-cut or median filter for effective correction (Fisher et al., 1994): in Harry (2009). Since dewowing is a vital step in GPR data processing, it was applied on all the data sets in order to reduce the data to a mean zero level and, therefore, allows positive-negative color filling to be used in the recorded data.

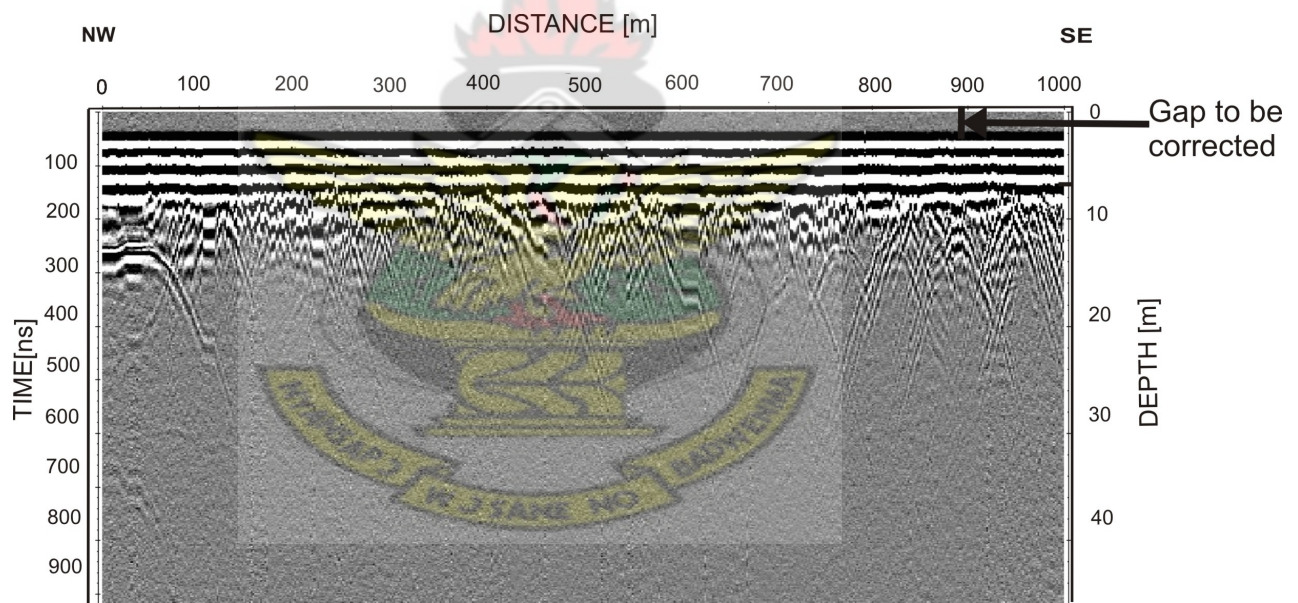


Figure 4.6: dewow filter correction on a 100 MHz GPR section

4.1.3.3 Time-Zero Correction

Thermal drift, electronic instability, cable length differences and variations in antenna air gap can cause 'jumps' in the air/ground wavelet first arrival time (usually referred to as the

Time-Zero point; (Nobes, 1999), (Young et al., 1995) : in Harry (2009). This has effect on the position of the ground interface; therefore, it is incumbent on the 'processor' to adjust the traces to a common time-zero position before processing methods can be applied. This correction was done automatically by the REFLEXW Software. The air wave first break point or first negative peaks of the trace were used to perform this correction. An example of the corrected time-zero is shown in figure (4.7).

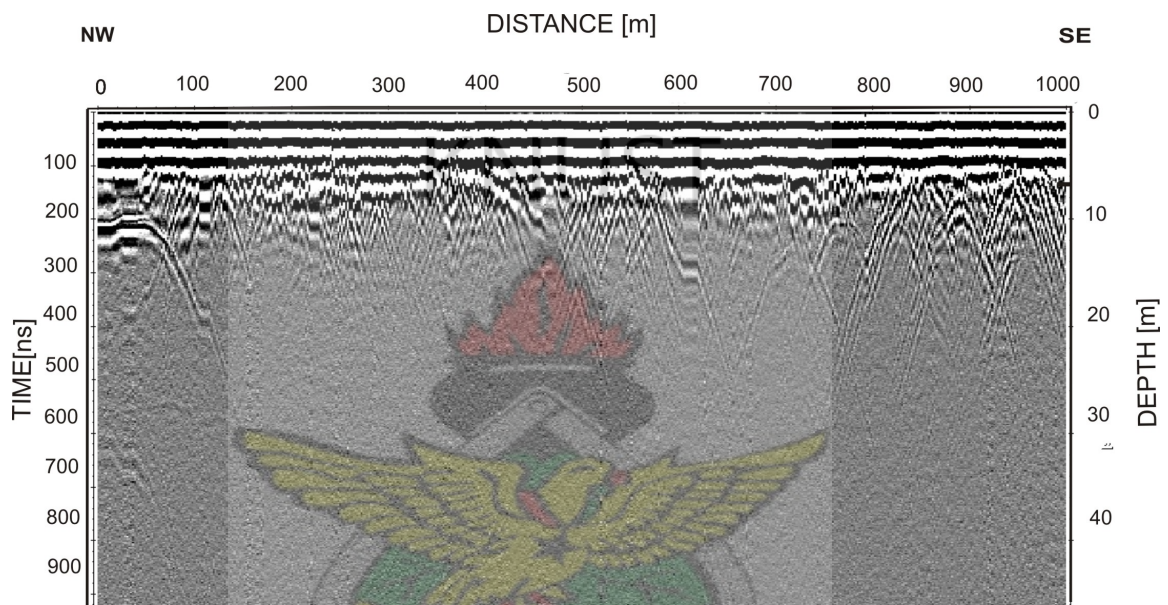


Figure 4.7: Example of time-zero correction on a 25 MHz RTA GPR section (the top gap in fig 4.6 has been adjusted to the zero level on the time axis)

4.1.3.4 Velocity Analysis and Depth Conversion

So far, the processing steps have been performed in the time domain, and the data not related directly to depth. It is practically important to convert the GPR sections to depth scale. This helps in the interpretations and application of elevation corrections. The quality of the velocity estimates is directly proportional to the quality of the depth estimates

In this work, the velocity estimates were picked using the hyperbola fitting from the GPR

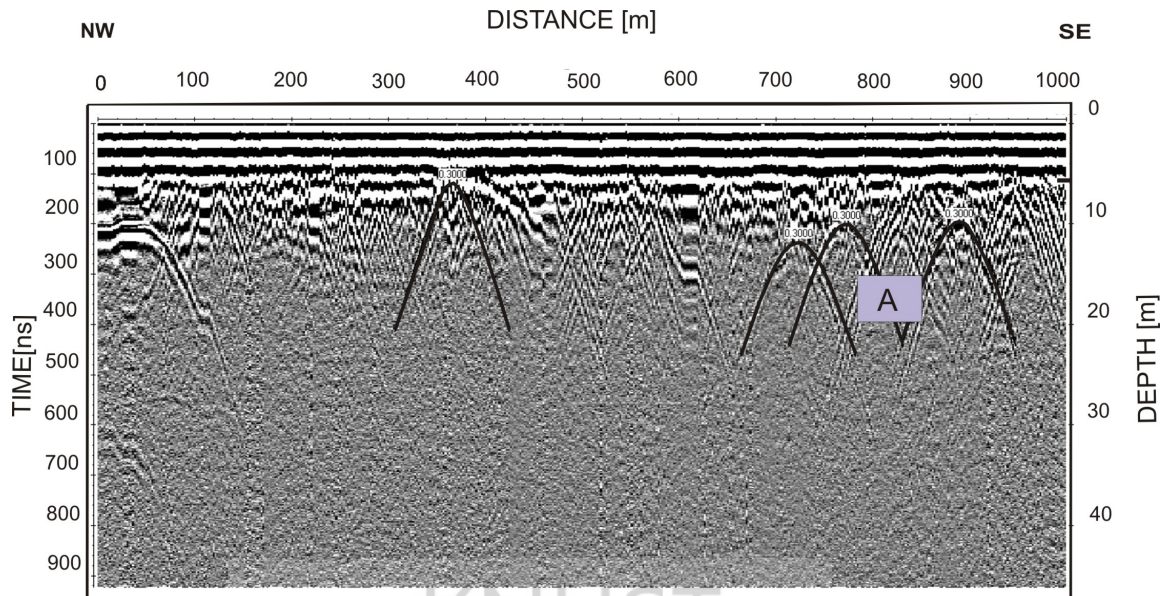


Figure 4.8: Velocity adaptation by hyperbola (marked A) fitting

sections. An example of this is shown in Fig (4.8) where two hyperbolic functions have been fitted to diffraction hyperbola from 25 MHz RTA GPR section with a 0.3, 0.3 and 0.3 m/ns velocity respectively. In practice, both common midpoint (CMP) and hyperbolic matching techniques tend to produce approximate velocity values with errors and variance of $\pm 10\%$ or worse (Harry, 2009).

4.1.3.5 Background Removal

The background removal takes the mean of all traces in a section and subtracts it from each trace. It does remove the background noise and is good for antenna ringing (Harry, 2009). In this work, the background removal filters was employed to remove horizontal and nearly horizontal stripes or features in the data by applying a horizontal high pass filter. The judicial use of background removal filter is a key step in processing and interpretation of GPR sections in relatively lossy material (e.g. wet soils). In these environments, strong antenna-ground coupling and shallow near-surface layers can cause significant reverberation

in the signal that can mask later signals (Harry, 2009).

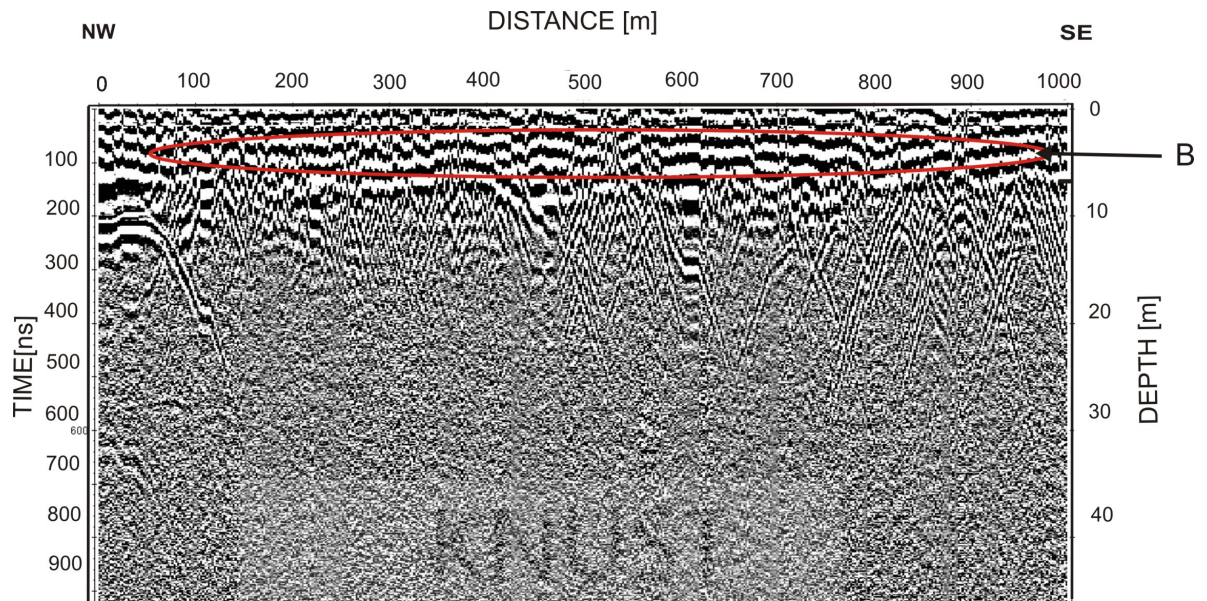


Figure 4.9: GPR data after background removal

4.1.4 Time Gain

Radar Signals are very rapidly attenuated as they propagate into the ground. Signals from greater depths are very small when compared to signals from shallower depth. In view of this, the time gain correction was applied to compensate the rapid fall of the radar signals from deeper depths (Harry, 2009).

CHAPTER 5

RESULTS AND DISCUSSION

5.1 Interpretation of Field Results

5.1.1 GPR Results from 25 MHz RTA Antenna

5.1.1.1 Traverse 1: Line 2000E/3000N

The results of line 2000E/3000N are represented in Figure 5.1 and Figure 5.2 respectively. The results comprise a radargram of 25 MHz data in Figure 5.1 with the inferred structural interpretation in Figure 5.2. The topmost layer picked with the pink color which is designated by D indicates the contact zone between the duracrust and saprolite at depth of about 6 m. The Saprolite is overlain by this duracrust. From Figure 5.1, the saprolite has an average thickness of about 8-50 m deep. Within the saprolite at about 30 m and 45 m, two structural discontinuities labeled S1 and S2 are delineated. The subsurface is seen to have many fractures, some of the inferred structures dip horizontally and others dip Sub vertically. The S1 structures extends at a maximum length of about 300 m and a minimum length of about 100 m distance. Furthermore, the S2 structures which are located between the depth intervals of 40 m and 44 m extends at a maximum length of 340 m. These structures are the inferred structures which are interpreted as the major zones possibly hosting gold mineralization.

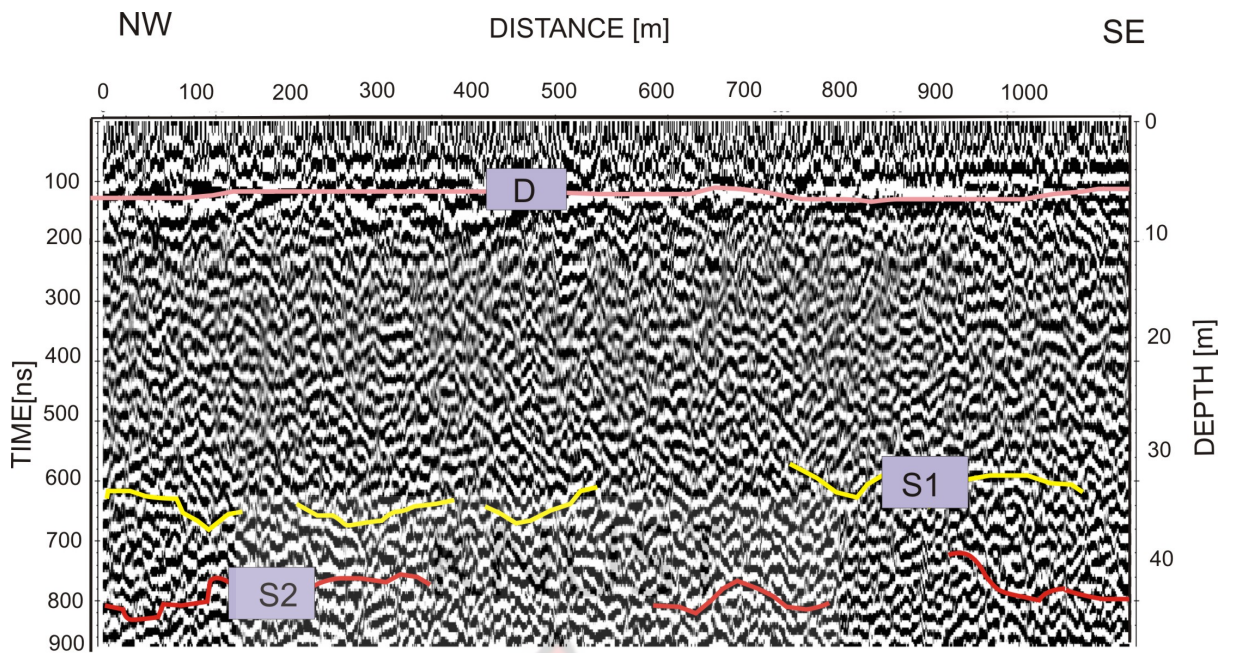


Figure 5.1: Radar Section of profile 2000E/3000N

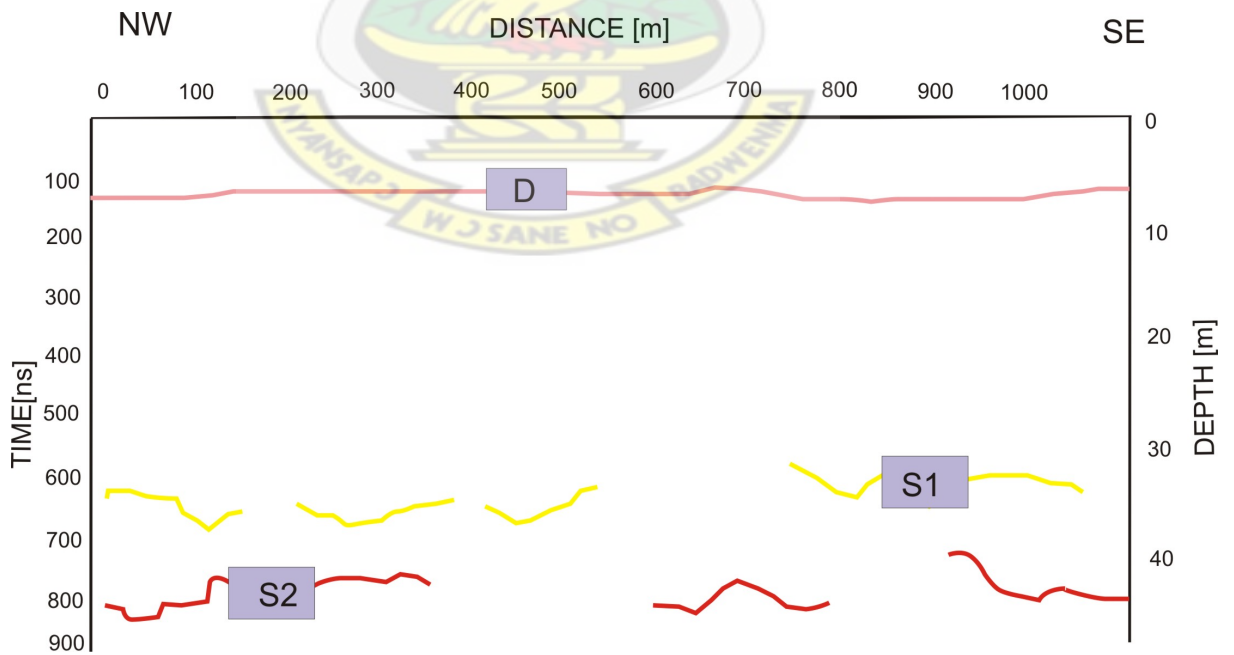


Figure 5.2: Inferred structures hosting mineralization of profile 2000E/3000N

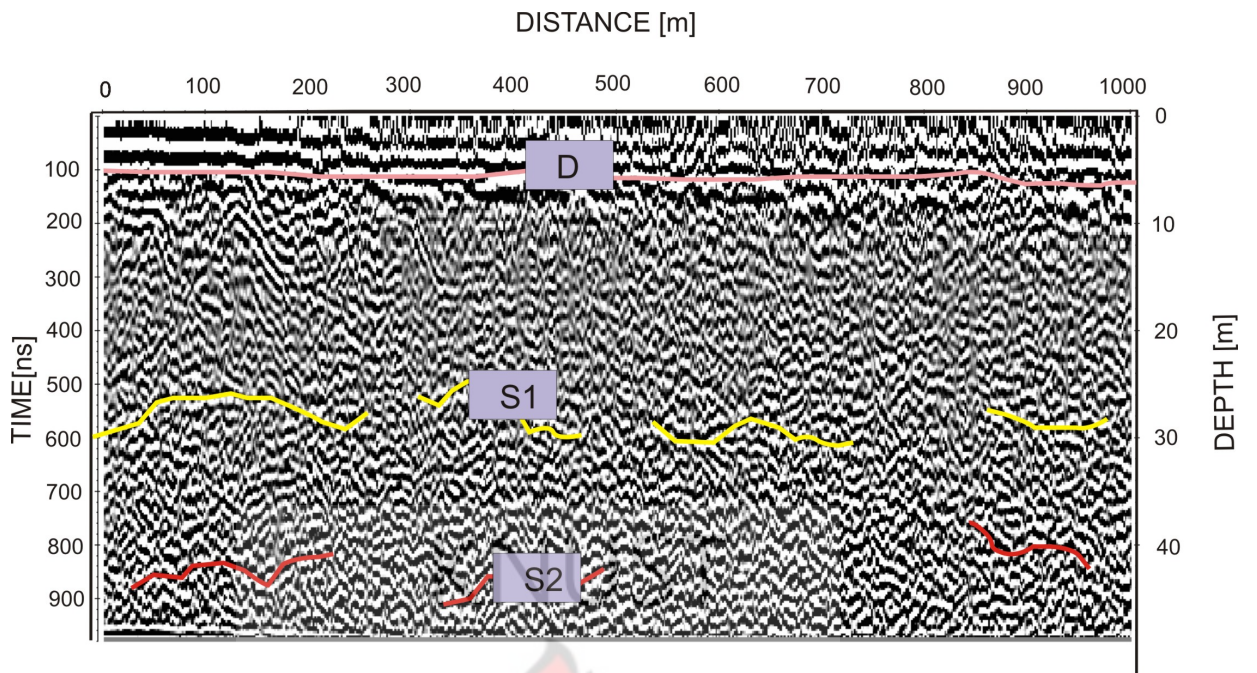


Figure 5.3: Radar Section of profile 2050E/2000N

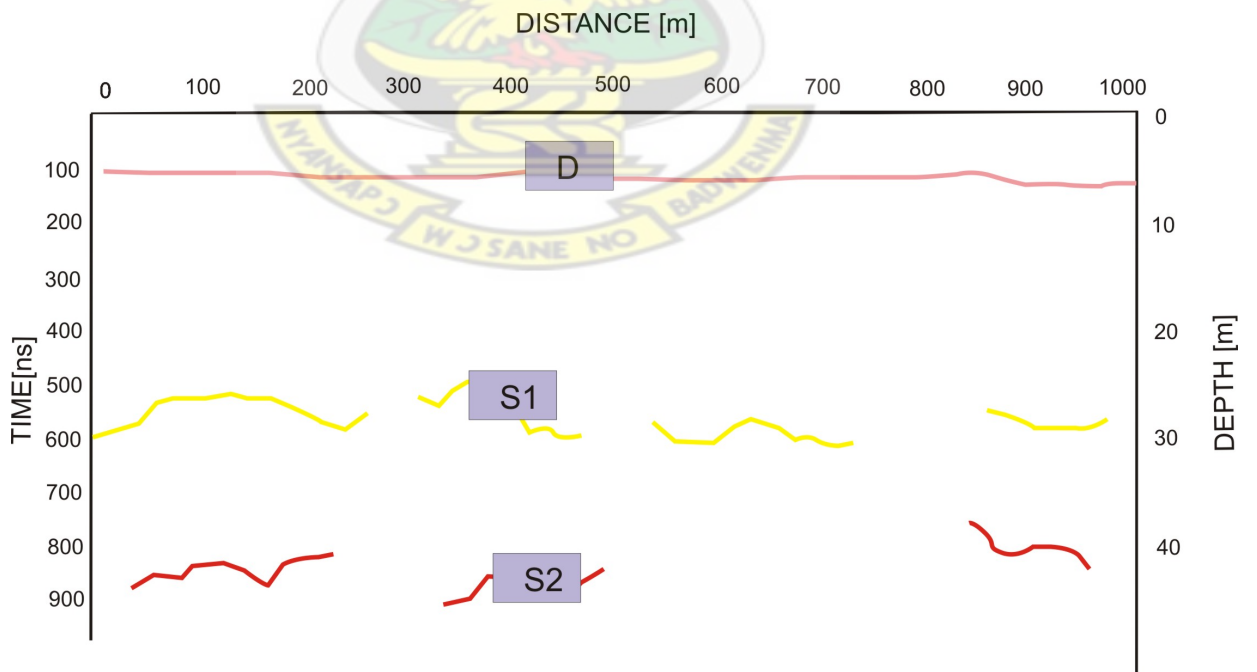


Figure 5.4: Inferred structures hosting mineralization of profile 2050E/2000N

5.1.1.2 Traverse 2: Line 2050E/2000N

Figure 5.3 and Figure 5.4, illustrate the results of line 2050E/2000N. The structure marked by D represents the Duracrust and saprolite transition. The fractured, weathered mineralized zones located between the depths of about 28 m and 45 m is clearly delineated by the horizontal and sub horizontal reflectors shown in the radargram and the inferred interpretation plot. Two sets of structures S1 and S2 are shown in the radargram in Figure 5.3. The high levels of fractures located between the depths aforementioned constitutes a probable region where gold mineralization may occur. This is due to the fact that, the fractured zones are the weaker zones where hydrothermal solution can be transported, thereby leaving traces of mineralization. Despite faults play important role in gold mineralization, not all faults or fractures that are mineralized. There is a very weak fracture anomaly between the depths of about 0 and 25 m. Probably this zone might not show strong mineralization.

5.1.1.3 Traverse 3: Line 2100E/3000N

Figure 5.5 shows the results for line 2100E/3000N with an exploration depth of about 50 m. The inferred structures hosting gold mineralization is also shown in Figure 5.6. The structure marked by D represent the thickness of the duracrust. It is clearly seen from the radargram in Figure 5.5 that, the structures in this situation are marked by S1 and S2. The S1 structures have the maximum length of about 390 m. While the S2 structures also trend with the maximum length of about 230 m. The S1 and S2 structures are inferred structures with potential of hosting gold mineralization. This profile almost show the same anomaly as that of the profile 2000E/3000N.

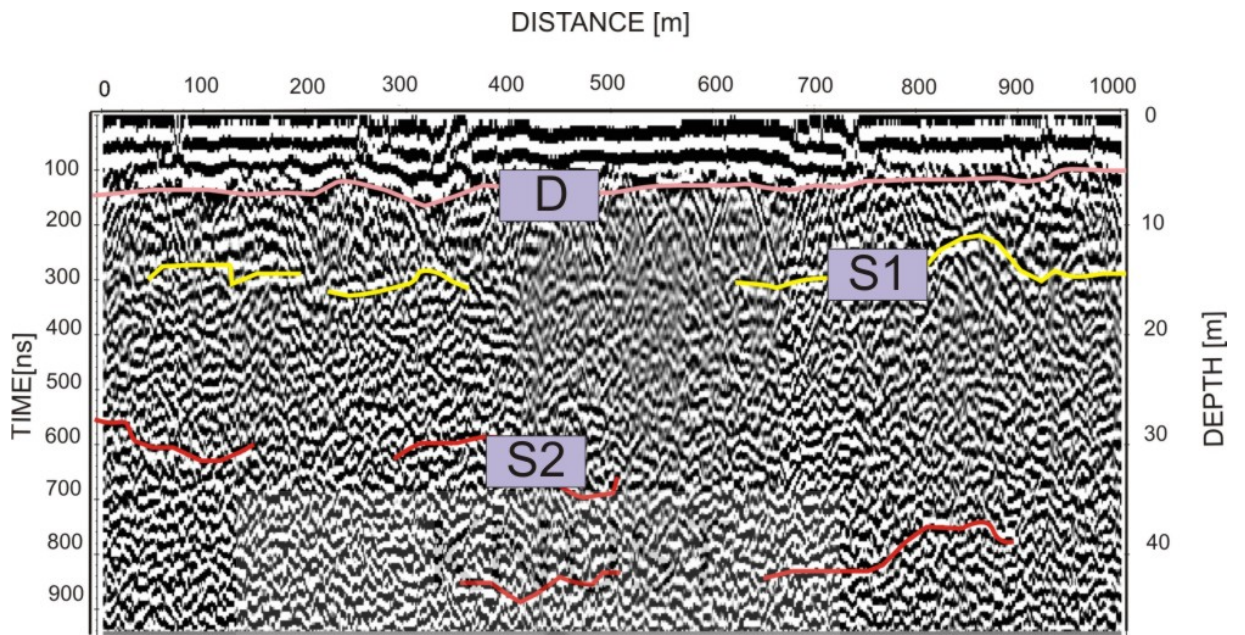


Figure 5.5: Radar Section of profile 2100E/3000N

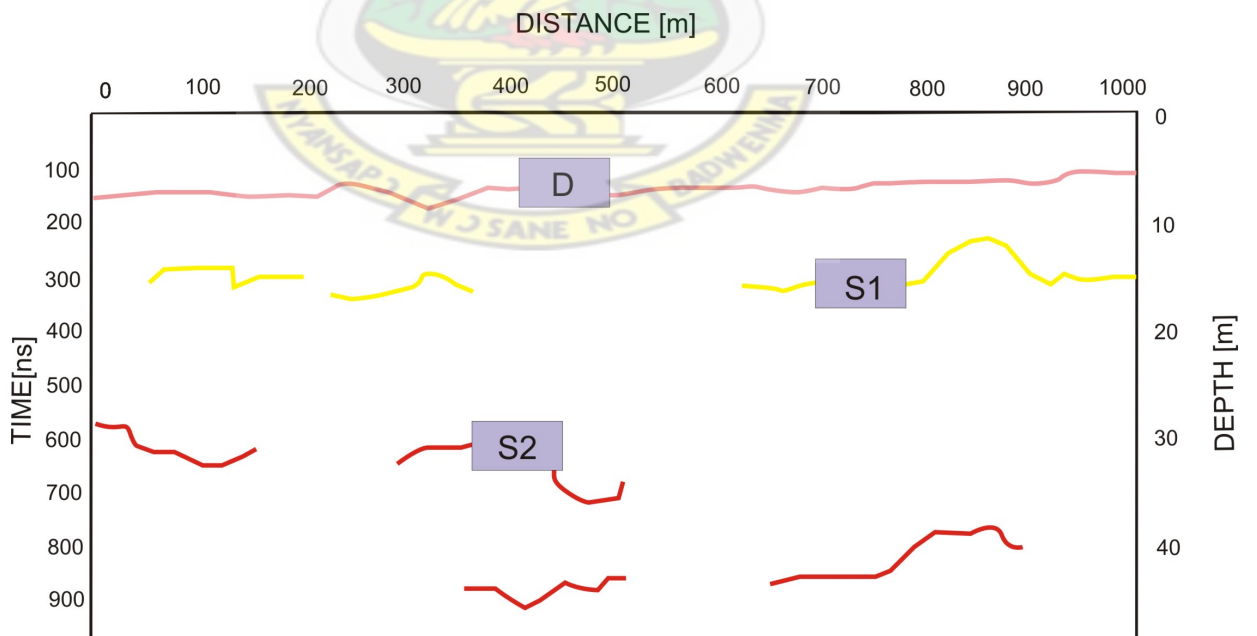


Figure 5.6: Inferred structures hosting mineralization of profile 2100E/3000N

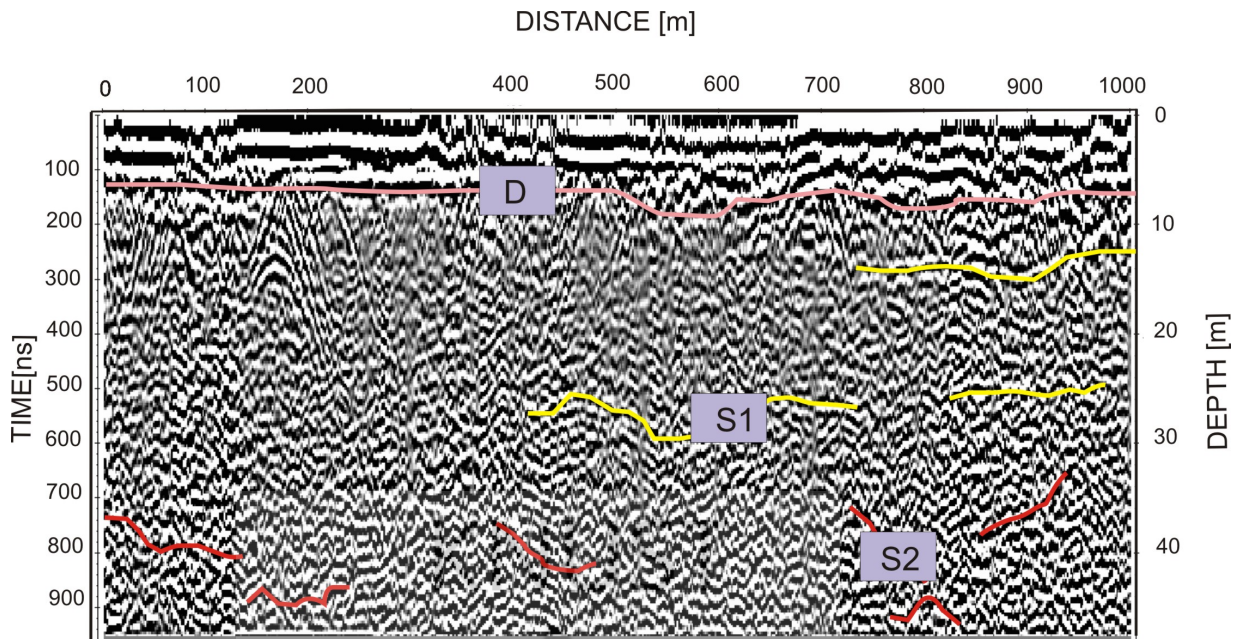


Figure 5.7: Radar Section of profile 2150E/2000N

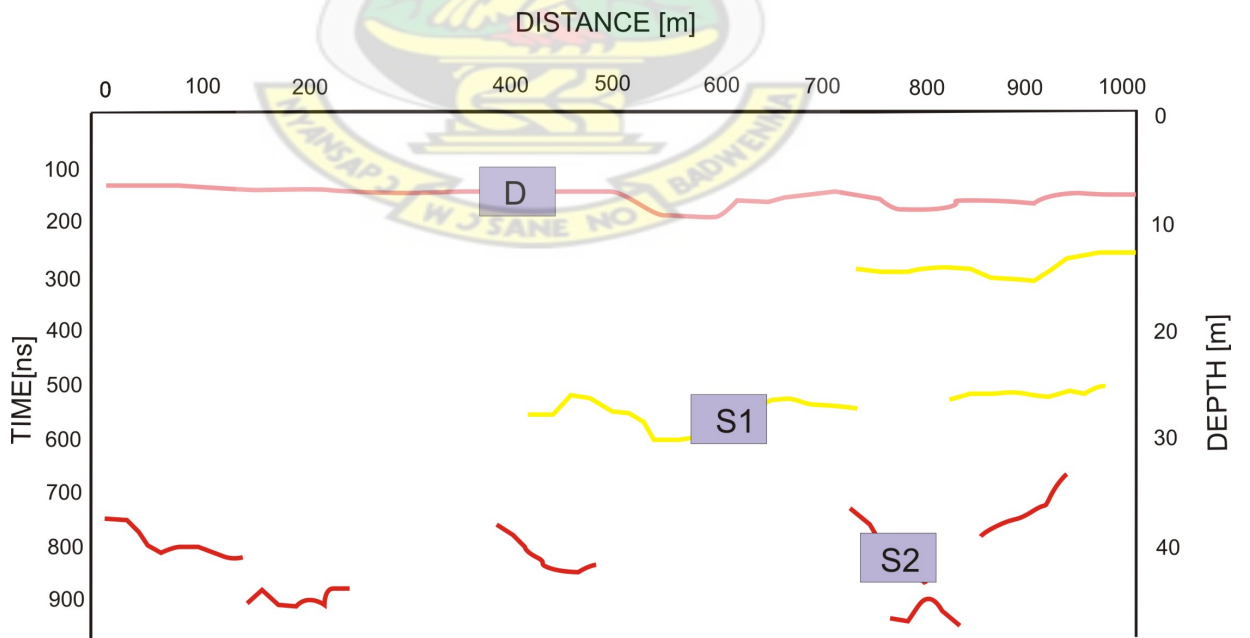


Figure 5.8: Inferred structures hosting mineralization of profile 2150E/2000N

5.1.1.4 Traverse 4: Line 2150E/2000N

The results of line 2150E/2000N are represented in Figure 5.7 and Figure 5.8. The radargram clearly shows a horizontal reflector interface marked by D at an average depth of 6 m. This top most layer is interpreted as the duracrust which overlain the Saprolite. From the radargram obtained, it was possible to identify hyperbolic diffractions between stations 0 and 200 m located at depths of about 6 m and 14 m. These hyperbolic reflectors are interpreted as just air reflections and are of no geological significance. Furthermore, horizontal, sub-horizontal and sub-vertical reflectors are also seen between the depth range of 13 m and 45 m. Two sets of structures are delineated as shown in Figure 5.8. These structures are marked by S1 and S2. These sets of structures show discontinuities and are quite undulating. S1 and S2 structures are inferred structures interpreted as possible zones hosting mineralization.

5.1.1.5 Traverse 5: Line 2200E/3000N

The results of profile 2200E/3000N are shown in Figure 5.9 and Figure 5.10. This profile shows similar features as that of line 2150E/2000N. The depth range where there are signs of horizontal reflectors is 30 m and 44 m. These structures marked by S1 and S2 are possible gold hosting structures hosting gold mineralization.

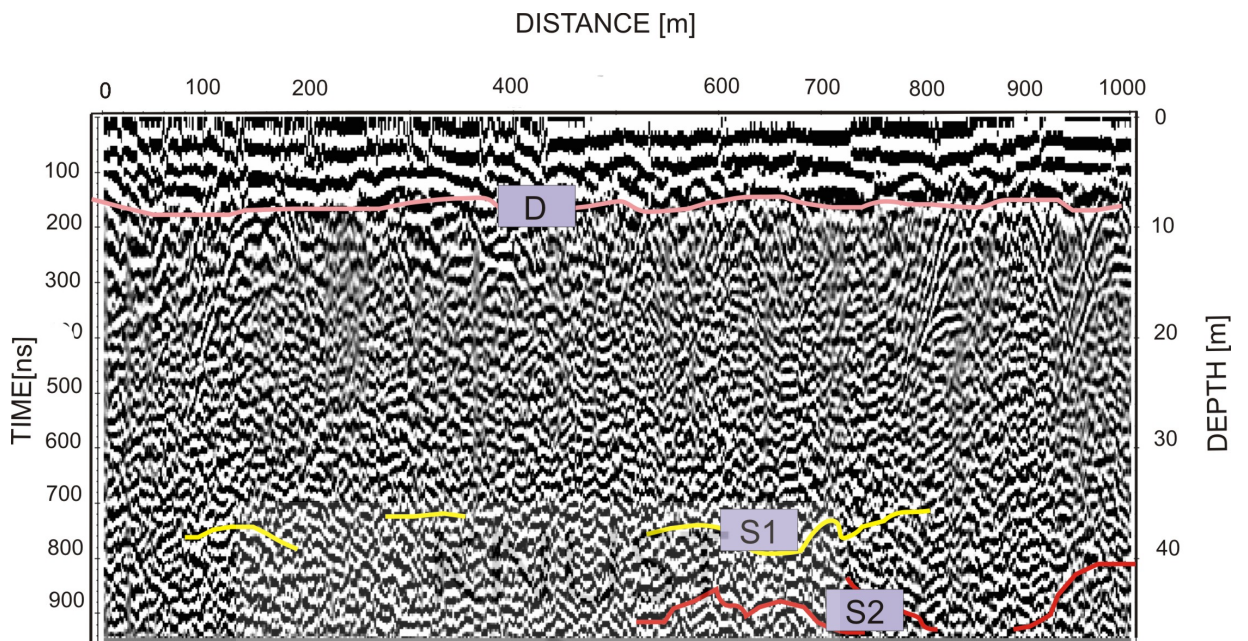


Figure 5.9: Radar Section of profile 2200E/3000N

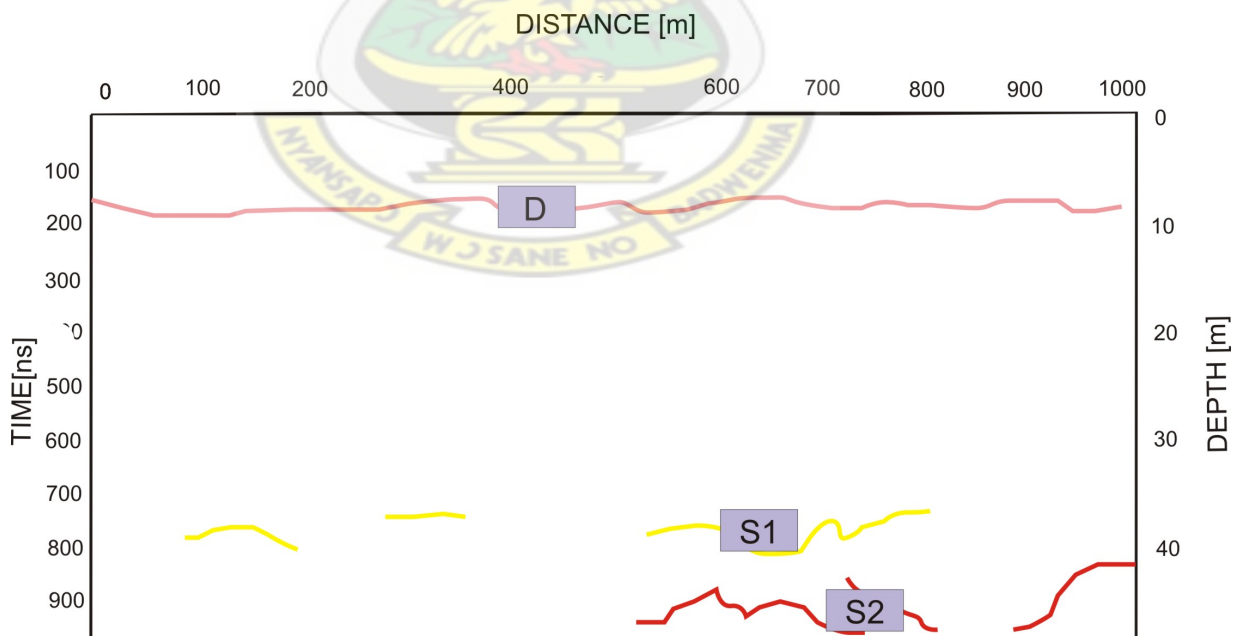


Figure 5.10: Inferred structures with potential of hosting gold mineralization of profile 2200E/3000N

5.1.1.6 Traverse 6: Line 2250E/2000N

Figure 5.11 and Figure 5.12 show the results of line 2250E/2000N. The topmost layer marked by D delineated at depth of 6 m represents the duracrust which overlain the thick Saprolite cover. The radargram shows hyperbolic diffractions at depths between 6 m and 10 m along the 1 km profile length. These structures are interpreted as noise resulting from air reflections and reflections from tree roots. These structures are of no geological significance as far as this work is concerned. There is also a clear evidence of successive diffraction hyperbolas at profile distances of 170 m, 340 m and 520 m which extends to the entire depth of approximately 50 m.

These sets of structures are interpreted as noise caused by an unseen field operation or may be due to diffractions from trees and other objects. The profile again shows a continuous reflector slightly undulating in geometry marked by S1, located at mean depths of about 30 m and 33 m between profile distances of about 560 m and 860 m. Between profile distances of 0 and 300 m at depths of about 28 m 33 m S1 structures are again seen. Below this there is a discontinuous reflector indicating a possible structure zone S2 . The major undulating sub horizontal reflectors are observed between the depths of 35 m and 44 m with slightly dipping features. These structures are indicated in red color designated by S2. This profile line is not highly weathered, but show moderate fracturing. The possible zones where mineralization may occur are the S1 and S2 inferred structures.

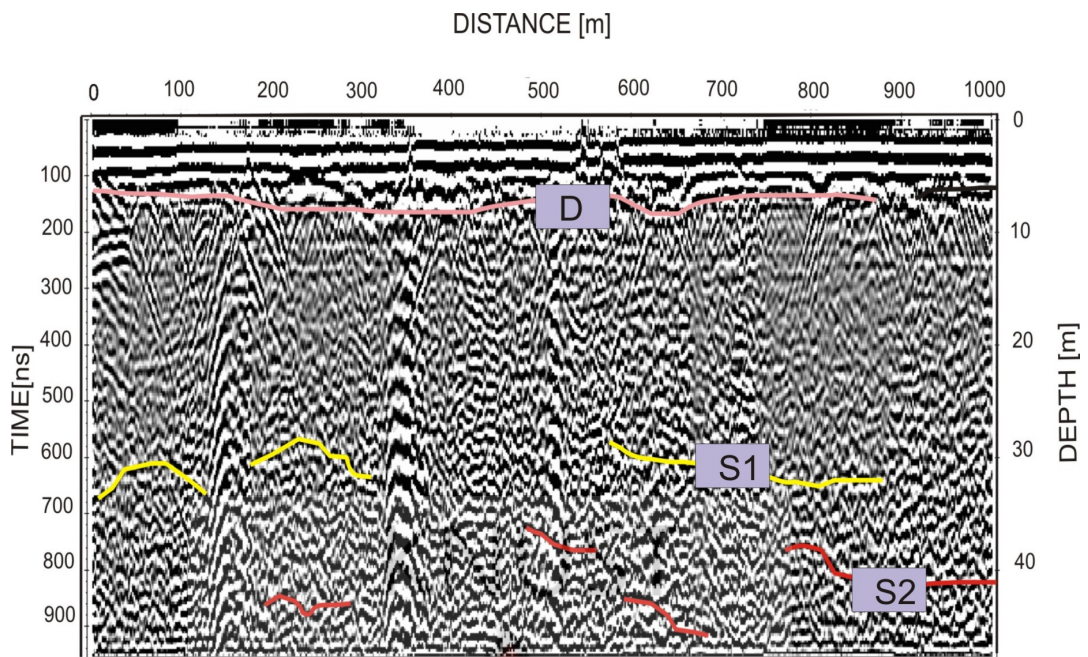


Figure 5.11: Radar Section of profile 2250E/2000N

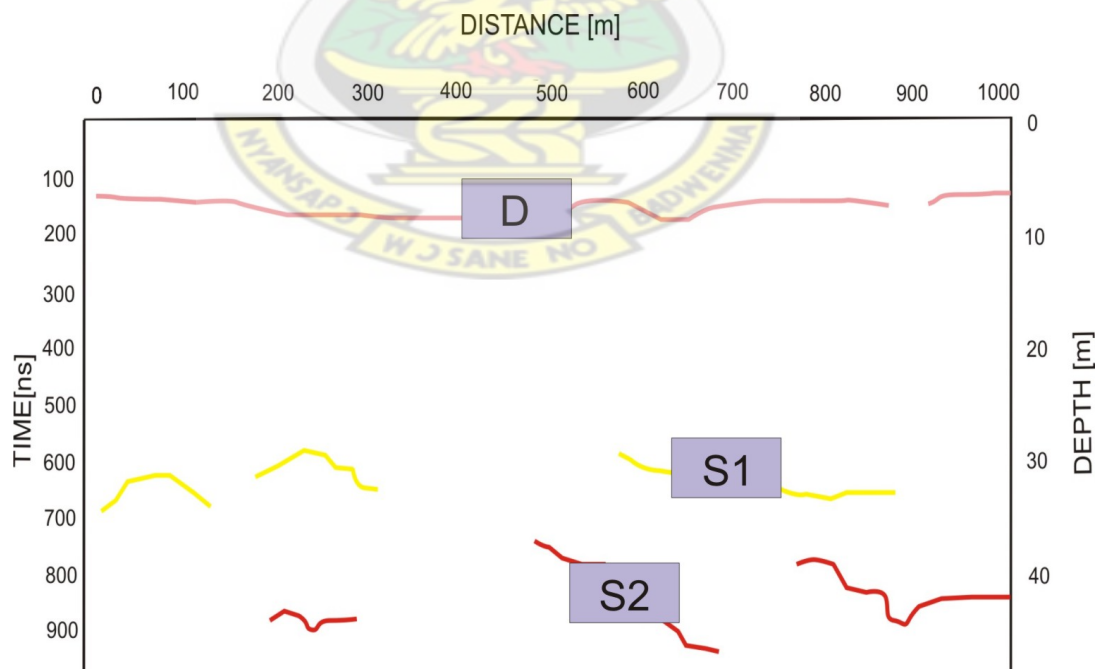


Figure 5.12: Inferred structures with potential of hosting gold mineralization of profile 2250E/2000N

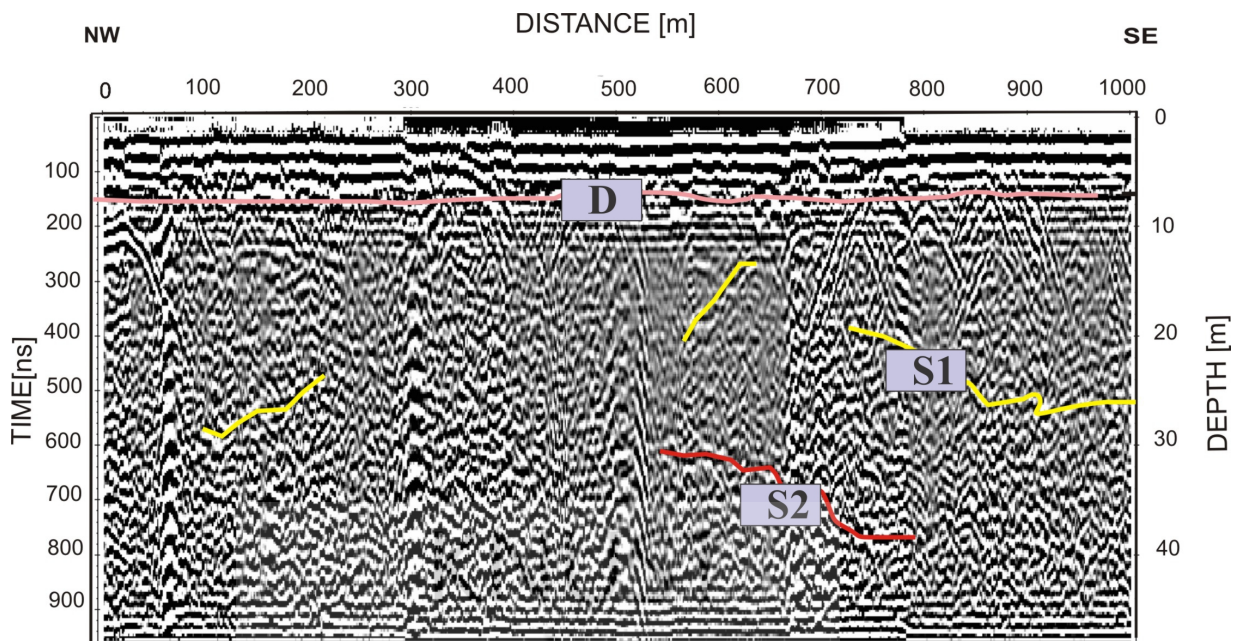


Figure 5.13: Radar Section of profile 2300E/3000N

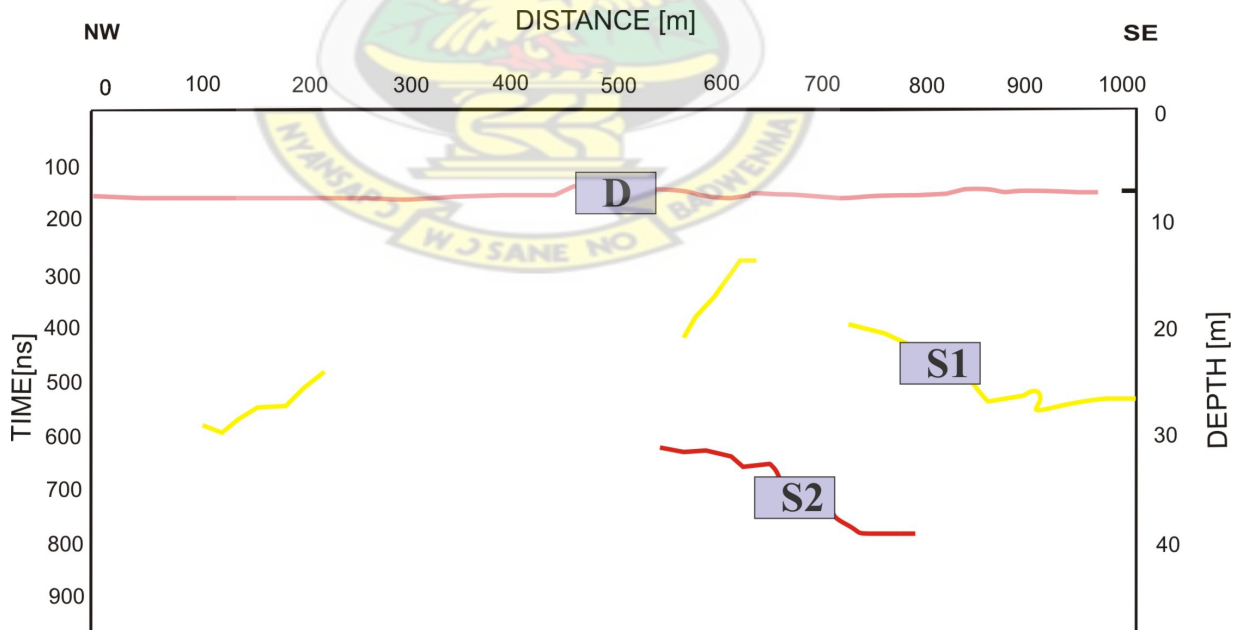


Figure 5.14: Inferred structures with potential of hosting gold mineralization of profile 2300E/3000N

5.1.1.7 Traverse 7: Line 2300E/3000N

Figure 5.13 and its inferred structure plot Figure 5.14 illustrate the results of line 2300E/3000N. From Figure 5.13, the topmost layer designated by D which is delineated at mean depth of about 6 m represents the thickness of the duracrust. Two sets of structures S1 and S2 can be identified in Figure 5.13 and Figure 5.14. First and foremost, there is a horizontal dipping reflector S1 with an approximate length of about 300 m at located at depths of 19 m and 28 m. Below this structure lies slightly undulating horizontal reflector also dipping S2 between the depths of 32 m and 40 m between the profile distances of 540 m and 800 m. The two sets of structures identified in this profile can be interpreted as inferred structures where gold mineralization may occur.

5.1.1.8 Traverse 8: Line 2350E/2000N

Figure 5.15 and Figure 5.16 show the results of line 2350E/2000N. As usual, there is a clear evidence of a duracrust marked by D in pink color with a mean thickness of 6 m. The radargram clearly shows numerous hyperbolic diffractions between the depth range of 6 m and 16 m throughout the entire profile length. These structures are basically noise as a result of diffractions from the air and trees. The entire profile is highly weathered with less structures. The prominent structures are shown by the S1 and S2 features. The S1 structural feature is clearly delineated and are located between the profile distances of 0 and 240 m, and 340 m and 580 m. the S2 structure also show some occurrences between the depth range of 45 m and 48 m. These structures are undulating in geometry and discontinuous. The possible zones suitable for the occurrences of mineralization are the inferred structures shown in Figure 5.16 fractures.

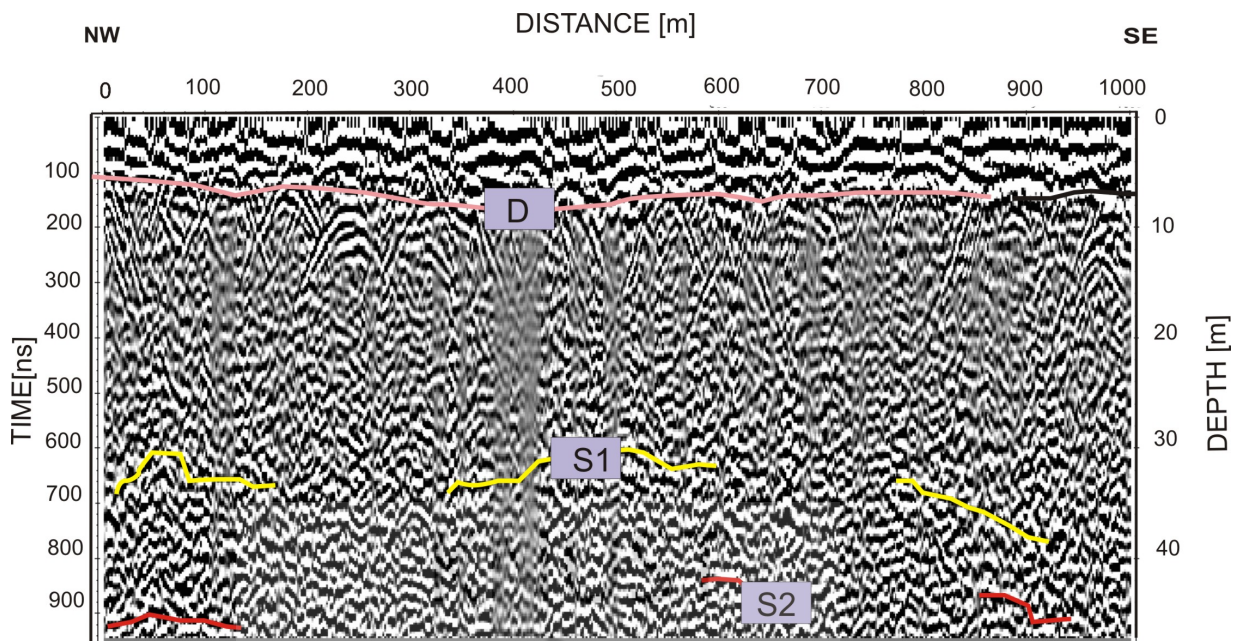


Figure 5.15: Radar Section of profile 2350E/2000N

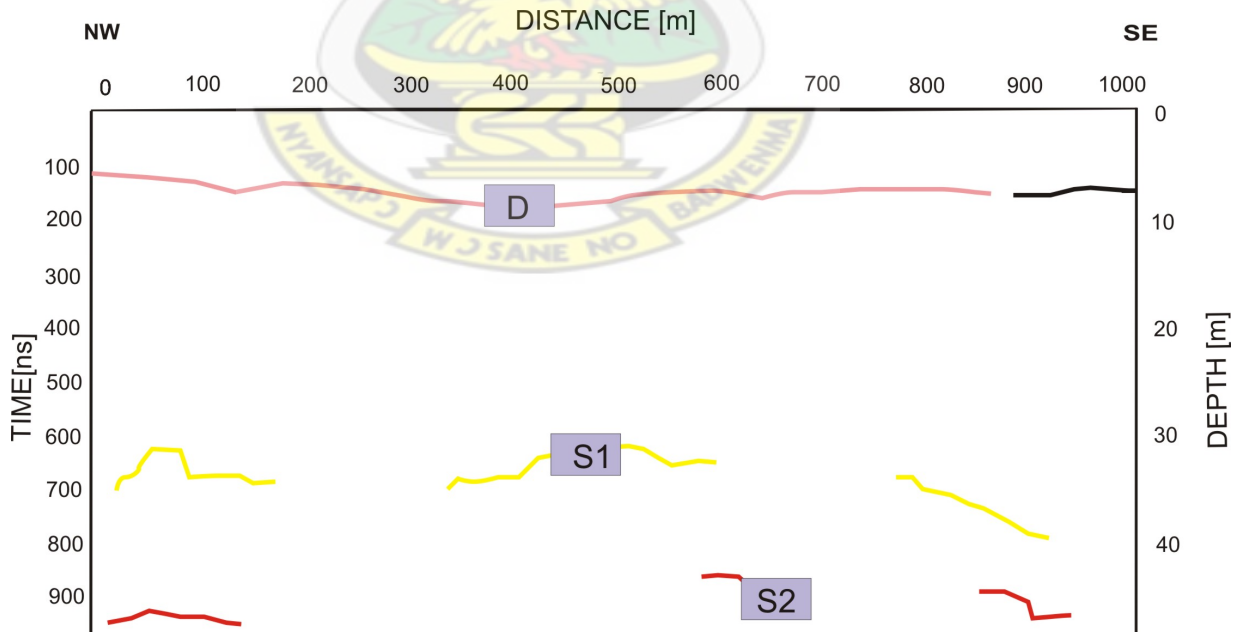


Figure 5.16: Inferred structures with potential of hosting gold mineralization of profile 2350E/2000N

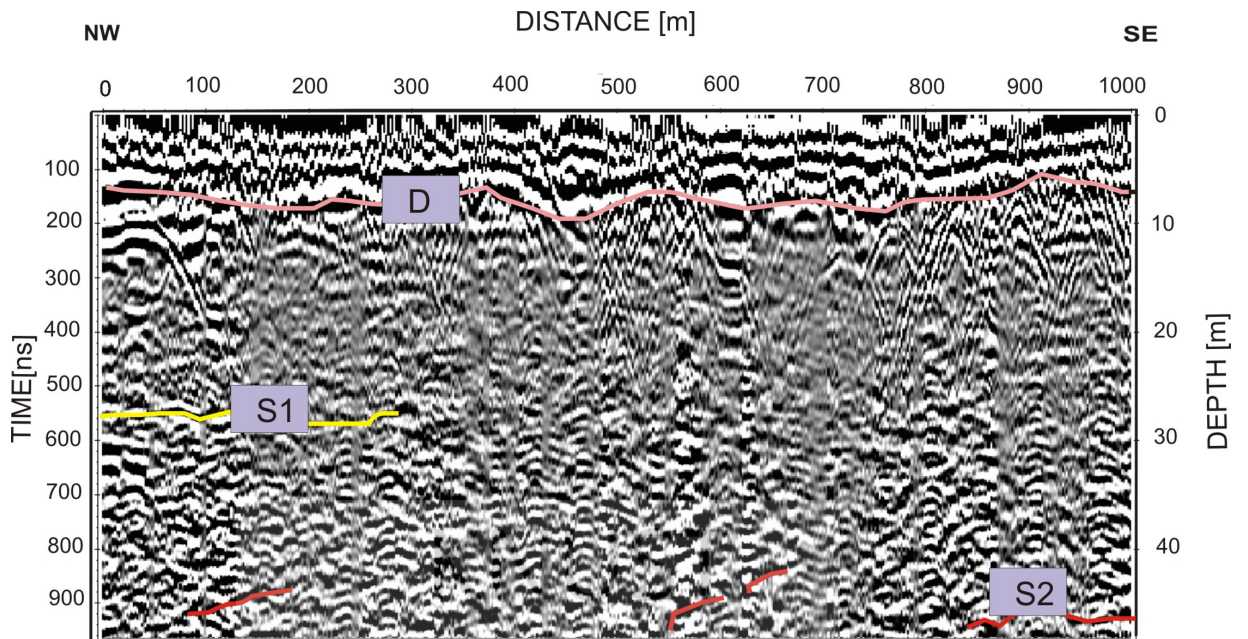


Figure 5.17: Radar Section of profile 2400E/3000N

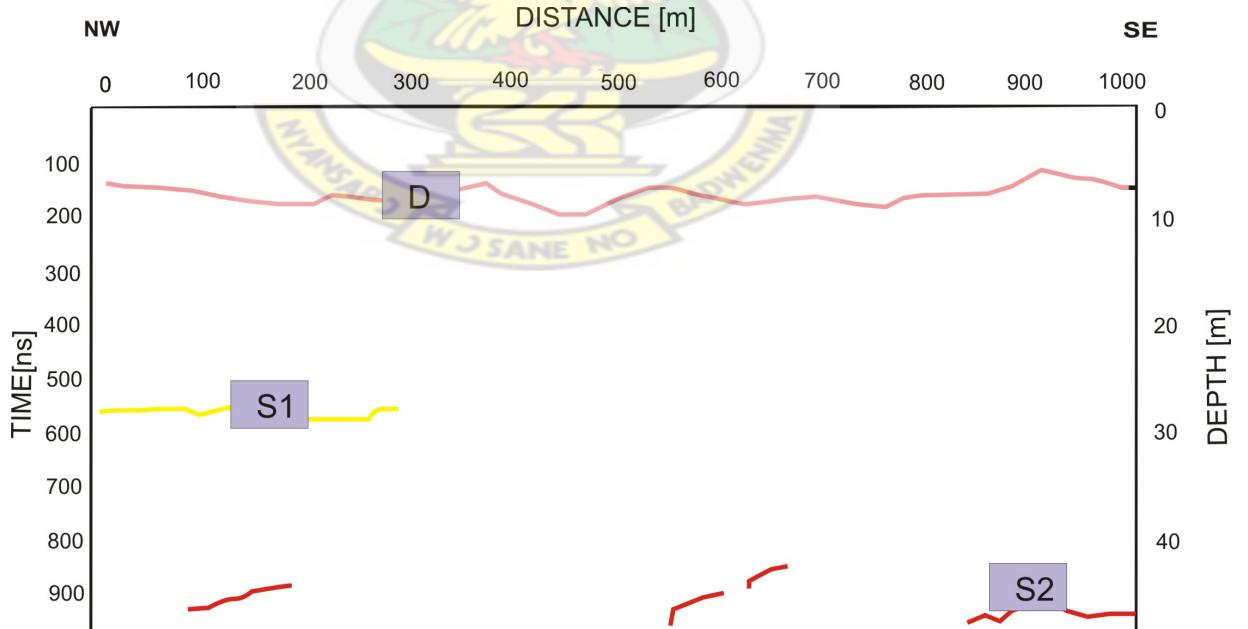


Figure 5.18: Inferred structures with potential of hosting gold mineralization of profile 2400E/3000N

5.1.1.9 Traverse 9: Line 2400E/3000N

Figure 5.17 and Figure 5.18 illustrate the results of line 2400E/3000N. The layer with the pink color marked by D represents the depth of the topmost layer which constitute the duracrust. The duracrust has an average depth of 6 m. There are many diffraction patterns between stations 500 m and 1000 m at depth range of 6 m and 13 m while there are no diffraction patterns between stations 0 and 500 m. These hyperbolic structures are interpreted as just mere air reflections. Though the radargram shows much weathering throughout the entire profile length with near horizontal reflector S1 extending from NW to SE between the profile stations 0 and 300 m. Furthermore there is a clear indication of a weak discontinuous undulating Structure S2 between the depths of 42 m and 46 m. Most probably, these inferred structures are the zones that might host gold mineralization.

5.1.1.10 Traverse 10: Line 2450E/2000N

The results of line 2450E/2000N are represented in Figure 5.19 and Figure 5.20. Figure 5.19 clearly shows many hyperbolic reflectors just below the duracrust layer marked by D. This duracrust has a mean thickness of 8 m in this profile. The hyperbolic reflectors are interpreted as reflections from trees and roots of trees. These are disturbances that may preclude the data set. just below this hyperbolas lies a strong horizontal slightly undulating reflector S1 extending from 300 m to 760 m and dipping towards SE along the profile. The entire profile shows much weathered formation and also have some discontinuous sub-horizontal reflectors S2 between the depth range of about 40 m and 46 m. It is interpreted that, the saprolite is composed of layers of undulating structures and highly weathered zones probably hosting mineralization. These structures are inferred of hosting gold mineralization.

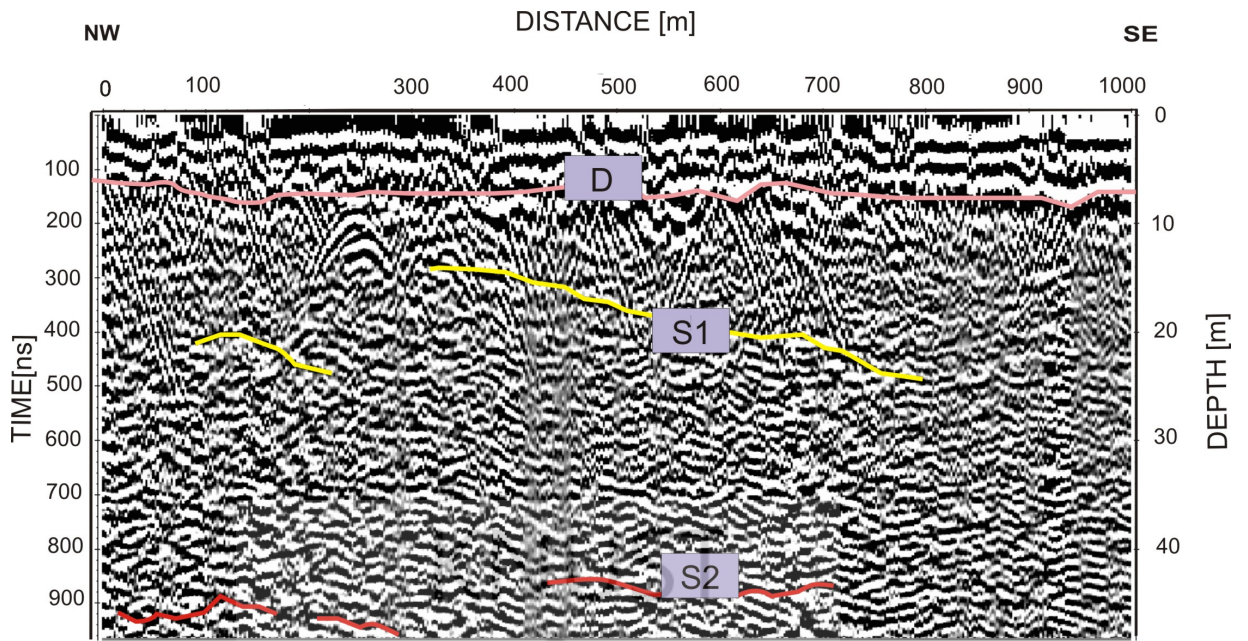


Figure 5.19: Radar Section of profile 2450E/2000N

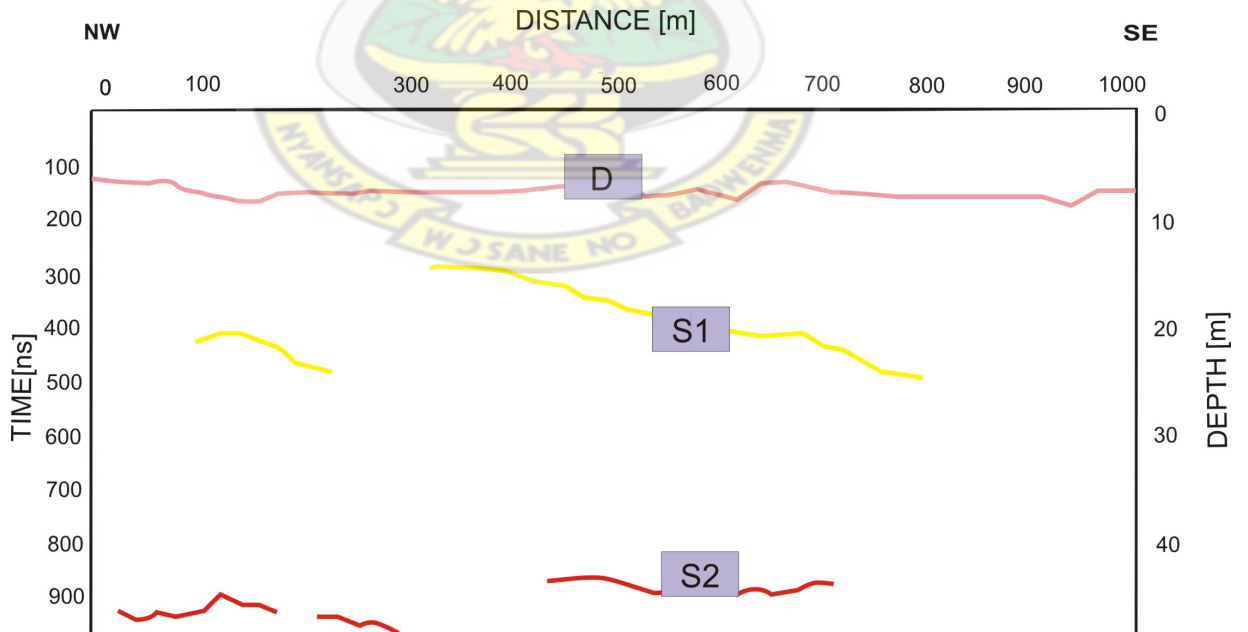


Figure 5.20: Inferred structures with potential of hosting gold mineralization of profile 2450E/2000N

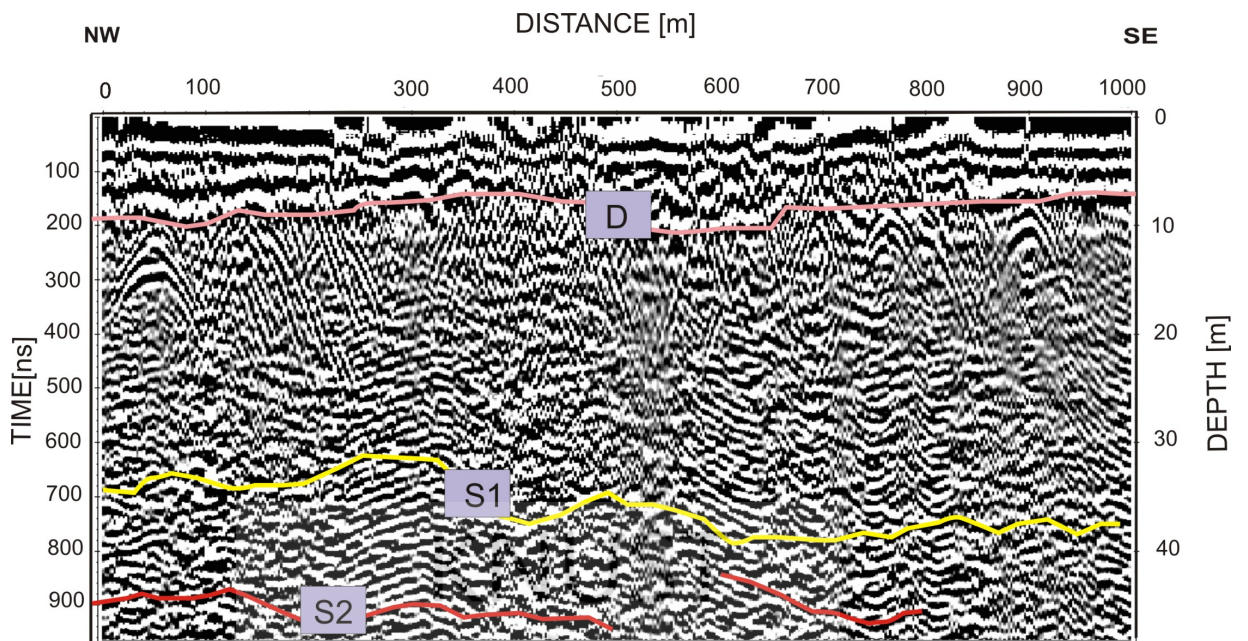


Figure 5.21: Radar Section of profile 2500E/3000N

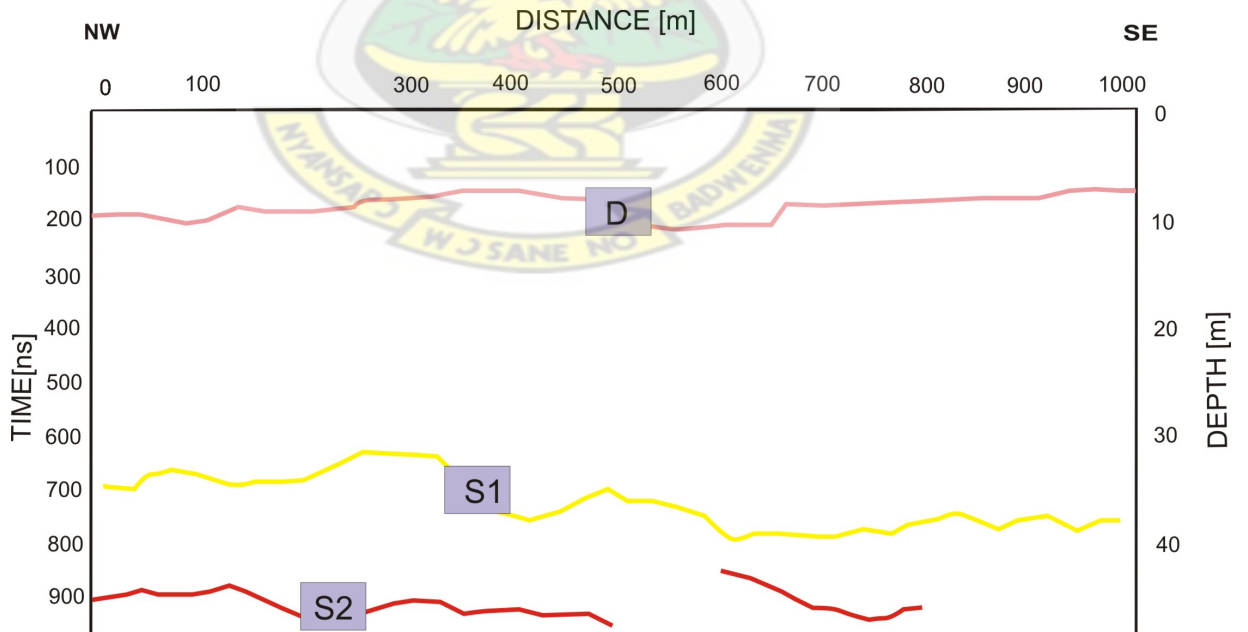


Figure 5.22: Inferred structures with potential of hosting gold mineralization of profile 2500E/3000N

5.1.1.11 Traverse 11: Line 2500E/3000N

The results of line 2500E/3000N are represented in Figure 5.21 and Figure 5.22. The pink layer marked D clearly shows the contact zone between the duracrust and the Saprolite. Between the depth range of 34 m and 40 m, there is a continuous undulating reflector marked S1. This structure extends throughout the entire profile length. Below this lies a non-continuous undulating horizontal reflector S2 between the depth range of 44 m and 48 m. Between these two layers, one could clearly see the weathered zone, which shows S2 structure which extends from 0 m to about 500 m at the SW corner of the profile at the profile length of 0 and 500 m. The indicated structures S1 and S2 are interpreted as inferred structures probably hosting gold mineralization. On the other hand, there are numerous hyperbolic diffractions between the depth range of 8 m and 18 m. These are interpreted as just mere air reflections, and show no geological significance.

5.1.1.12 Traverse 12: Line 2550E/2000N

Figure 5.23 and Figure 5.24 show the results of line 2550E/2000N. The radargram Figure 5.23 from this traverse has shown the presence of a highly deformational structures S1 and S2. trends of structures are horizontal trending NW to SE. Unlike the other radargrams presented for the previous profiles, there is a moderate structural anomaly S1 between the depths of 25 m and 30 m which spreads out over the entire profile length of 1000 m. Continuous structure S2 also noticed at the depth of 42 m.

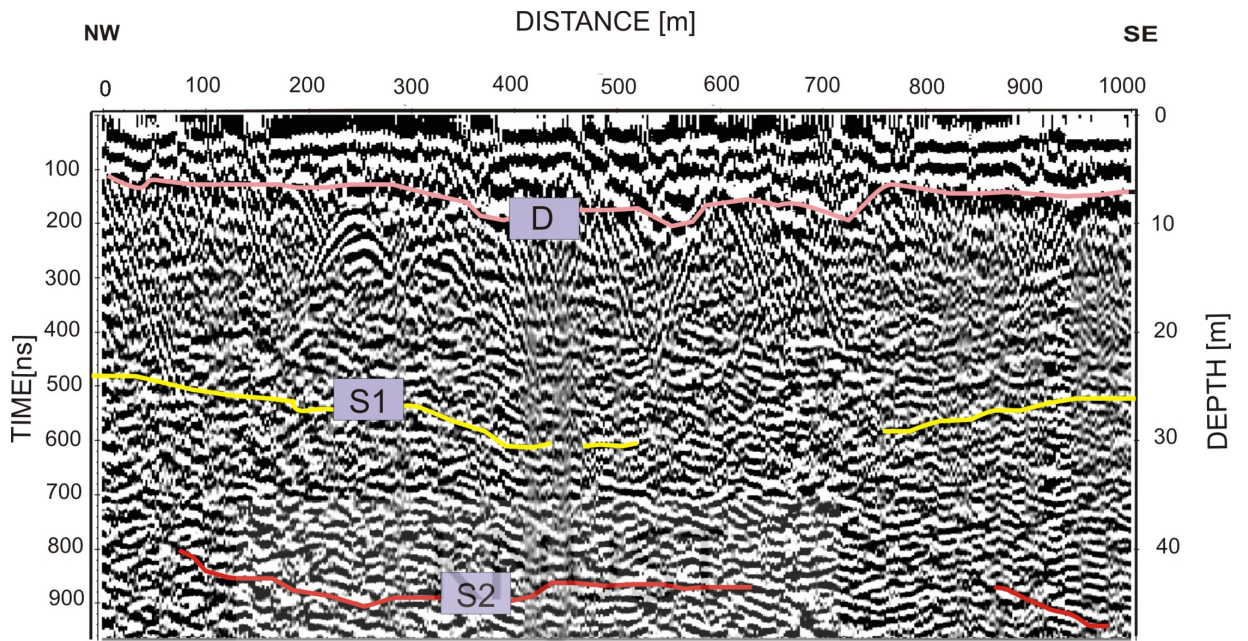


Figure 5.23: Radar Section of profile 2550E/2000N

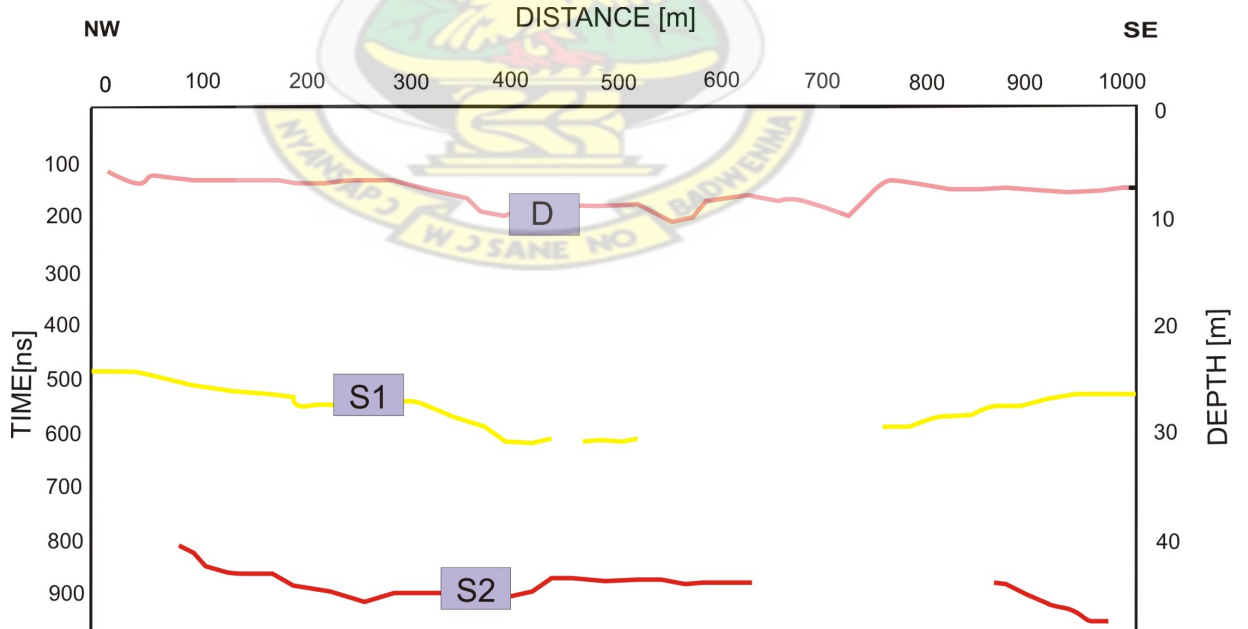


Figure 5.24: Inferred structures with potential of hosting gold mineralization of profile 2550E/2000N

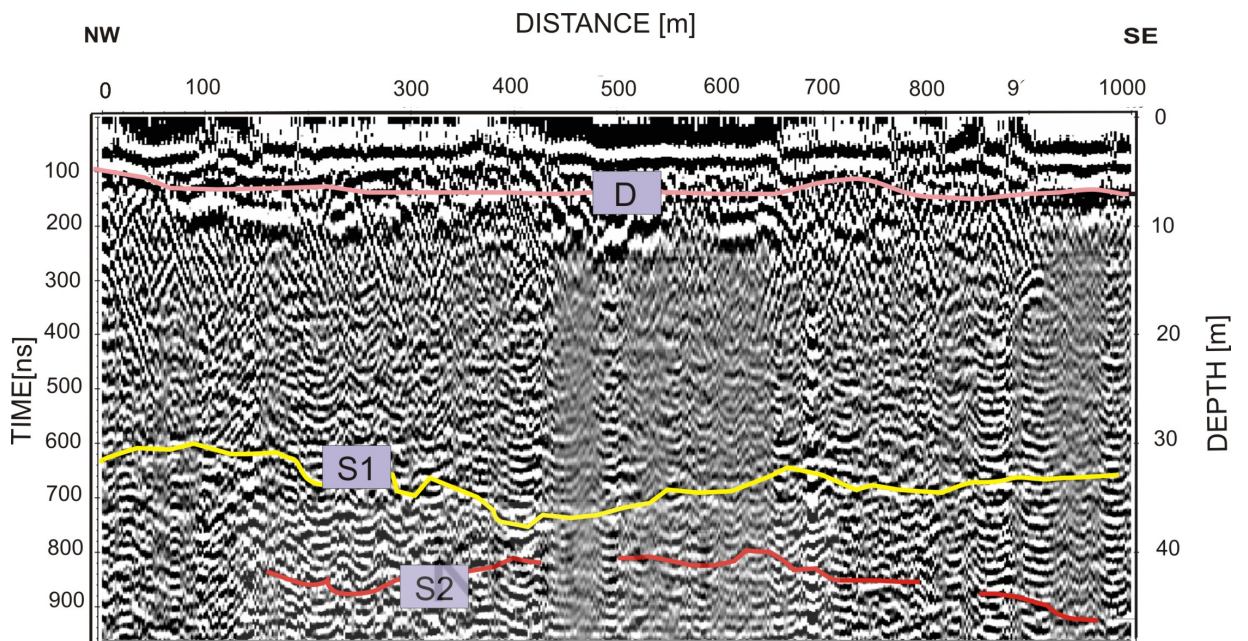


Figure 5.25: Radar Section of profile 2600E/3000N

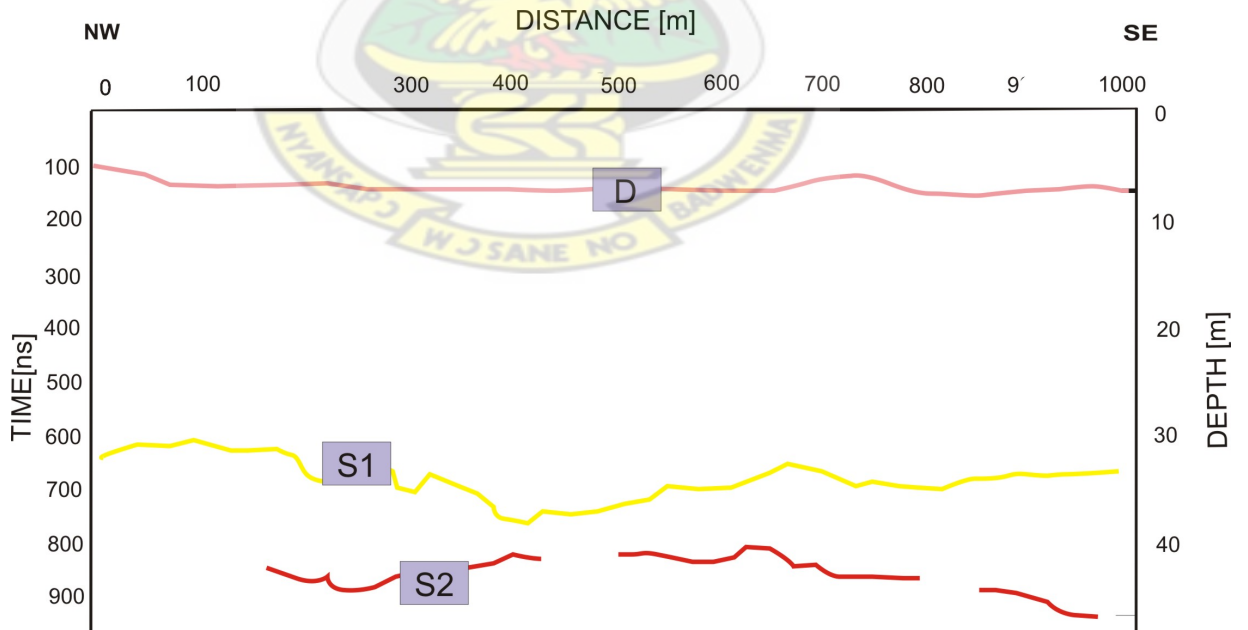


Figure 5.26: Inferred structures with potential of hosting gold mineralization of profile 2600E/3000N

5.1.1.13 Traverse 13: Line 2600E/3000N

The results of line 2600E/3000N are represented in Figure 5.25 and Figure 5.26. Looking at the radar scene in Figure 5.25, the pink line at the topmost layer D is interpreted as the duracrust with a thickness of approximately 7 m. Below 10 m depth, there are a lot of reflection patterns characterized by a group of south-west dipping reflectors. Between the depths of about 30 m and 36 m, there is a continuous sub-horizontal structure S1 which runs from 0 to 1000 m. On the other hand, discontinuous structure S2 can also be identified. These structures are interpreted as the possible oxidized zones within the weathered Saprolite where mineralization may occur.

5.1.1.14 Traverse 14: Line 2650E/2000N

Figure 5.27 and Figure 5.28 show the results of line 2650E/2000N. The radargram interpretation in Figure 5.27 shows the depth of the duracrust which is about 6 m thick. This layer is indicated in the pink color by D. There are a lot of hyperbolic diffractions between the depth range of about 6 m and 16 m. These hyperbolic diffractions are as a result of air reflections. they are considered as noise with no geological significance. Furthermore, there are high degrees of structures present at the depth range of about 20 m and 50 m. These set of structures are marked by S1 and S2 as indicated in Figure 5.28. These set of inferred structures probably plays a vital role in defining the mineralized zones within the saprolite.

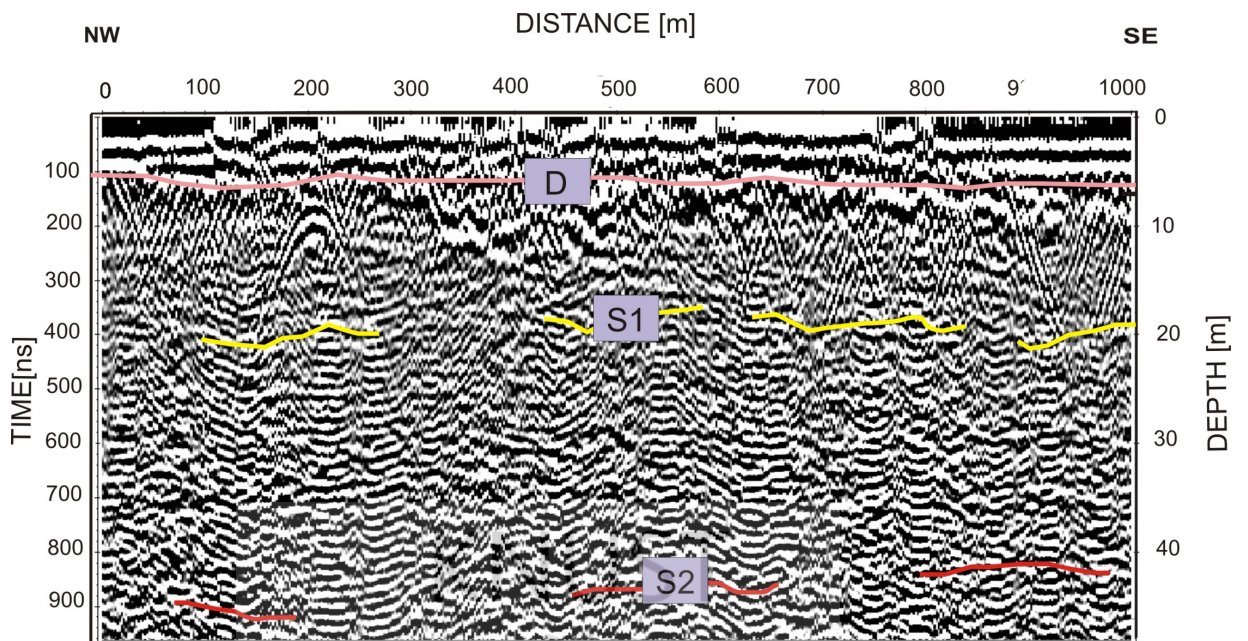


Figure 5.27: Radar Section of profile 2650E/2000N

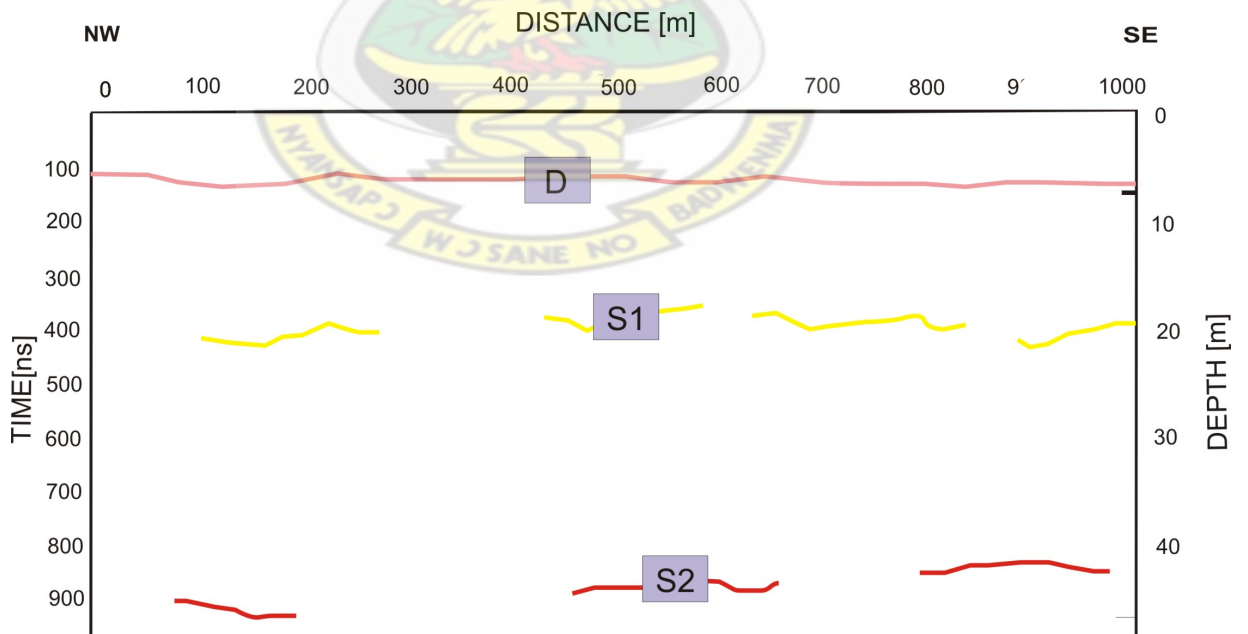


Figure 5.28: Inferred structures with potential of hosting gold mineralization of profile 2650E/2000N

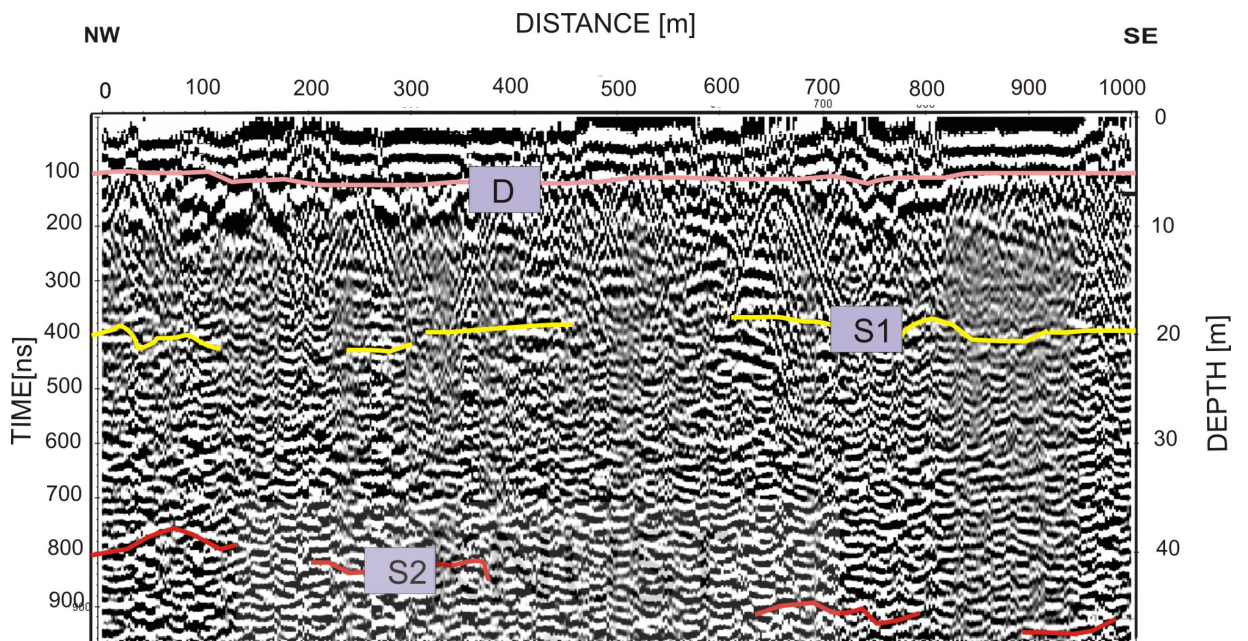


Figure 5.29: Radar Section of profile 2700E/3000N

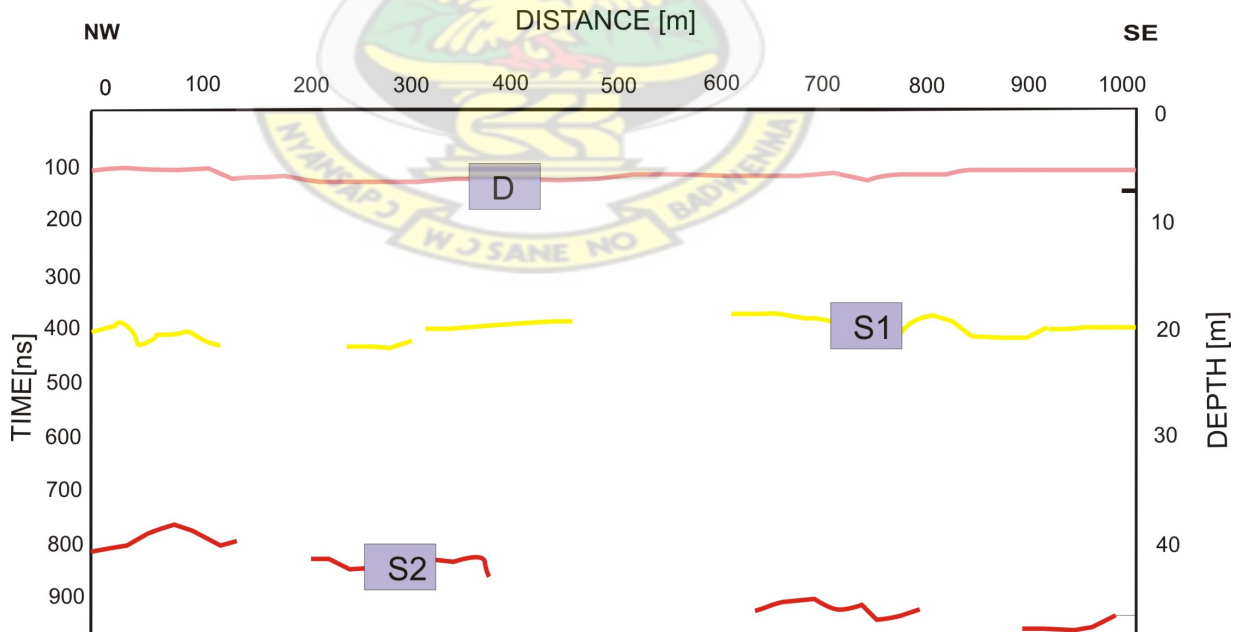


Figure 5.30: Inferred structures with potential of hosting gold mineralization of profile 2700E/3000N

5.1.1.15 Traverse 15: Line 2700E/3000N

Figure 5.29 and Figure 5.30 illustrate the results of line 2700E/3000N. The topmost layer marked D indicates the thickness of the duracrust. The radargram and its interpretation plot clearly shows a lot of hyperbolic diffractions between the depths of 6 m and 20 m. As in the other profiles, these structures are noise that have precluded the data. The profile shows a moderately strong continuous reflector S1 slightly undulating in geometry, located at a mean depth of 19 m and 21 m which is between the profile distances of 600 m and 1000 m. Below this, noncontinuous undulating strong reflectors S2 appear. The most prominent ones appears at depth range of 34 m and 40 m which represents the S2 structure. The radar scene for this line is characterized by a weak sub-horizontal reflectors. The interpretation to this profile is that, fracturing zones are not much pronounced and this zone show less weathering.

5.1.1.16 Traverse 16: Line 2750E/2000N

The results of line 2750E/2000N are represented in Figure 5.31 and Figure 5.32. The radargram Figure 5.31 clearly shows a duracrust layer marked D with the pink color at a depth of approximately 5 m. The depth range of 6 m to 15 m is masked by hyperbolic diffractions. These hyperbolas are interpreted as noise. They are really diffractions from air and trees and base on that effect, these structures are of no geological significance as far as this work is concerned. Between profile distances of about 0 and 300 m at depths of 30 m and 40 m shows S1 structure. There is a clear evidence of a strong reflector undulating in geometry located at a mean depth of 33 m and 38 m. Furthermore, there is also an undulating reflector extending at about 250 m long between profile stations of 750 m and 1000 m located at an average depth of 35 m. Below this undulating fracture zone appears a

strong discontinuous reflector S2 stretching at an average length of 280 m between profile distances of 0 to 280 m and 360 to 600 m. These structures are interpreted as intensely weathered Saprolite. Complete oxidation includes all of the saprolite and locally extends to 1 to 10 m into the primary bedrock. The primary bedrock is overlain by the saprolite.

KNUST



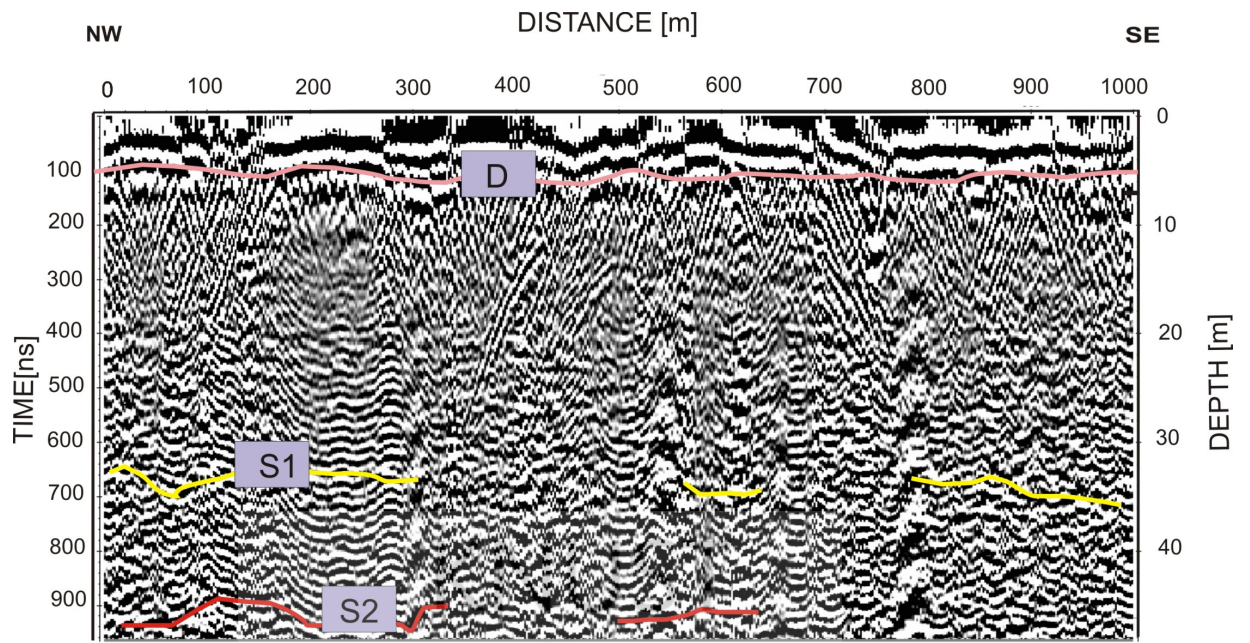
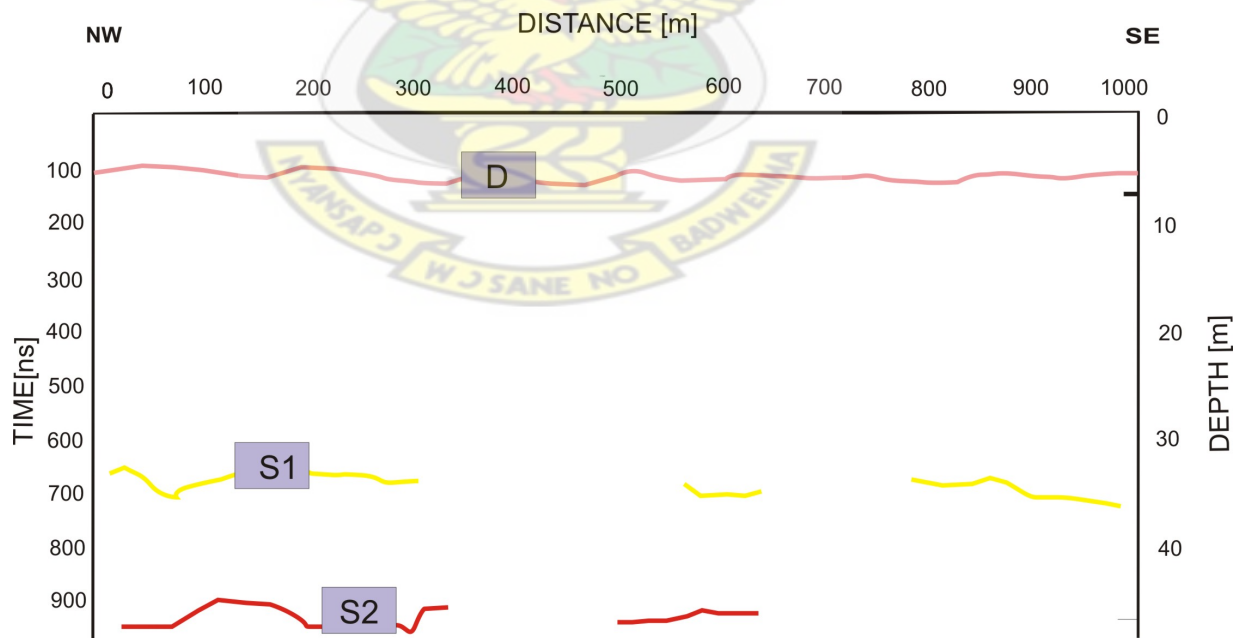


Figure 5.31: Radar Section of profile 2750E/2000N



3

Figure 5.32: Inferred structures with potential of hosting gold mineralization of profile 2750E/2000N

5.1.2 Results of 50 MHz Antenna

KNUST



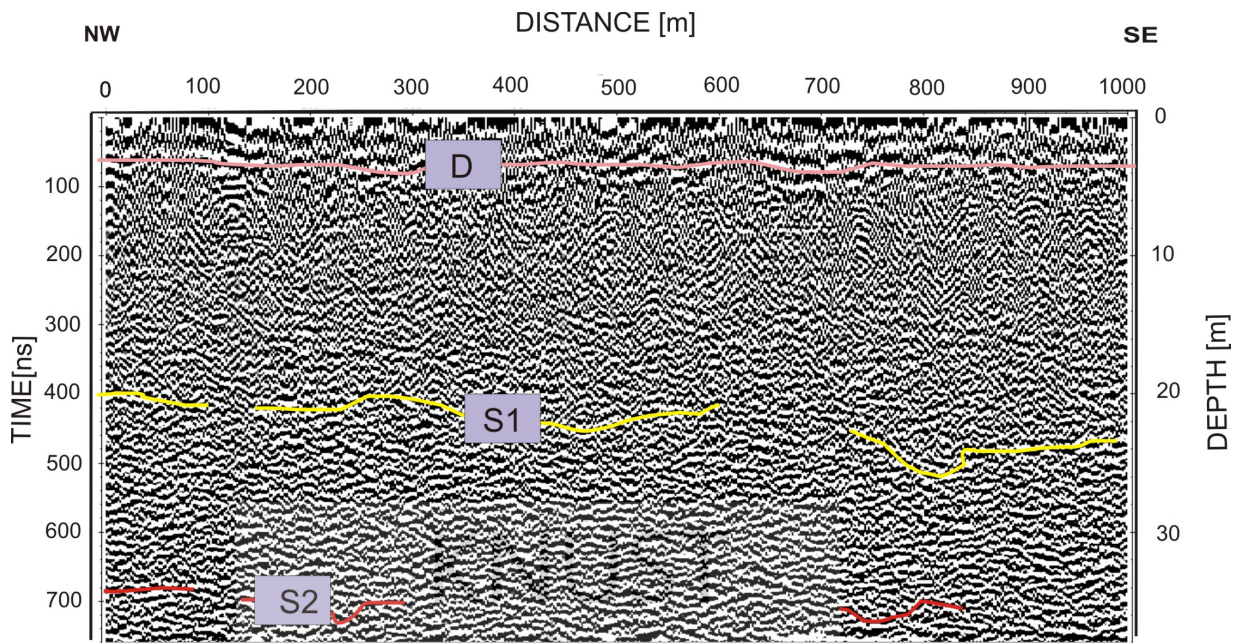


Figure 5.33: Radar Section of profile 2000E/3000N

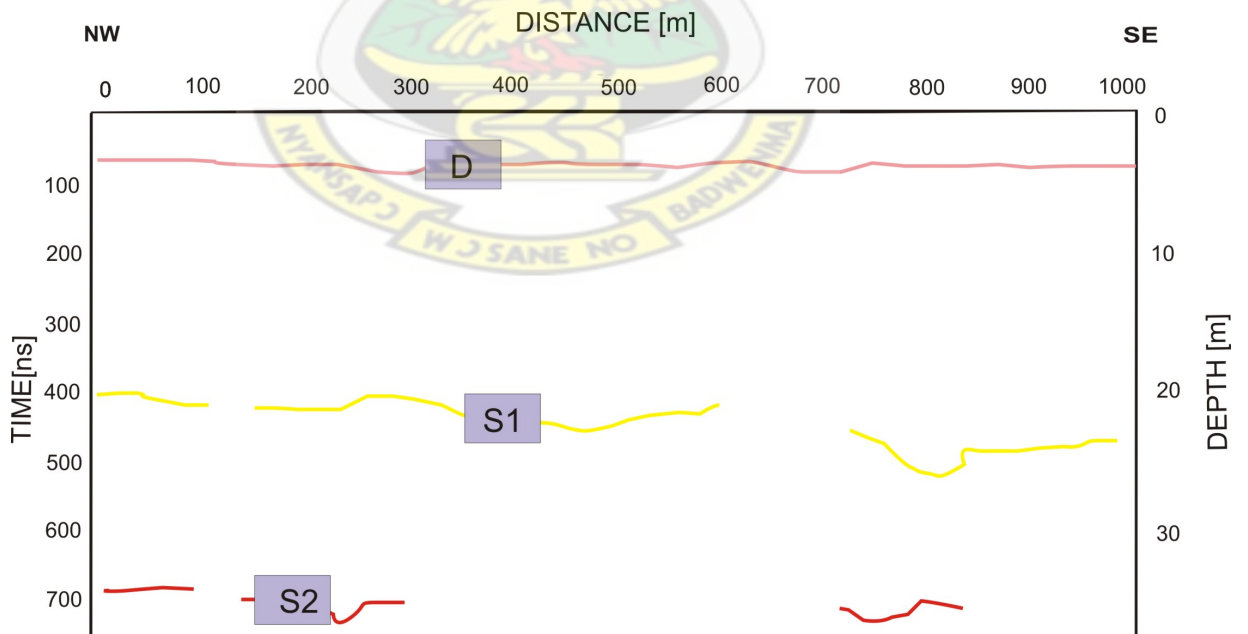


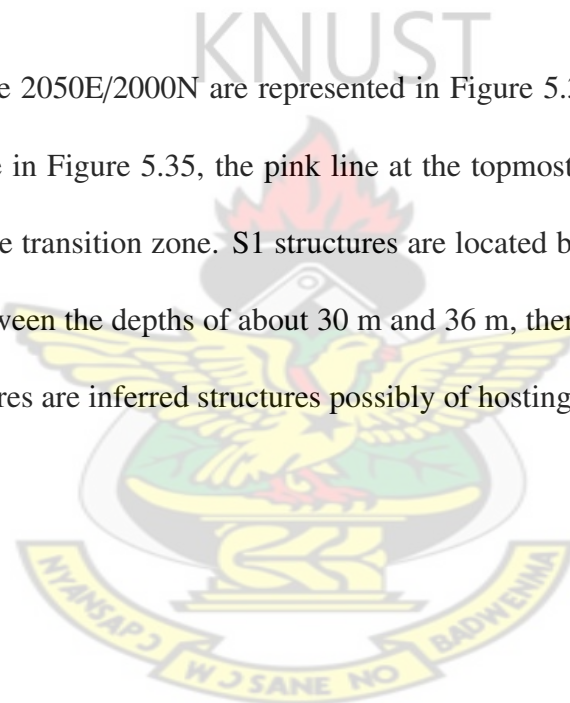
Figure 5.34: Inferred structures with potential of hosting gold mineralization of profile 2000E/3000N

5.1.2.1 Traverse 1: Line 2000E/3000N

Figure 5.33 and Figure 5.34 show the results of line 2000E/3000N. The duracrust and saprolite contact is marked by D. There is a structure marked S1 which is located at 20 m and 26 m depth range. S2 is also a structure identified between 35 m and 37 m. These structures S1 and S2 are inferred structures of hosting gold mineralization.

5.1.2.2 Traverse 2: Line 2050E/2000N

The results of line 2050E/2000N are represented in Figure 5.35 and Figure 5.36. Looking at the radar scene in Figure 5.35, the pink line at the topmost layer D is interpreted as the duracrust-saprolite transition zone. S1 structures are located between the depth range of 10 m and 20 m. Between the depths of about 30 m and 36 m, there is another structure marked S2. These structures are inferred structures possibly of hosting gold mineralization.



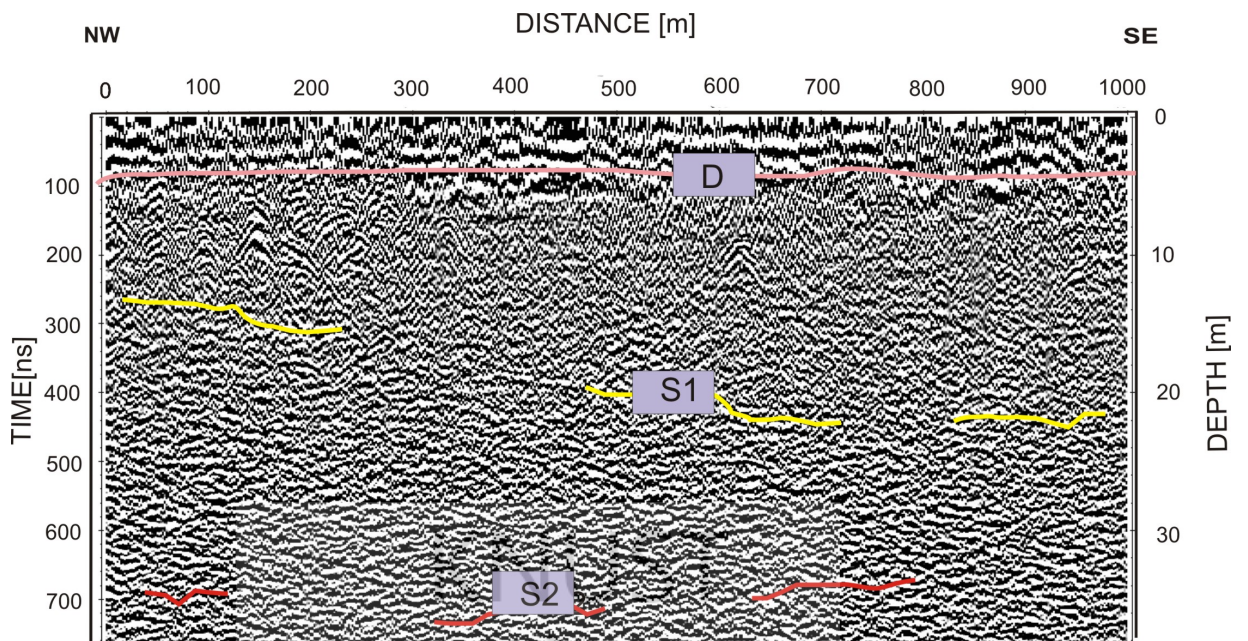


Figure 5.35: Radar Section of profile 2050E/000N

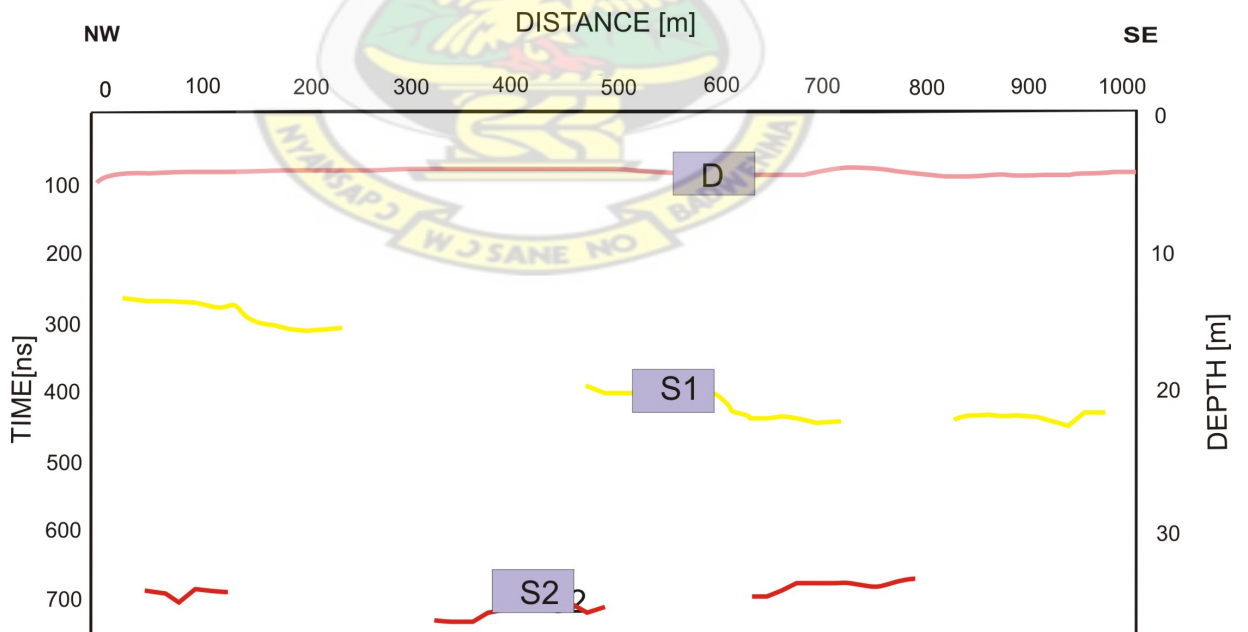


Figure 5.36: Inferred structures with potential of hosting gold mineralization of profile 2050E/2000N

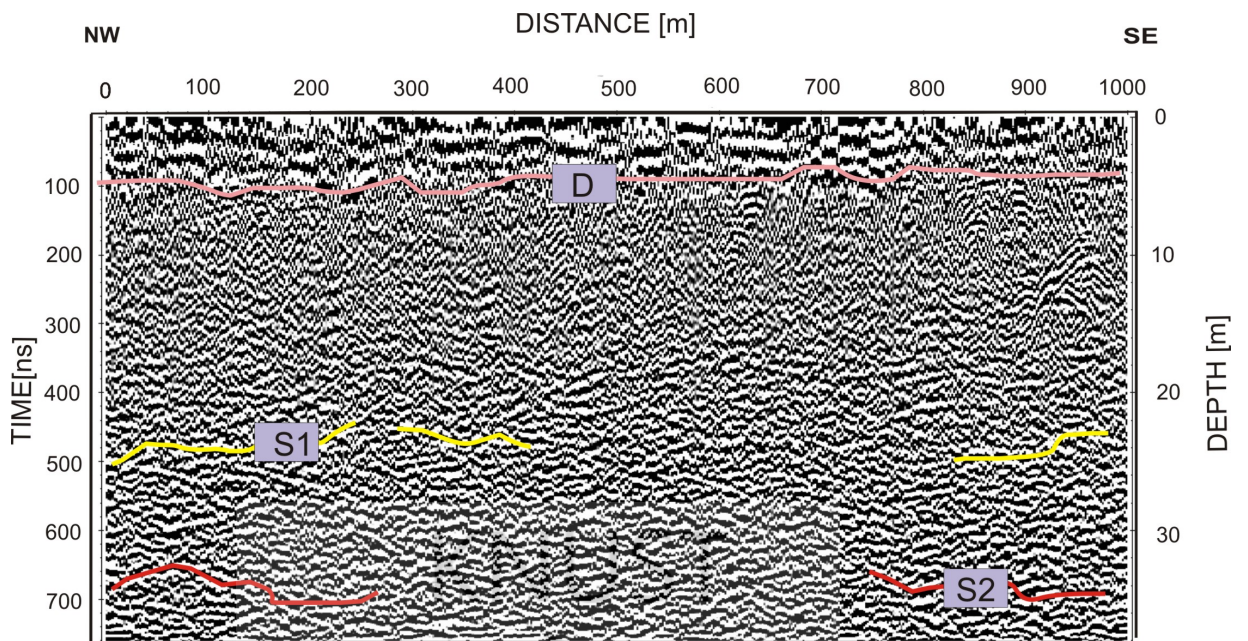


Figure 5.37: Radar Section of profile 2100E/3000N

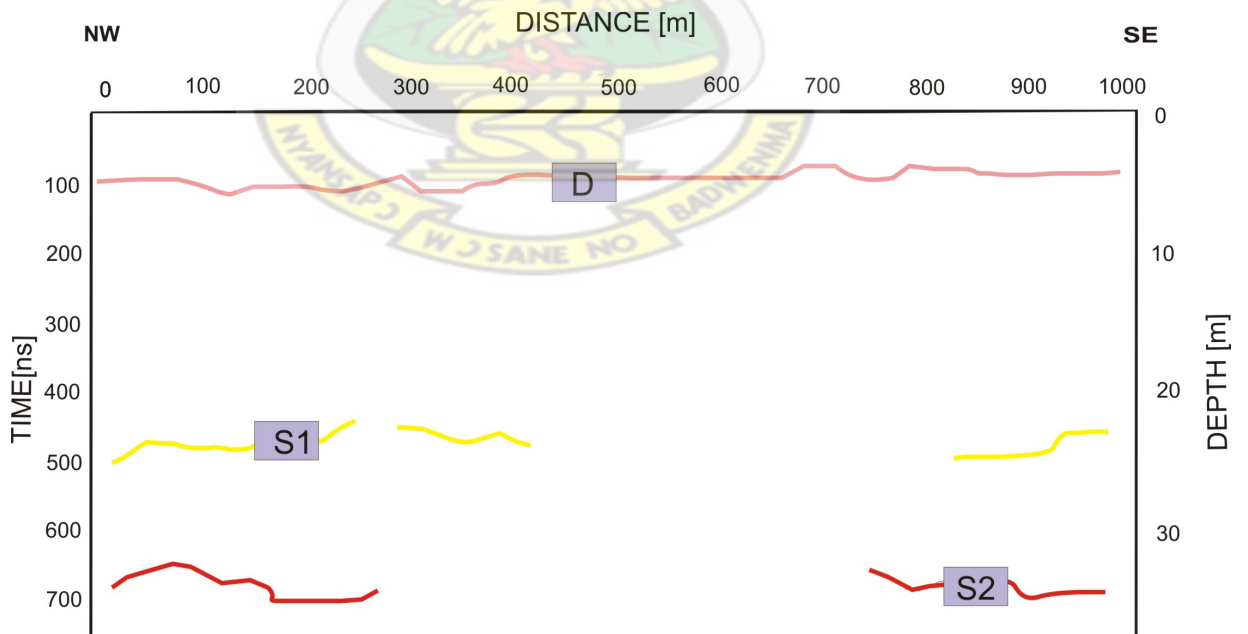


Figure 5.38: Inferred structures with potential of hosting gold mineralization of profile 2100E/3000N

5.1.2.3 Traverse 2: Line 2100E/3000N

The results of line 2050E/2000N are represented in Figure 5.37 and Figure 5.38. The duracrust-saprolite transition is marked D. The S1 structures occur between the depths of about 20 m and 25 m. On the other hand, S2 structures are also delineated between the depth range of 32 m and 36 m. The entire radargram has a lot of structures which are inferred to be hosting gold mineralization.

The rest of the interpretation for the 50 MHz antenna can be found in Appendix A



5.1.3 Interpretation of Inferred S2 Structures Hosting Gold Mineralization for 25 MHz RTA

In this section, the results of a contour plot of all S2 inferred structures possibly hosting gold mineralization are discussed. The results of the structural patterns for the inferred structures will be compared to the chargeability and resistivity results already acquired by the Newmont Ghana gold limited. This will help in understanding the trend of possible mineralization and its associated structures.

In the second look, the grid of inferred S1 structures for the 25 MHz RTA and the grid of inferred S1 and S2 structures for the 50 MHz RTA will be discussed in Appendix (A) section (A.2). In Appendix (A) section (A.3), the plots of The various sections drawn AB, CD, EF and GH showing the general trend of structures mapped will also be presented.

5.1.3.1 Interpretation of Inferred S2 Structural Depth Run for 25 MHz RTA

Figure 5.39 shows the structures between the depth range of 37.0 m and 44.5 m. In general the inferred structures depict possible structural deformation in the NW - SE direction. There is a clear evidence of a dipping structure Z1 falling between the profile spacing of about 200 m and 600 m stretching at a total distance of about 500 m. The depth range at which this dipping structure Z1 occurs is between 38.5 m and 44.5 m. This structural trend could be a potential zone for gold mineralization.

On the other hand, there is also a structural pattern Z2 showing a near horizontal feature between the profile intervals of 600 m and 800 m. The depth range at which this Z2 dipping structure occurs is between 42.0 m and 44.5 m which has a length of about 300 m.

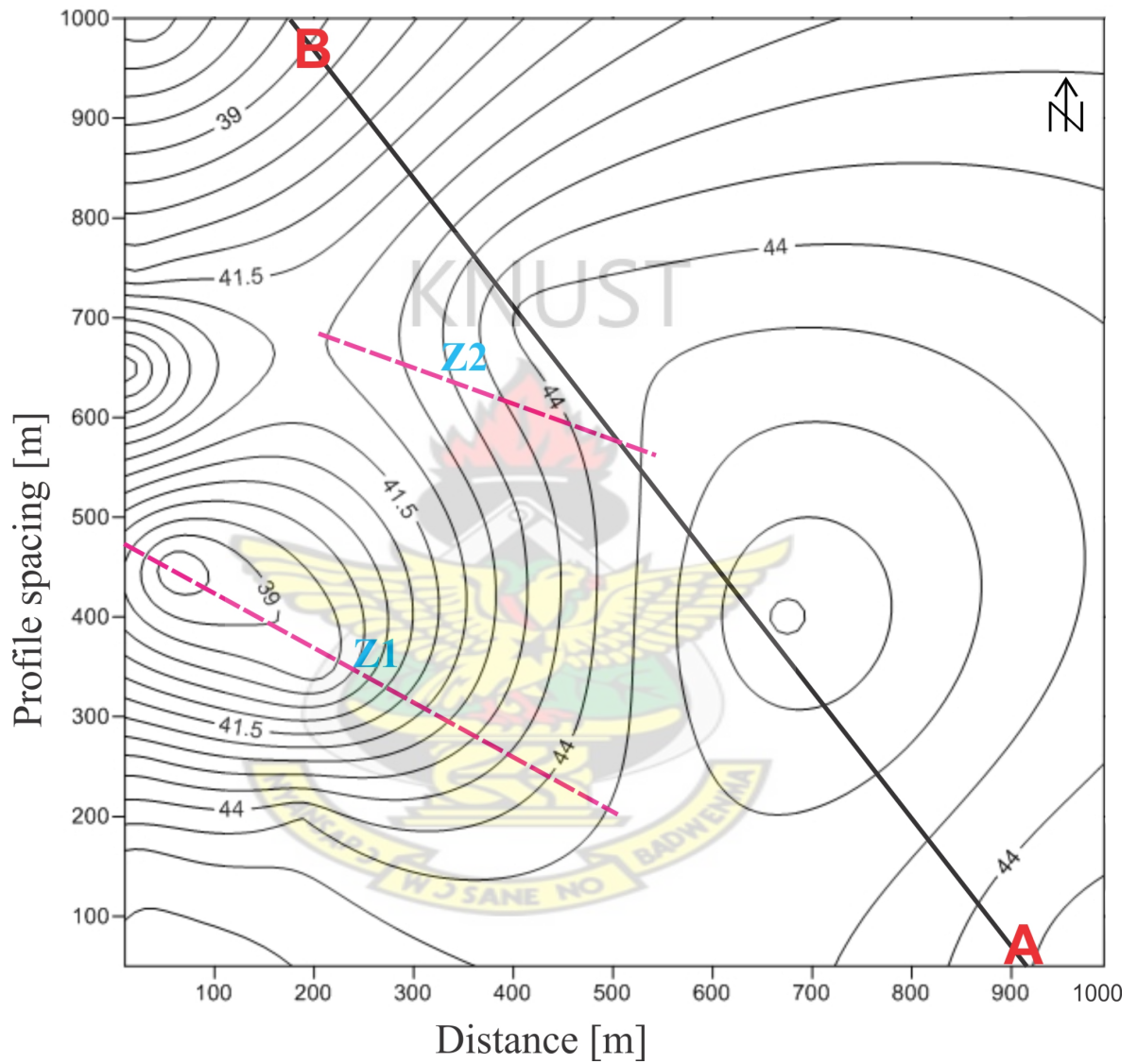


Figure 5.39: A contour grid of inferred S2 structures for 25 MHz RTA

5.1.4 Correlating GPR Results with Chargeability and Resistivity Results

Figure 5.4 and Figure 5.41 presents the results of the chargeability and resistivity data set respectively of the area under study. The chargeability and resistivity data were collected in a gradient array configuration at a maximum exploration depth of 12.5 m. The chargeability and resistivity results do not give the exact depths at which mineralization occur. The GPR results however have shown the possible structures hosting mineralization and the depths at which these structures hosting gold mineralization occur.

In Figure 5.4 the chargeability results show a clear evidence of high chargeability values between 14 mV/V and 17 mV/V which is indicated in the red color code. This anomalous zone is seen to be dipping in the North West South East direction. This is strongly in conformity with the structural trend mapped with the GPR as discussed in section 5.1.3. This NW - SE trend of mineralization falls within the profile spacing of 200 m and 700 m which stretches at about a total distance of 700 m.

The high chargeable zones indicate the weaker zones (conductive zones) within the saprolite which could be due to fractures, shear zones, cracks etc. These conductive zones are potential zones of gold mineralization.

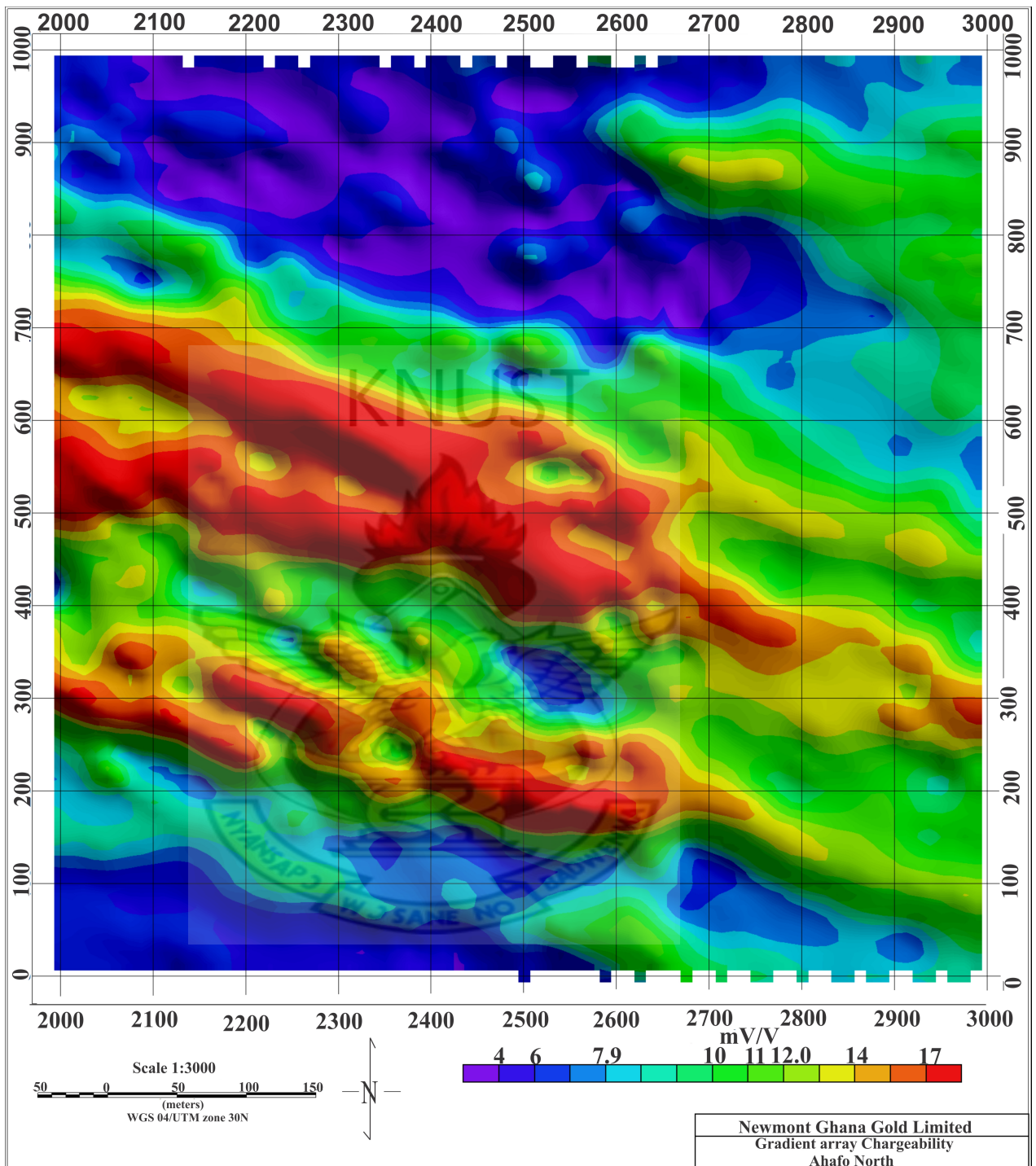


Figure 5.40: Local grid of Subenso-north chargeability results (Source: Geophysics section Newmont Ghana Gold Ltd, 2011)

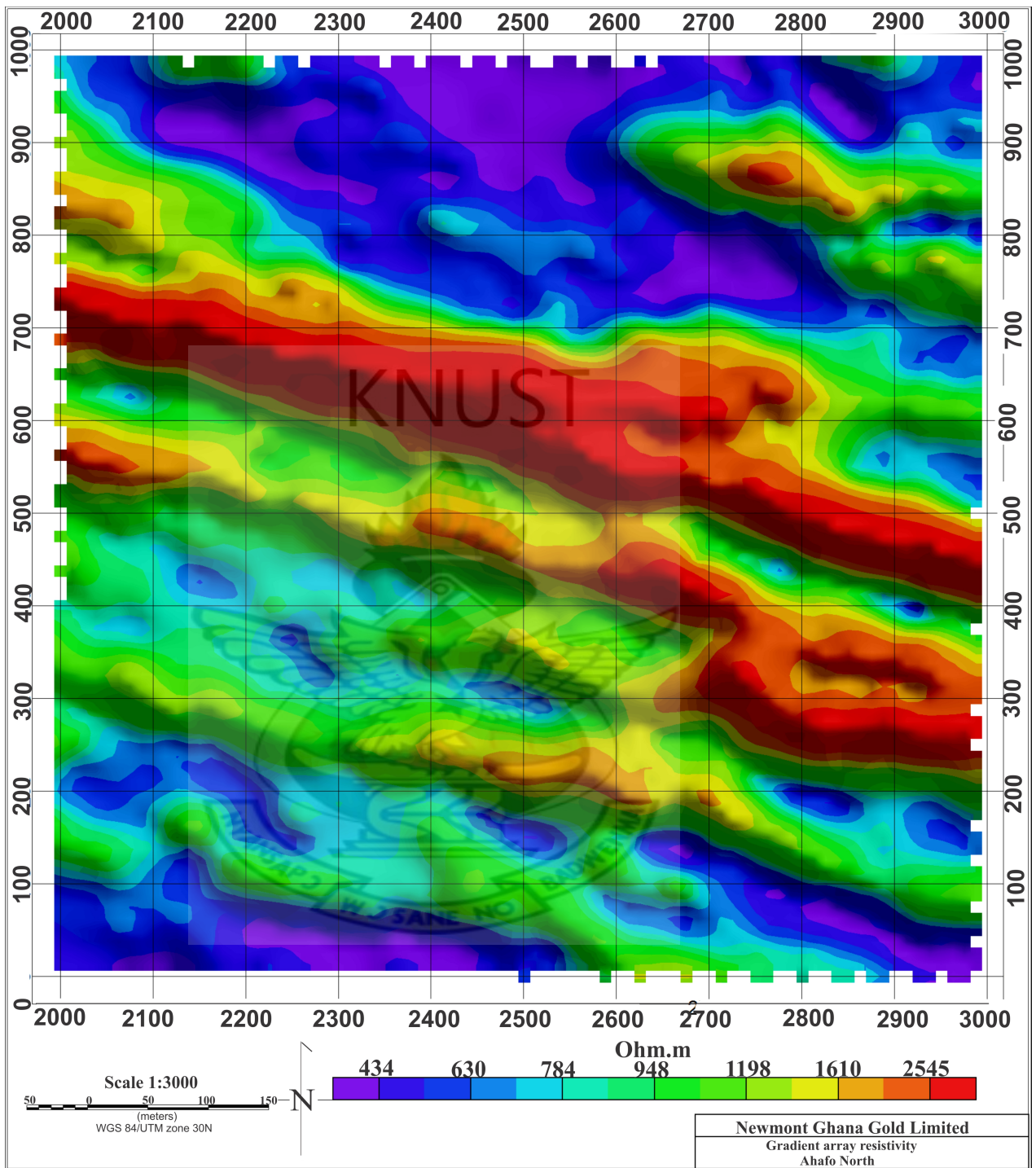


Figure 5.41: Local grid of Subenso-north resistivity results (Source: Geophysics section Newmont Ghana Gold Ltd, 2011)

Furthermore, the resistivity results shown in Figure 5.41 show a clear evidence of high resistivity value of 2545 Ohm m which is indicated in red color code. The high resistivity anomaly seen in red dips in the NW - SE direction. The anomalous zone is a clear indication of the presence of sulfide minerals which come in association with the gold mineralization. The likely sulfide minerals that could give rise to the high resistivity values are pyrite and arsenopyrite. These minerals have high resistivity values in nature and their presence has caused the resistivity anomaly which is in conformity with the structural trend presented by the GPR results in section 5.1.3 and that of the chargeability results.



CHAPTER 6

CONCLUSION AND RECOMMENDATIONS

6.1 Conclusion

In the quest of mapping zones of gold mineralization at the Subenso north concession of Newmont Ghana Gold Limited. The ground based ground penetrating radar (GPR) survey was conducted over an already known gold deposit mapped by the Newmont company with results from both chargeability and resistivity data sets. This study has shown a strong correlation in gold mineralization trend with the resistivity and chargeability results presented by the Newmont Ghana gold limited. Throughout the survey, less cost was incurred as compared with the resistivity and chargeability survey carried out by the Newmont Ghana gold limited. The structures in the highly weathered saprolite has been delineated by the application of this ground penetrating radar method.

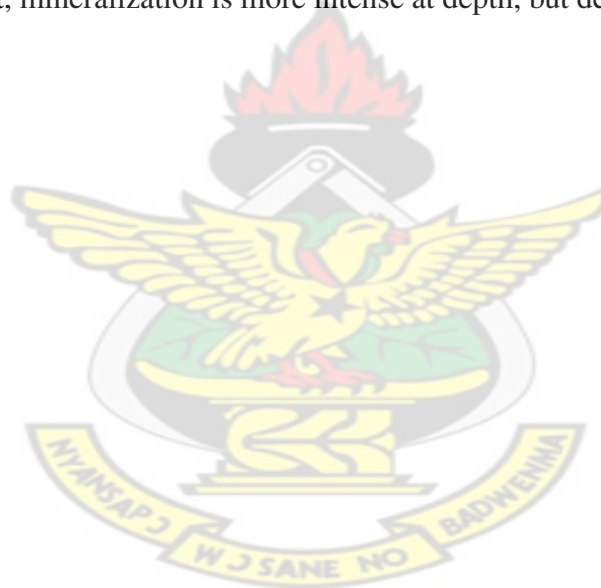
The exploration depth was found to be approximately 925 ns corresponding to 50 m with an average soil velocity of 0.1 m/ns. The saprolite which overlain the primary lithologic unit as well as the duracrust which also overlain locally the saprolite were successfully delineated.

Two sets of inferred structural patterns were established. The structural patterns were S1 and S2 . The S1 inferred structures were found between the depth range of (12 m and 42 m) and the S2 also between (31 m and 48 m) for 25 MHz RTA. 50 MHz RTA also recorded S1

structures at the depth range of (14 m and 34 m) and that of the S2 at the depth range of (27 m and 38 m).

Furthermore, the heterogeneous radar signatures recorded suggests that, deformation effects are more intense between the depth range of (32 m and 39 m) and (43 m and 47 m) for 25 MHz RTA S1 and S2 structures respectively.

50 MHz RTA radar sections also provided relevant structures between the depth ranges of (28 m and 31 m) and (35 m and 38 m) for S1 and S2 inferred structures respectively. These sets of structures are inferred structures possibly hosting gold mineralization. The work has also revealed that, mineralization is more intense at depth, but decreases as it outcrops to the surface.



6.2 Recommendations and Outlook

The results of the present study lead to the following recommendations

- It is strongly recommended that, exploration companies should carry out GPR survey to help them image the various structural patterns controlling gold mineralization. This is for the fact that, GPR survey provides the best subsurface resolution among the other electromagnetic methods along side its cost effectiveness.
- The GPR survey should be carried out in a distance measuring mode. This will help define the exact location and provide the necessary coordinates for the anomalous body.
- It is recommended that, a 2 MHz rough terrain antenna should be used to survey the area up to a maximum depth of about 600 m. This will help characterize the various lithology associated with gold mineralization at the study area.
- Disturbances from trees gave a lot of diffractions in the radar data. This was solved by filtering the data set with diffraction stack and dewow filters.
- Collecting data on muddy areas proved very difficult. This is as a results of high attenuation of the radar signal. This difficulty was minimized by choosing appropriate time window and samplings frequency.

References

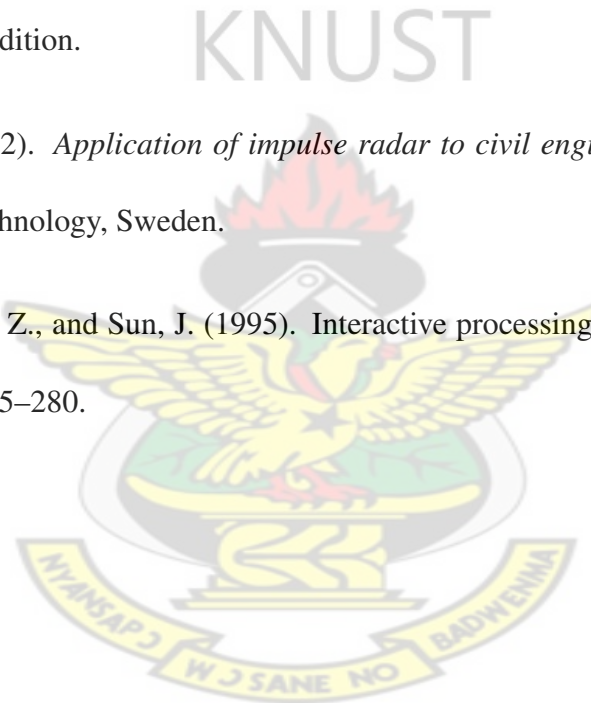
1. Akabzaa, T. and Darimani, A. (2001). Impact of mining sector investment in Ghana: A study of the Tarkwa mining region. *A draft report*, pages 2–4.
2. Balanis, C. (1989). *Advanced engineering electromagnetic*. page 981.
3. Bishop, J., Cumming, A., Ferrari, R., and Miller, K. (1980). Results on impulse radar ice-depth, Iceland. *Conference on International Karakoram Project*, 1:126–134.
4. Cagnoli, B. and Russel, J. (2000). Imaging the subsurface stratigraphy in the Ubehebe hydrovolcanic field (death valley California) using ground penetrating radar. *Journal of Volcanology and Geothermal Research*, 96:45–56.
5. Carlos da Silva, C., Walter de Medeiros, E., Emanuel de Sa, F., and Pedro Xavier, N. (2004). Resistivity and ground-penetrating radar images of fractures in a crystalline aquifer: a case study in Caicara farm-ne Brazil. *Journal of Applied Geophysics*, 56:295–307.
6. Cees, S. (2006). South West Interpretation Geology of Ghana. *consulting structural Geologist, Greenfields Exploration*.
7. Conyers, L. and Goodman, D. (1998). *Ground Penetrating Radar, An Introduction for Archaeologists*. AltaMira Press, Walnut Creek, Calofornia.

8. Daniels, D. (1996). Surface penetrating radar. Technical report, The Institute of Electrical Engineers, London UK.
9. Davis, J., Killey, R., Annan, A., and Vaughan, C. (1984). Surface and borehole ground penetration radar surveys for mapping geological structure. *A-Cubed Inc, Tech. paper presented at NWWA/US EPA Conf on surface and Borehole Geophysical Methods, San Antonio, Texas*, (4).
10. Dougherty, M., Michaels, P., Pelton, J., and Liberty, L. (1994). Enhancement of ground penetrating radar data through signal processing. *Symposium on the Application of Geophysics to Engineering and Environmental Problem (SAGEEP)*, 94:1021–1028.
11. Dzigbodi-Adjima, K. (1992). Geology and geochemical patterns of the Birimian gold deposits. *Journal of Geochemical Exploration*, 47(305-320):306–313.
12. Fisher, C., Stewart, R., and Jol, H. (1994). Processing ground penetrating radar. *The 5th International Conference on Ground Penetrating Radar (GPR), Canada*, 94:661–675.
13. Grasmueck, M. (1996). 3-D ground penetrating radar applied to fracture imaging in gneiss. *Journal of geophysics*, 61:1050–1064.
14. Harry, M. J. (2009). *Ground Penetrating Radar Theory and Application*. Elsevier Science, first edition.
15. Hirdes, W. and Leube, R. (1989). Gold mineralization of the Birimian supergroup in Ghana/West Africa. *Ghanaian-German Mineral prospecting project*.
16. Holloway, A. (1992). Fracture mapping in granite rock using ground radar in Pilon. *Geological Survey of Canada*, (90-4):85–100.
17. Junner, N. (1935). Gold in the gold coast. *Gold Coast Geological survey. Mem*, 4:67.

18. Kesse, G. (1985). *The Mineral and Rock Resources of Ghana*. A.A.Balkema, Rotterdam.
19. Knight, R. (2001). Ground penetrating radar for environmental applications. *Annual Rev. Earth planet Science*, 29:229–225.
20. Lees, B. (1998). The application of ground penetrating radar to mineral specimen mining. *Mineralogical Record*, 29:145–153.
21. Leggo, P. and Leech, C. (1983). Sub-surface investigation for shallow mine workings and cavities by the ground impulse radar technique. *Ground Engineering*, 16:20–23.
22. Leube, A. and Hirdes, W. (1986). The Birimian supergroup of Ghana-depositional environment, structural development and conceptual model of an early proterozoic suite.
23. Leube, A., Hirdes, W., and Kesse, G. (1990). The early Proterozoic Birimian supergroup of Ghana some aspects of its associated gold mineralization. pages 139–165.
24. Leucci, G. (2006). Contribution of ground penetrating radar and electrical resistivity tomography to identify the cavity and fractures under the main church in Botrugno (Lecce, Italy). *Journal of Archaeological Science*, 33:1194–1204.
25. Mala (2011). Mala geoscience, "RAMAC/GPR" software manual. pages 7–18.
26. Modroo, J. and Olhoeft, G. R. (2004). Ground penetrating radar location of Buried Avalnache Victims. *Proceedings of the 2004 International Snow Science Workshop, Jackson Hole, Wyoming*.
27. Newmont (2006). Ahafo gold mine environmental report to EPA. *Technical report, Newmont Ghana Gold Ltd*.
28. Newmont (2007). Ahafo gold mine environmental report to EPA. *Technical report, Newmont Ghana Gold Ltd*.

29. Newmont (2008a). Ahafo gold mine environmental report to EPA. Technical report, Newmont Ghana Gold Ltd.
30. Newmont (2008b). Ahafo mineral resource and ore reserve. Technical report, Newmont Ghana Gold Ltd.
31. Newmont (2009). Ahafo gold mine environmental report to EPA. Technical report, Newmont Ghana Gold Ltd.
32. Nobes, D. (1999). Geophysical surveys of burial sites: A case study of the oara urupa. *Geophysics*, 64(2):357–367.
33. Noon, D., Stickley, G., and Longstaff, D. (2000). Proceedings of the eighth international conference on ground penetrating radar, SPIE. 4084:908.
34. Olhoeft, G. (1998). Electrical, magnetic and geometric properties that determine ground penetrating radar performance. *International Conf. Ground Penetrating Radar*, 7:177–82.
35. Olsson, O., Falk, O., Forslund, O., Lundmark, L., and Sandberg, E. (1992). Borehole radar applied to the characterization of hydraulically conductive fracture zones in crystalline rock. *Geophysical prospecting*, 40:109–142.
36. Oluwatosin, C. (2010). Ground penetrating radar imaging of ancient clastic deposits: A three-dimensional outcrops studies. pages 17, 223–224.
37. Pilon, J. (1992). Ground penetrating radar. *Geological survey of Canada*, (90-4):241.
38. Powers, M. (1997). Modelling frequency-dependent GPR. *Leading Edge*, 16:1657–62.
39. Roland, H. (2004). Interpretation of regional structure and geology from aeromagnetic data,. *Newmont Ghana Gold Ltd*, pages 6.25–6.29.

40. Sandmeier, K. (2011). *The 2D processing and 2D/3D interpretation software for GPR, reflection seismics and refraction seismics.*
41. Skolnik, M. (1970). *Radar Handbook.* McGraw Hill Book Company, New York.
42. Slater, L. and Tina Niemi, N. (2003). Ground penetrating radar investigation of active faults along the dead sea transform and implications for seismic hazards within the city of Aqaba, Jordan. *Journal of Tectonophysics*, 368:33–50.
43. Telford, W., Geldart, L., and Sheriff, R. (1990). *Applied Geophysics.* Cambridge university Press, second edition.
44. Ulriksen, C. (1982). *Application of impulse radar to civil engineering.* PhD thesis, Lund Institute of Technology, Sweden.
45. Young, R., Deng, Z., and Sun, J. (1995). Interactive processing of GPR data. *The Leading Edge*, pages 275–280.



Appendix A

A.1 Ground Penetrating Radar Profile Images For 50 MHz

RTA

KNUST



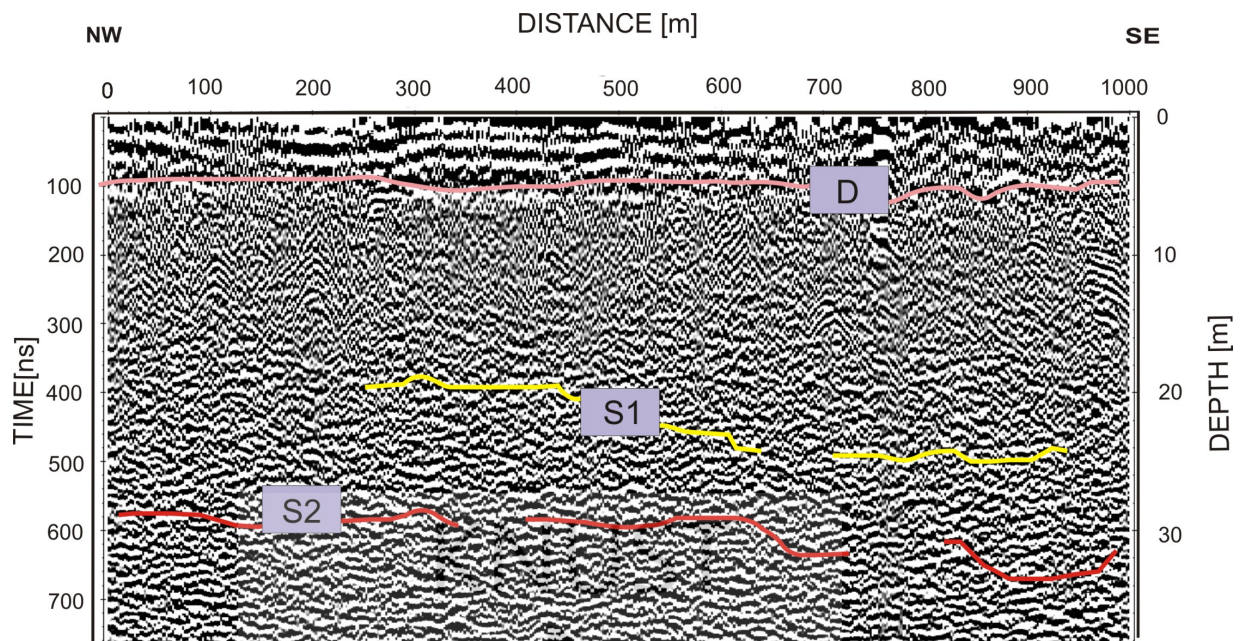


Figure A.1: Radar section of profile 2150E/2000N

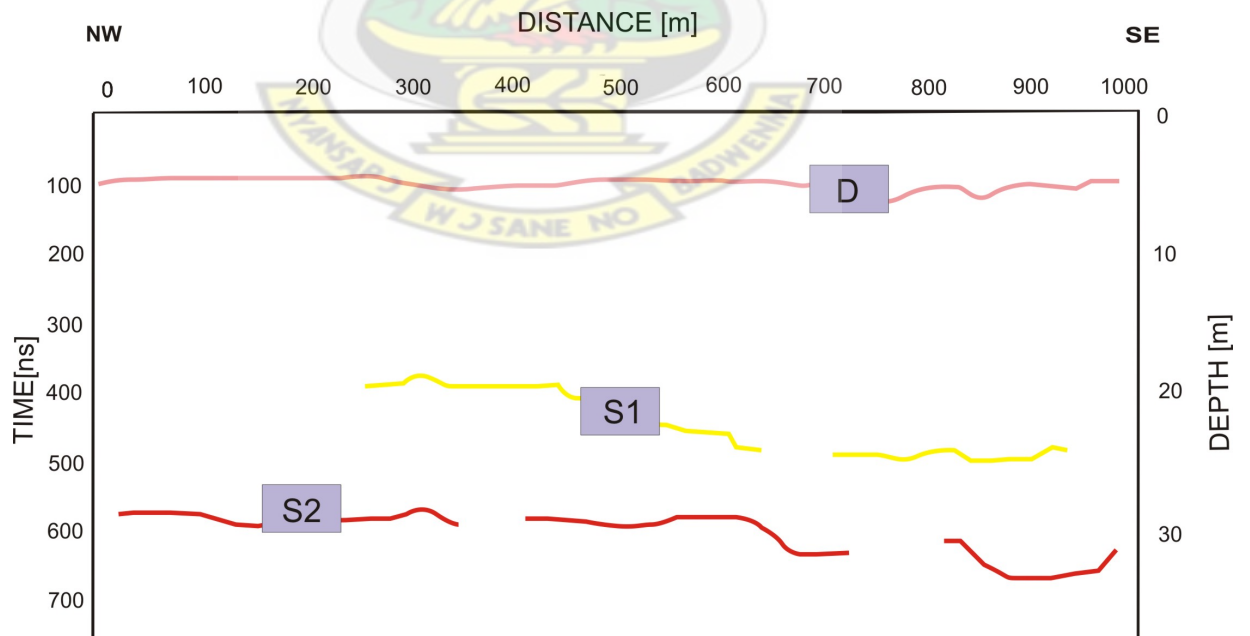


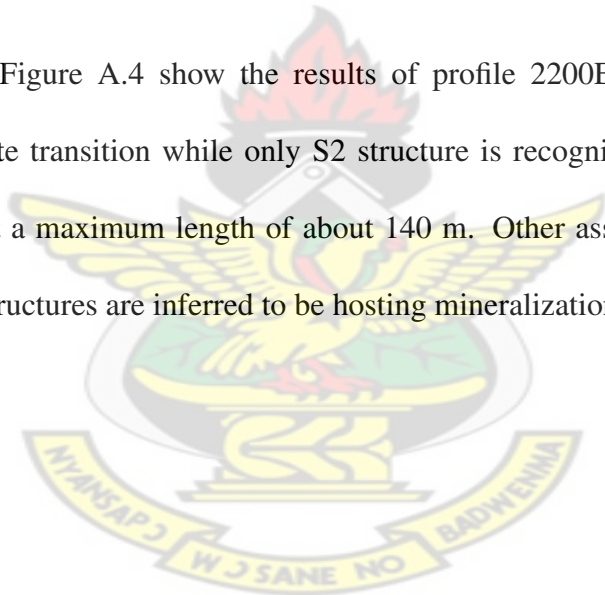
Figure A.2: Inferred structures hosting mineralization of profile 2150E/2000N

A.1.1 Traverse 3: Line 2150E/2000N

The results of profile 2150E/2000N are represented in Figure A.1 and Figure A.2. The structure marked D with the pink layer indicates the duracrust and saprolite contact. S1 structure is located between the depth range of 20 m and 25 m with a maximum extension of about 310 m. Structure S2 also extends at a maximum length of 320 m at depths between 30 m and 32 m. S1 and S2 structures are inferred structures hosting mineralization.

A.1.2 Traverse 4: Line 2200E/3000N

Figure A.3 and Figure A.4 show the results of profile 2200E/3000N. D represents the duracrust-saprolite transition while only S2 structure is recognized. The extension of the S2 structure is at a maximum length of about 140 m. Other associated structures are also present. These structures are inferred to be hosting mineralization



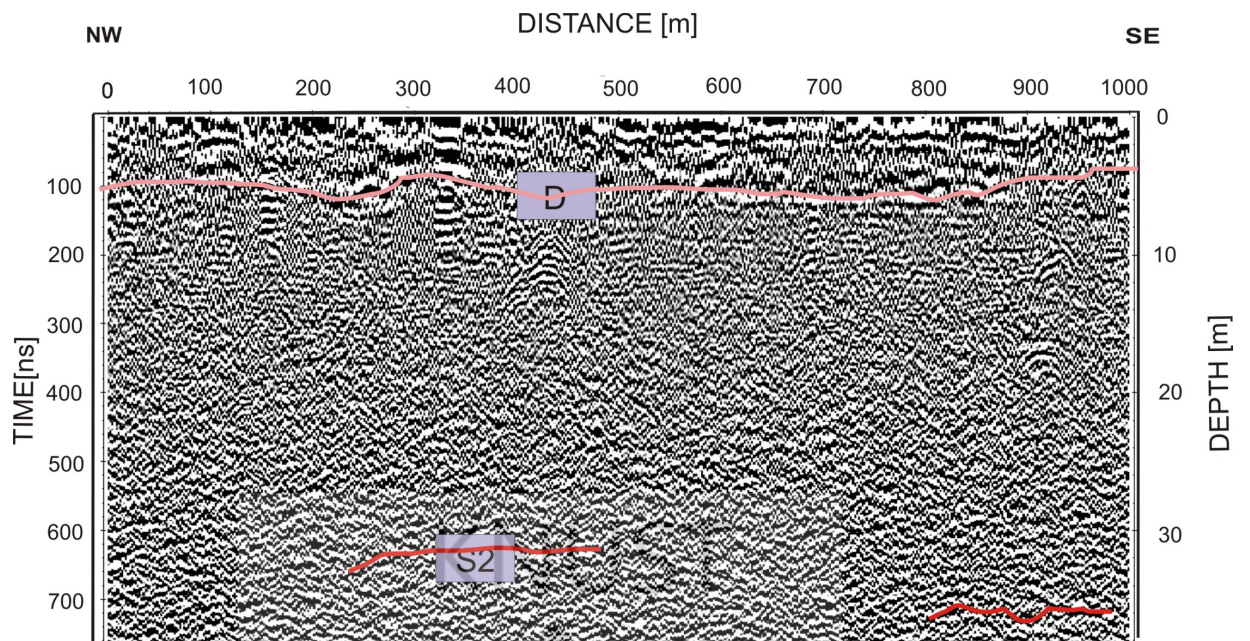


Figure A.3: Radar section of profile 2200E/3000N

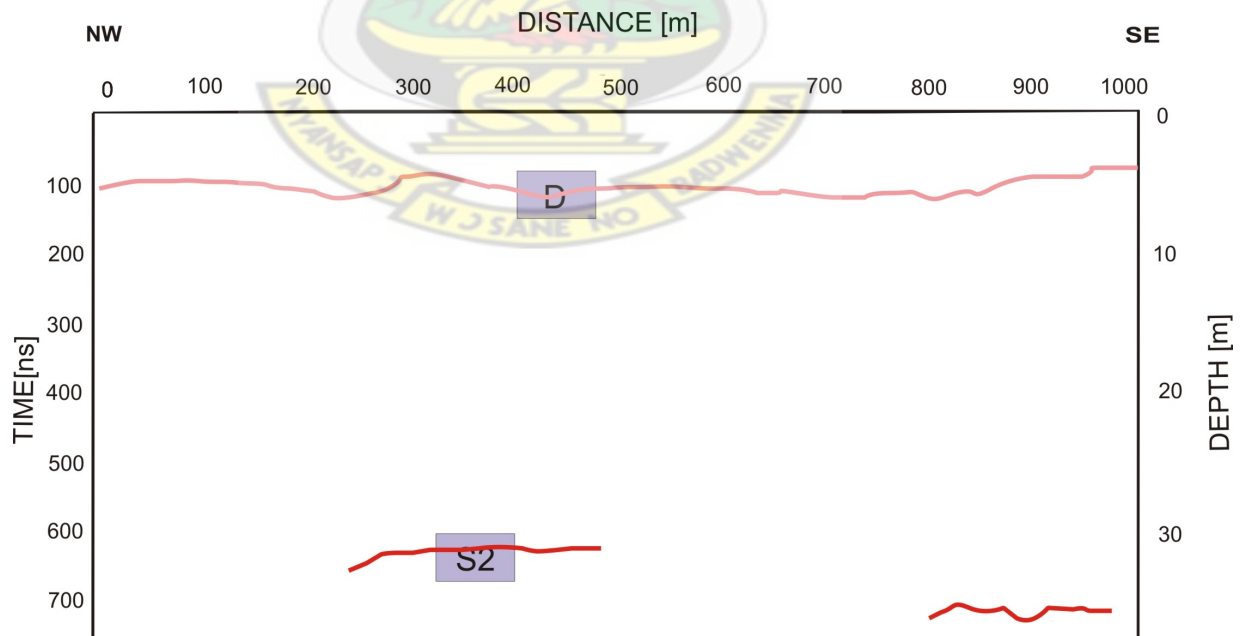


Figure A.4: Inferred structures hosting mineralization of profile 2200E/3000N

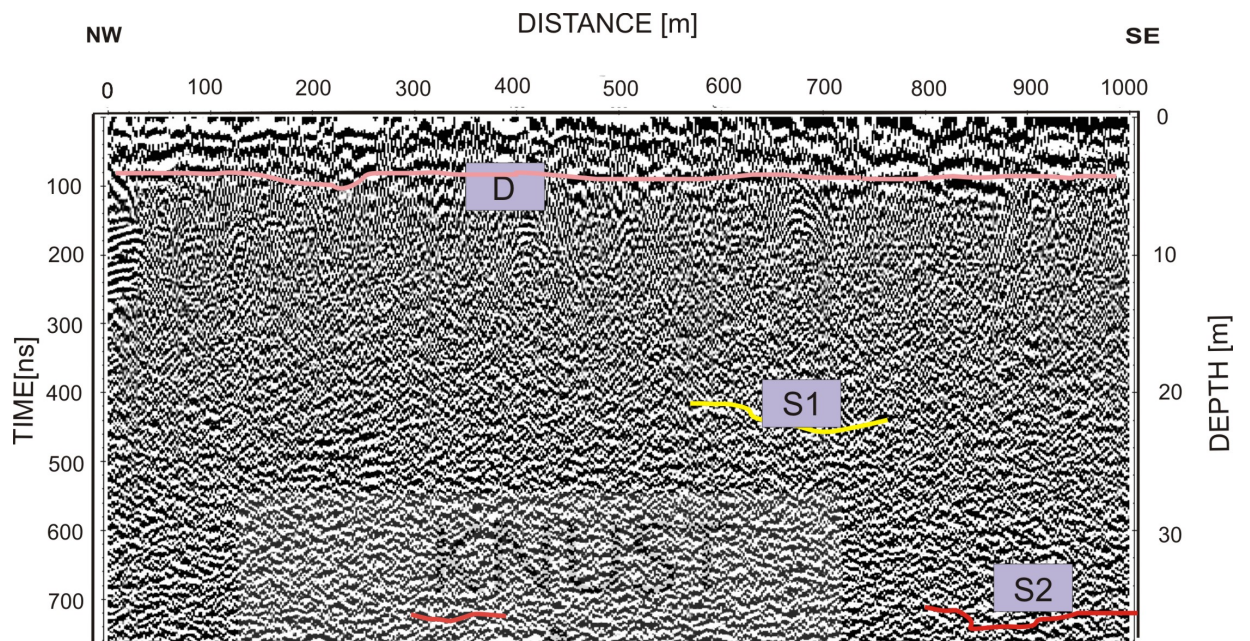


Figure A.5: Radar section of profile 2250E/2000N

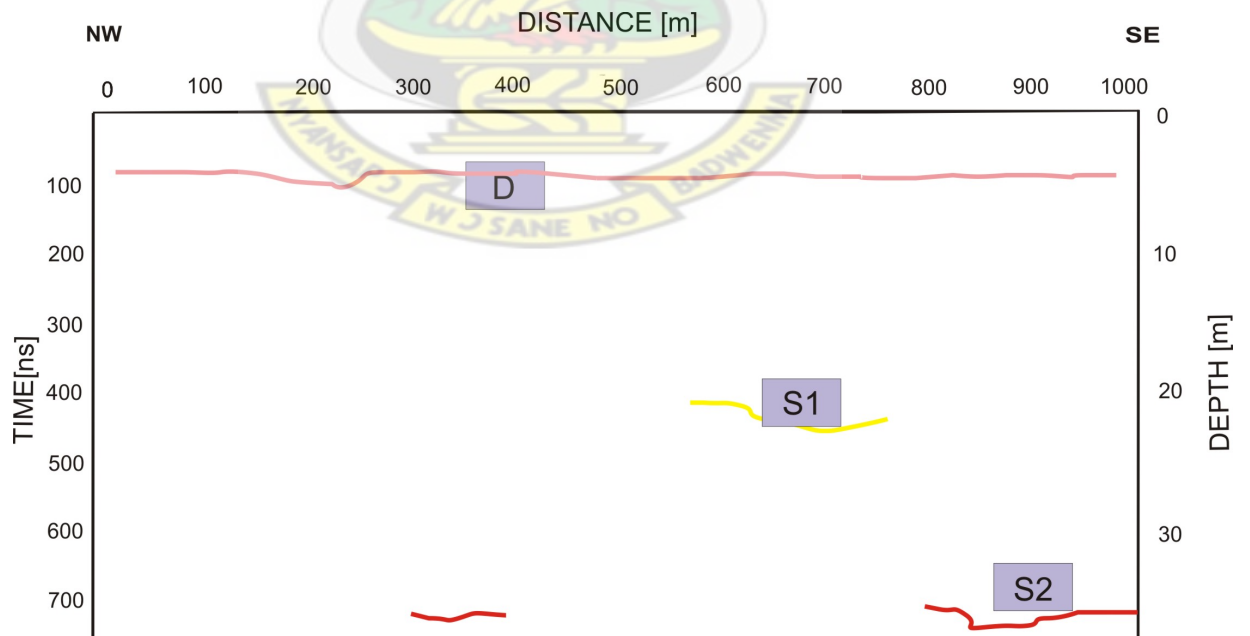


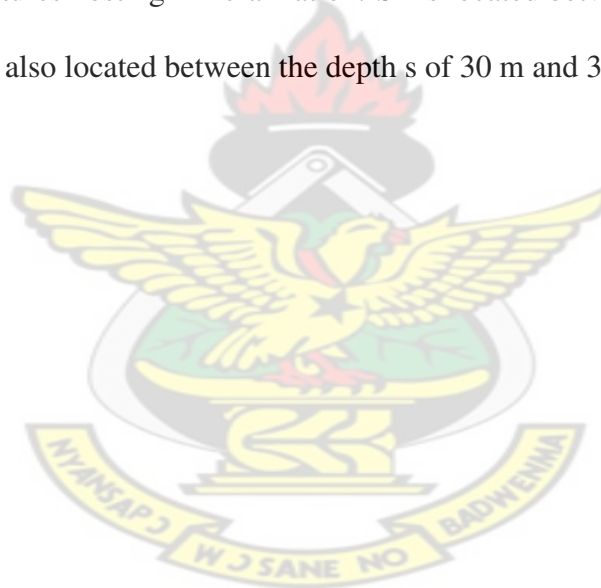
Figure A.6: Inferred structures hosting mineralization of profile 2250E/2000N

A.1.3 Traverse 5: Line 2250E/2000N

Figure A.5 and Figure A.6 illustrate the results of profile 2250E/2000N. The duracrust and saprolite contact is designated by the structure D on the oink layer. S1 and S2 are inferred structures possibly hosting mineralization.

A.1.4 Traverse 6: Line 2300E/3000N

The results of profile 2300E/3000N are represented in Figure A.7 and Figure A.8. S1 and S2 are inferred structures hosting mineralization. S1 is located between the depths of 19 m and 22 m while S2 is also located between the depths of 30 m and 36 m.



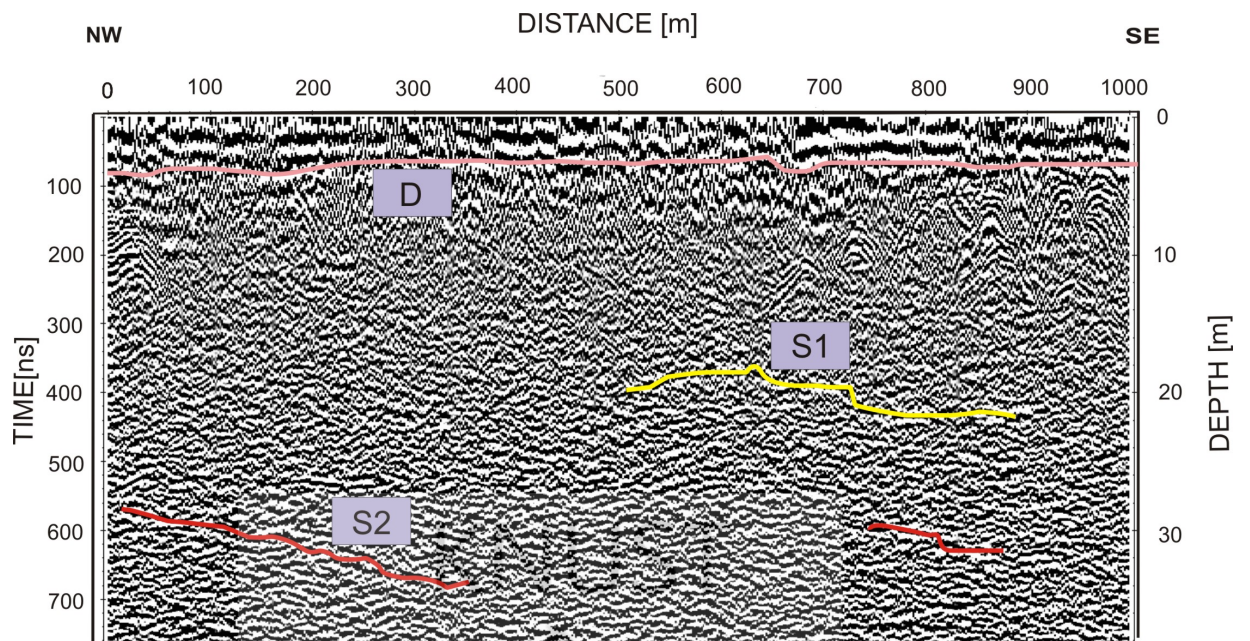


Figure A.7: Radar section of profile 2300E/3000N

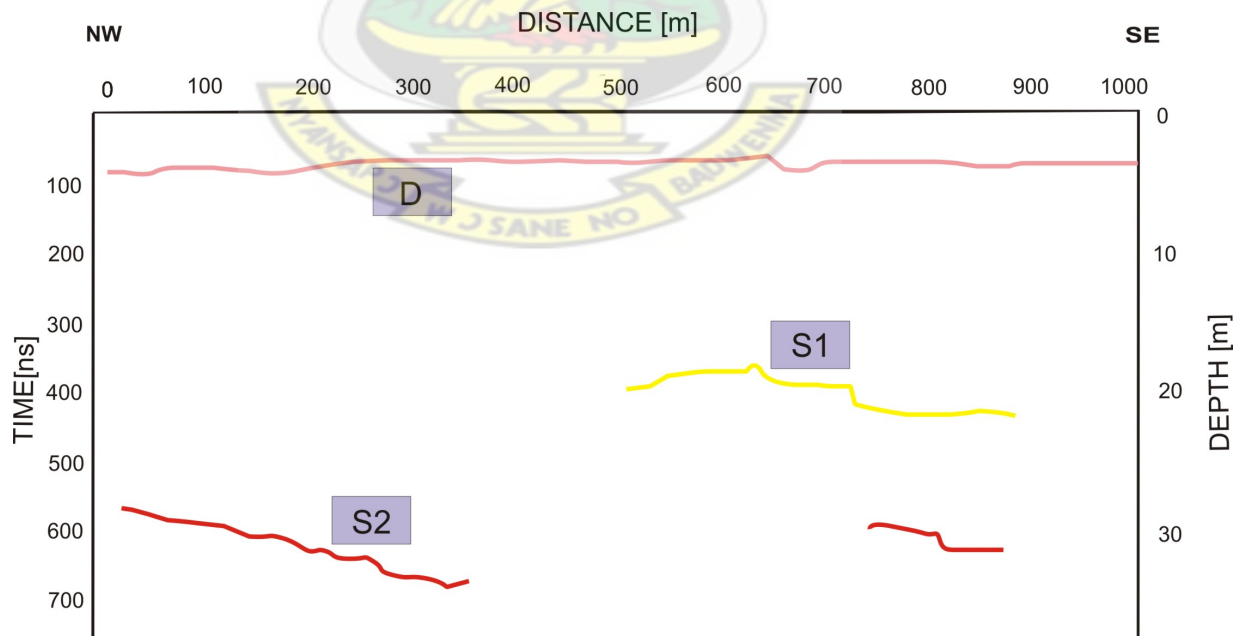


Figure A.8: Inferred structures hosting mineralization of profile 2300E/3000N

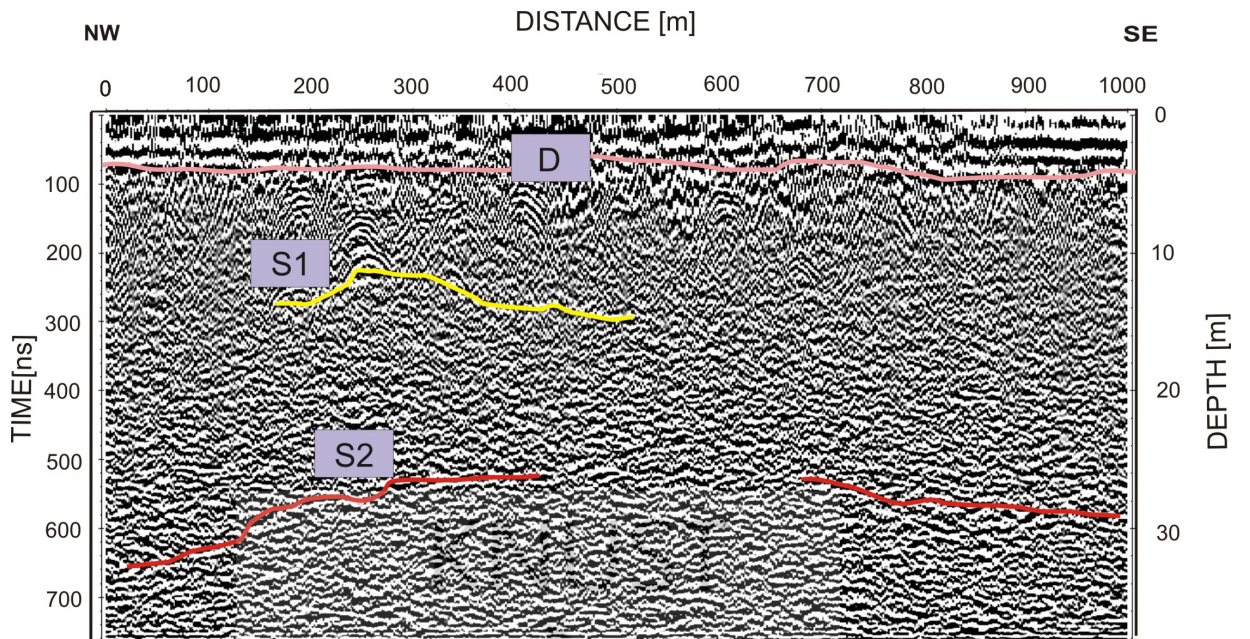


Figure A.9: Radar section of profile 2350E/2000N

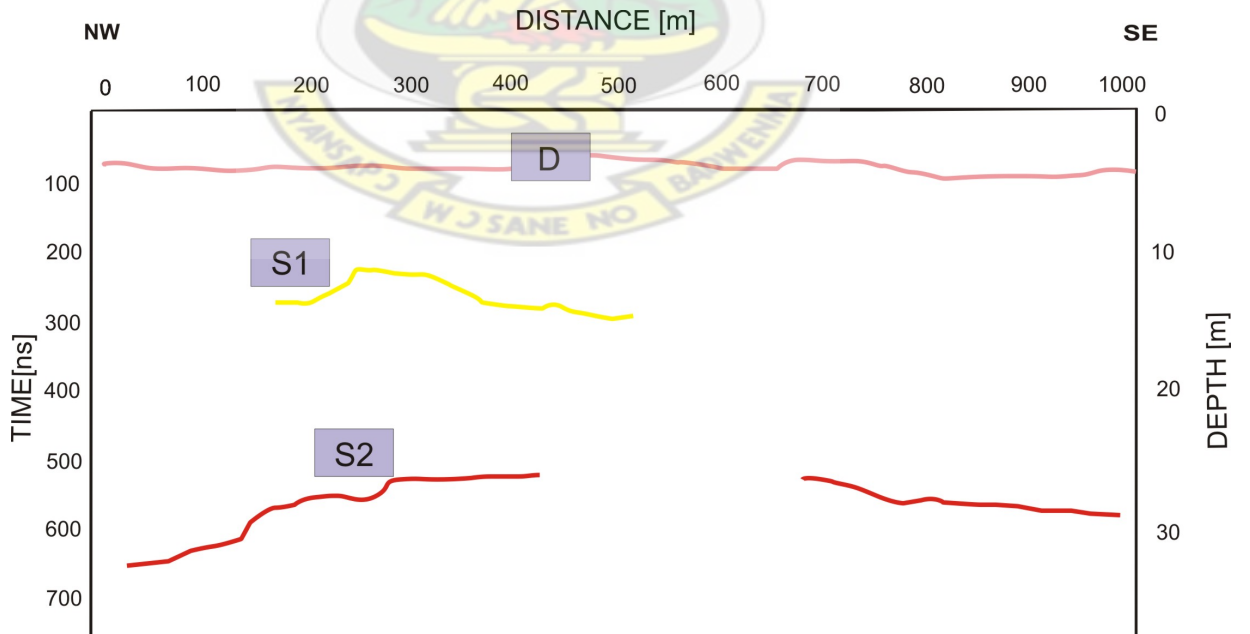


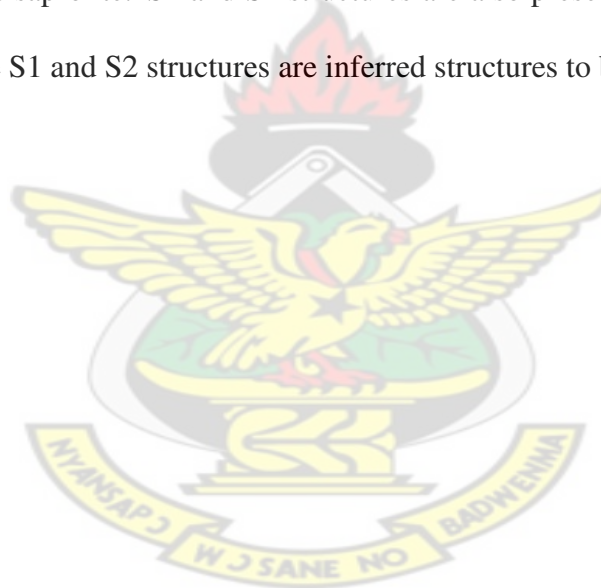
Figure A.10: Inferred structures hosting mineralization of profile 2350E/2000N

A.1.5 Traverse 7: Line 2350E/2000N

Figure A.9 and Figure A.10 show the results of profile 2350/2000N. The inferred structures hosting mineralization are marked S1 and S2 with the duracrust-saprolite contact marked D.

A.1.6 Traverse 9: Line 2450E/2000N

The results of line 2450E/3000N are represented in Figure A.11 and A.12. D is a structure located at a depth range of 4 m and 6 m. This structure marked D is the contact between the duracrust and saprolite. S1 and S2 structures are also present at depths 23 m and 38 m respectively. The S1 and S2 structures are inferred structures to be hosting mineralization.



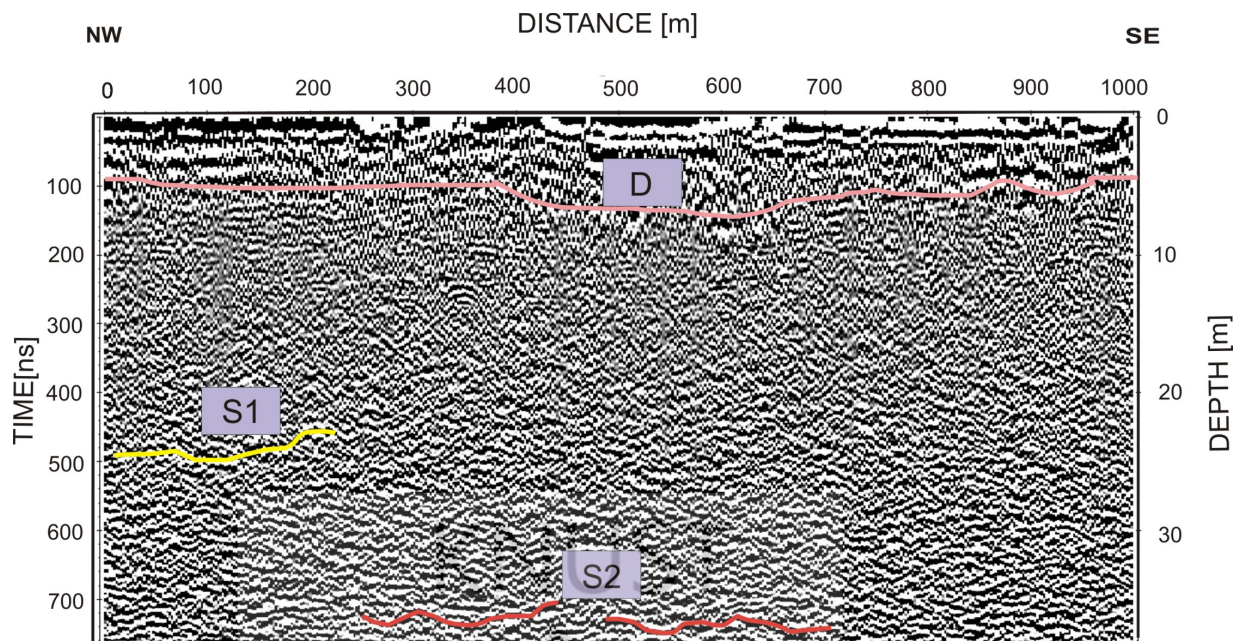


Figure A.11: Radar section of profile 2450E/2000N

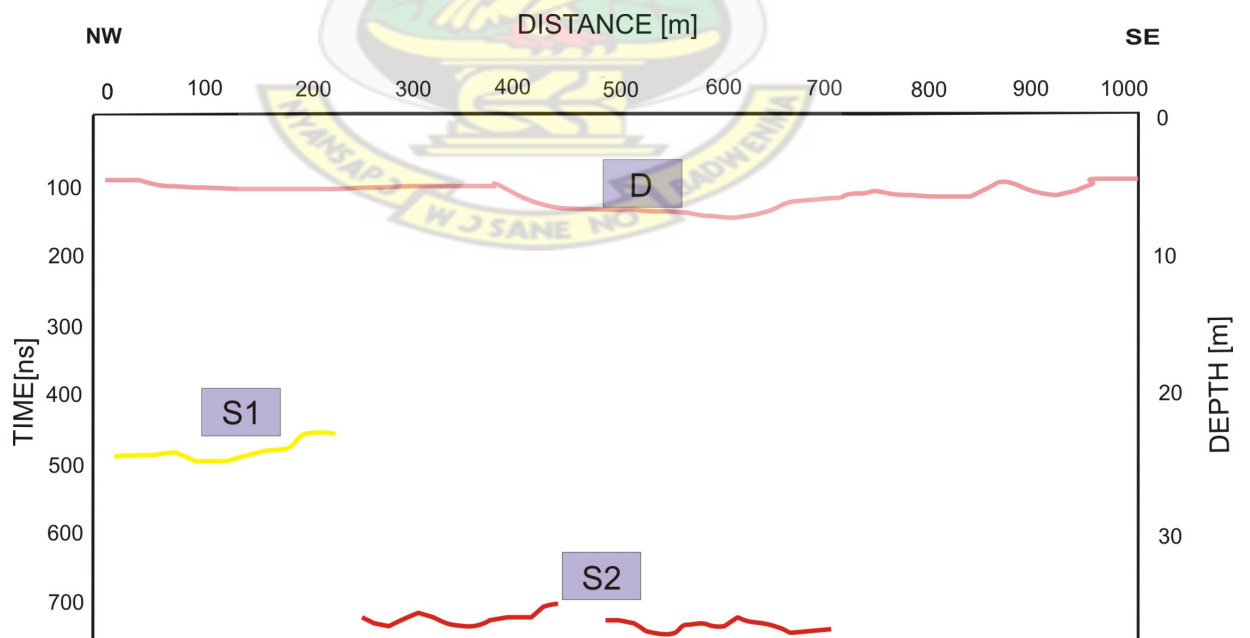


Figure A.12: Inferred structures hosting mineralization of profile 2450E/2000N

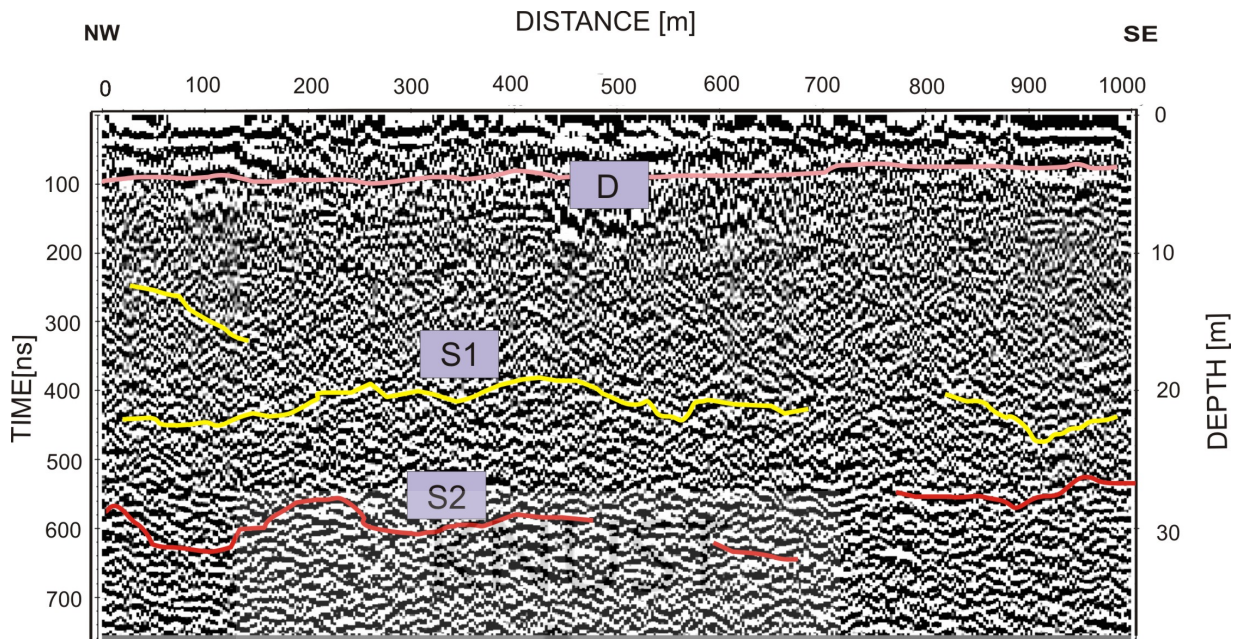


Figure A.13: Radar section of profile 2500E/3000N

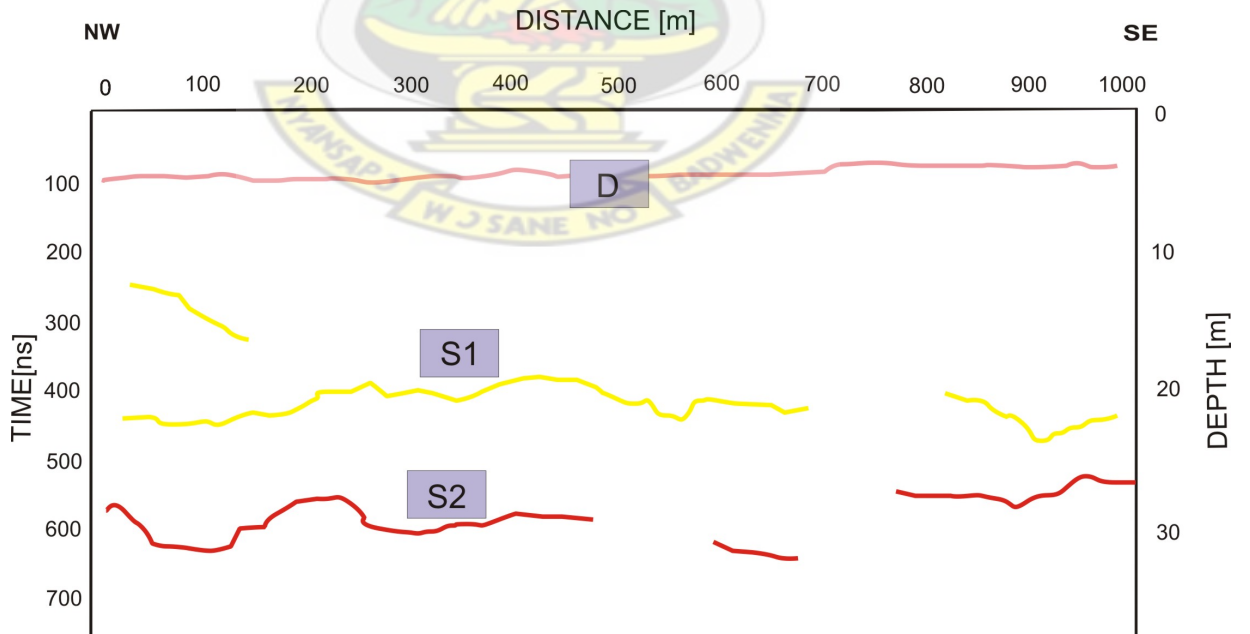


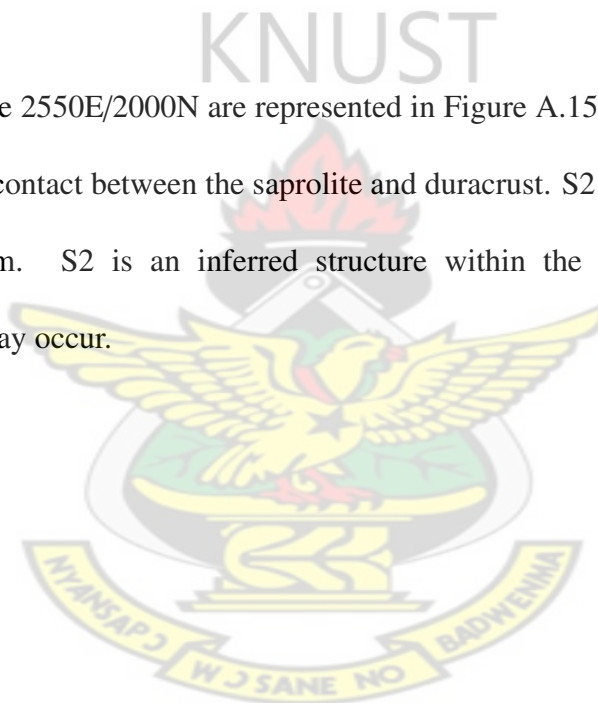
Figure A.14: Inferred structures hosting mineralization of profile 2500E/3000N

A.1.7 Traverse 10: Line 2500E/3000N

Figure A.13 and A.14 show the results of line 2500E/3000N. The S1 structure is slightly undulating in geometry and extends from 15 m to 670 m distance interval. The S2 structure Also show discontinuities and undulating feature between the depths 26 m and 33 m.. The S1 and S2 structures are inferred structures which might be hosting gold mineralization.

A.1.8 Traverse 11: Line 2550E/2000N

The results of line 2550E/2000N are represented in Figure A.15 and Figure A.16. Structure marked D is the contact between the saprolite and duracrust. S2 structure is also recognized in this radargram. S2 is an inferred structure within the subsurface where possible mineralization may occur.



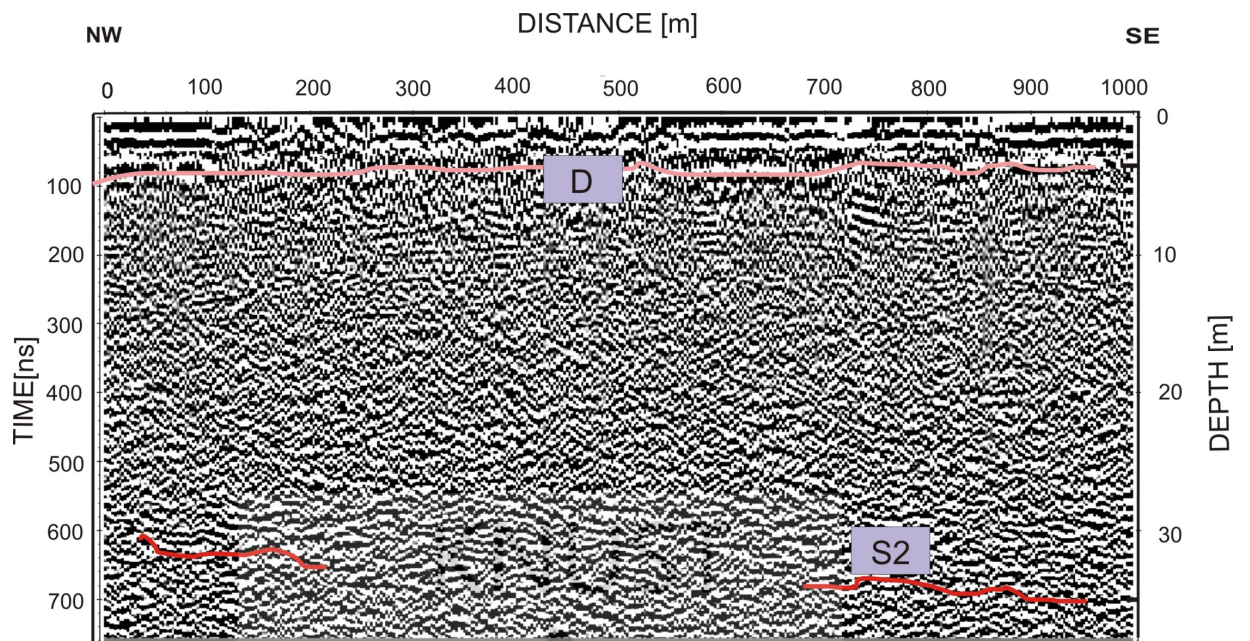


Figure A.15: Radar section of profile 2550E/2000N

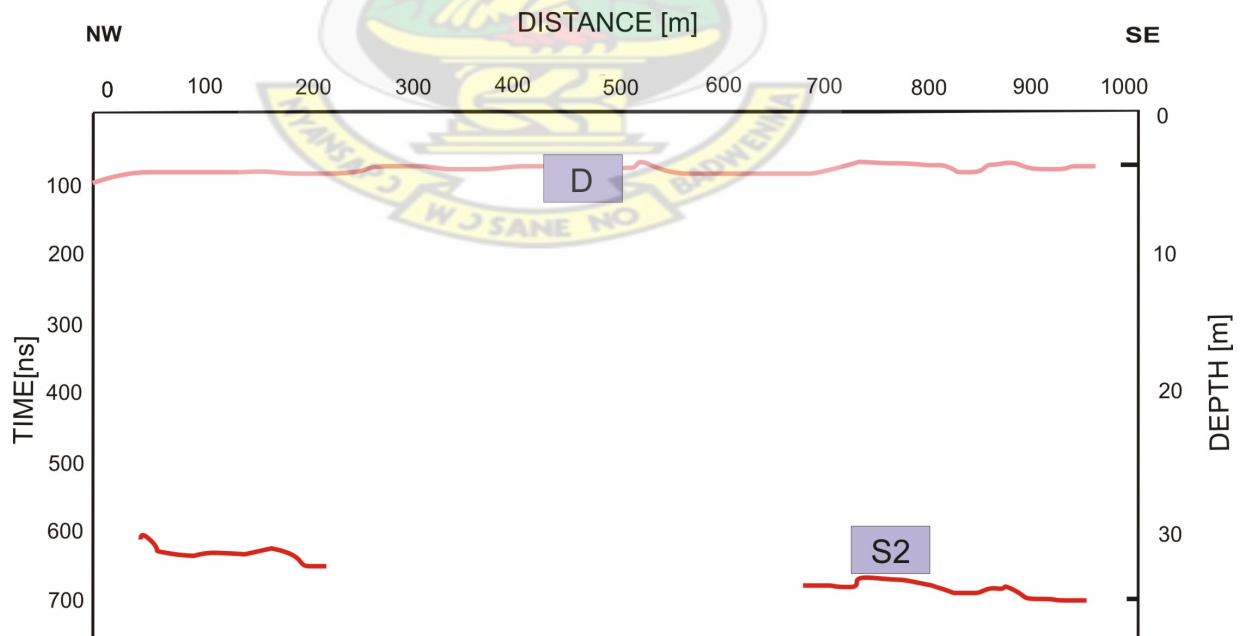


Figure A.16: Inferred structures hosting mineralization of profile 2550E/2000N

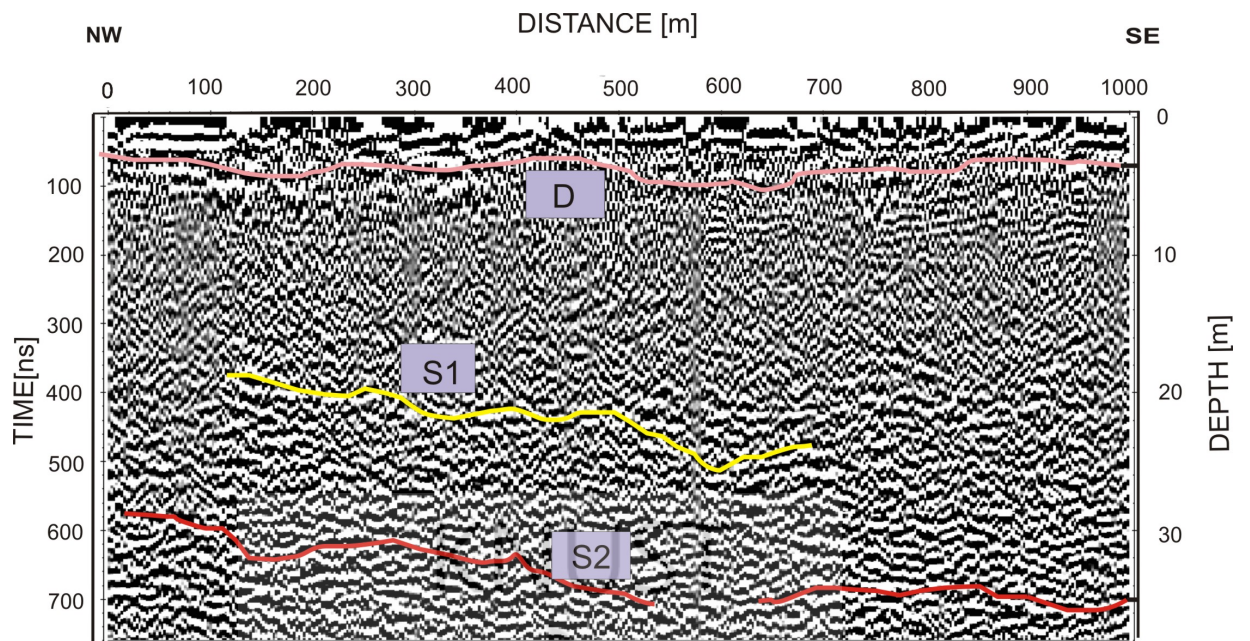


Figure A.17: Radar section of profile 2600E/3000N

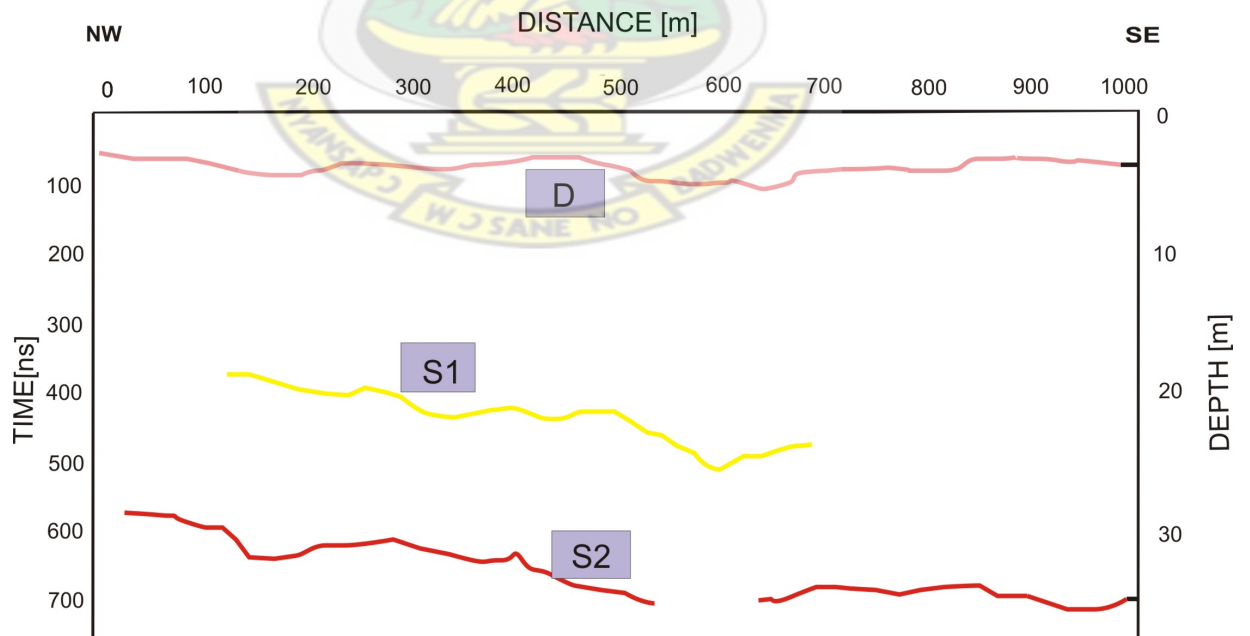


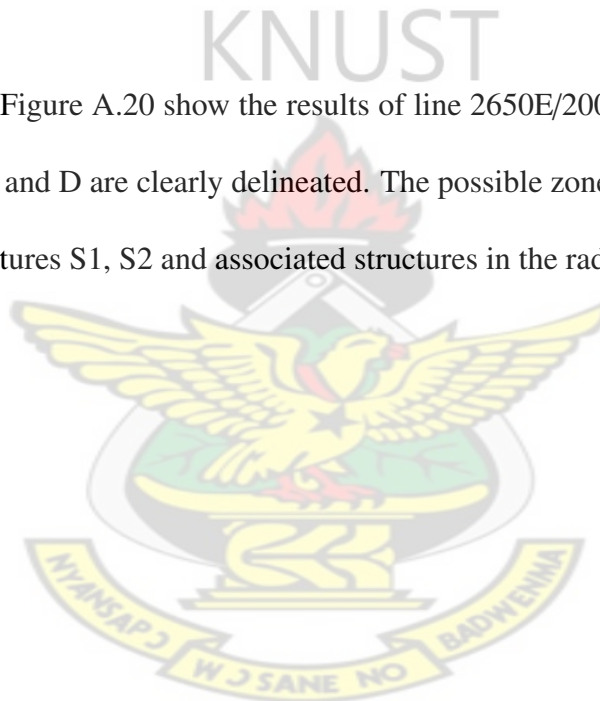
Figure A.18: Inferred structures hosting mineralization of profile 2600E/3000N

A.1.9 Traverse 12: Line 2600E/3000N

Figure A.17 and Figure A.18 illustrate the results of line 2600E/3000N. The depth range of the duracrust and saprolite transition zone is between 3 m and 5 m. S1 and S2 structures are delineated between the depth range of 20 m and 26 m, and 32 m and 37 m respectively. S1 and S2 are inferred structures possibly hosting gold mineralization.

A.1.10 Traverse 13: Line 2650E/2000N

Figure A.19 and Figure A.20 show the results of line 2650E/2000N. From Figure A.19, the structures S1, S2 and D are clearly delineated. The possible zone of mineralization could be the inferred structures S1, S2 and associated structures in the radargram.



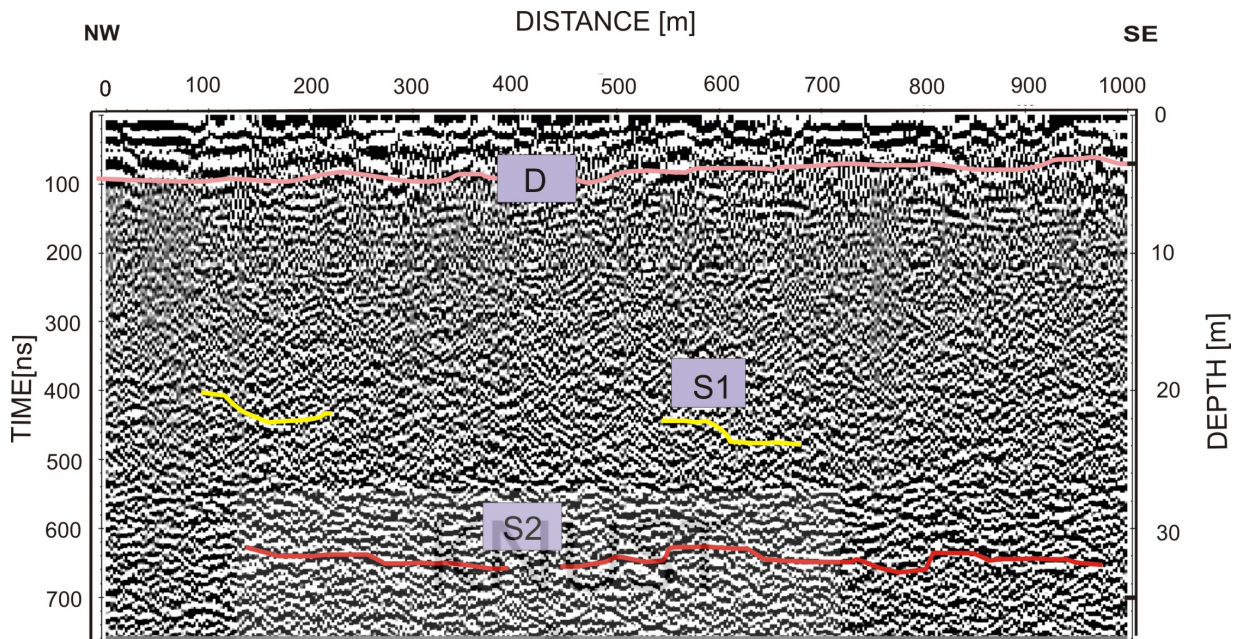


Figure A.19: Radar section of profile 2650E/2000N

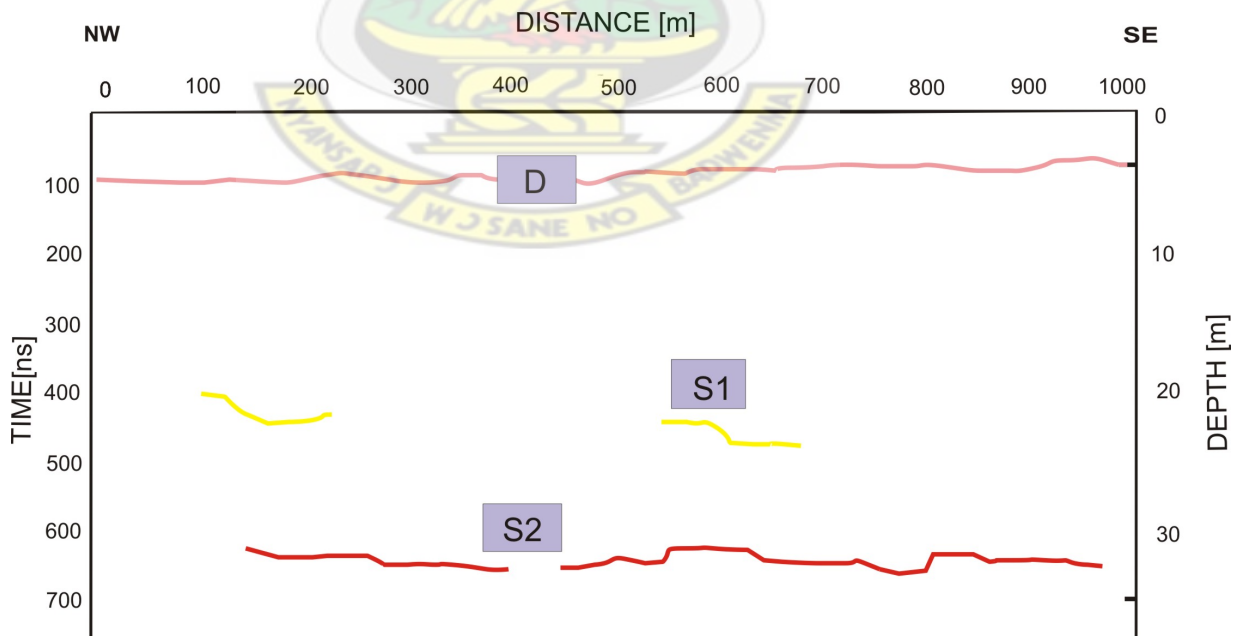


Figure A.20: Inferred structures hosting mineralization of profile 2650E/2000N

A.1.11 Traverse 14: Line 2700E/3000N

The results of line 2700E/3000N are represented in Figure A.21 and Figure A.22. The S1 structure is delineated between the depth range of 15 m and 26 m. S2 structure is also delineated between the depth range of 31 m and 37 m. Other related structures are also present . The structures are inferred to be hosting mineralization



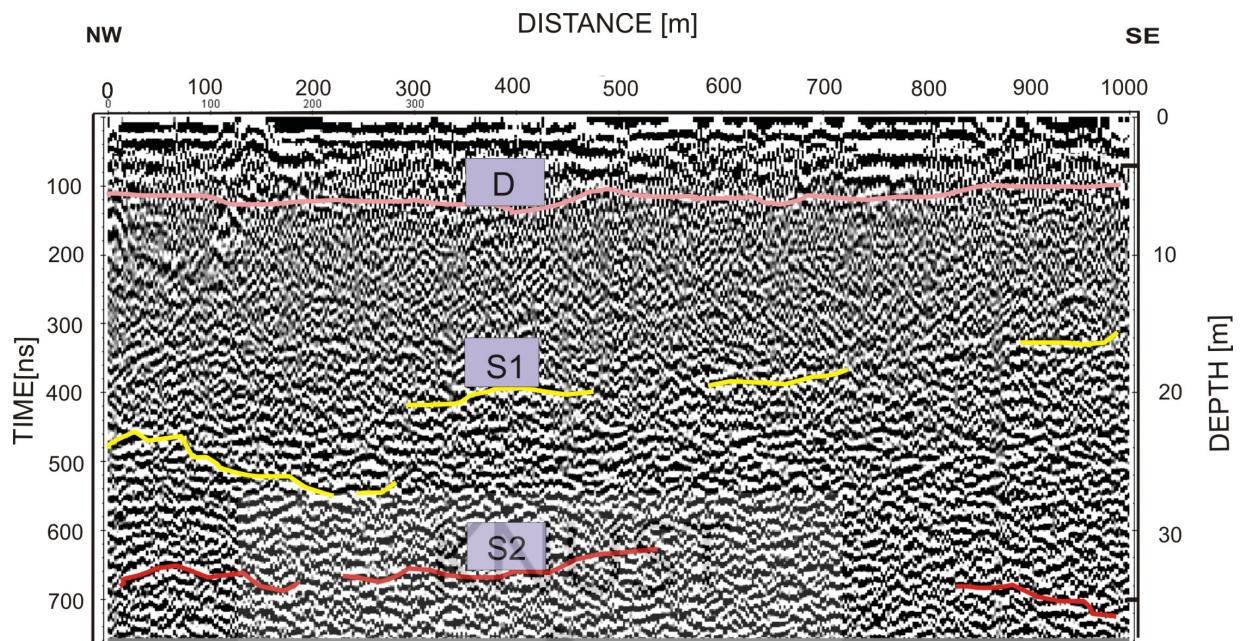


Figure A.21: Radar section of profile 2700E/3000N

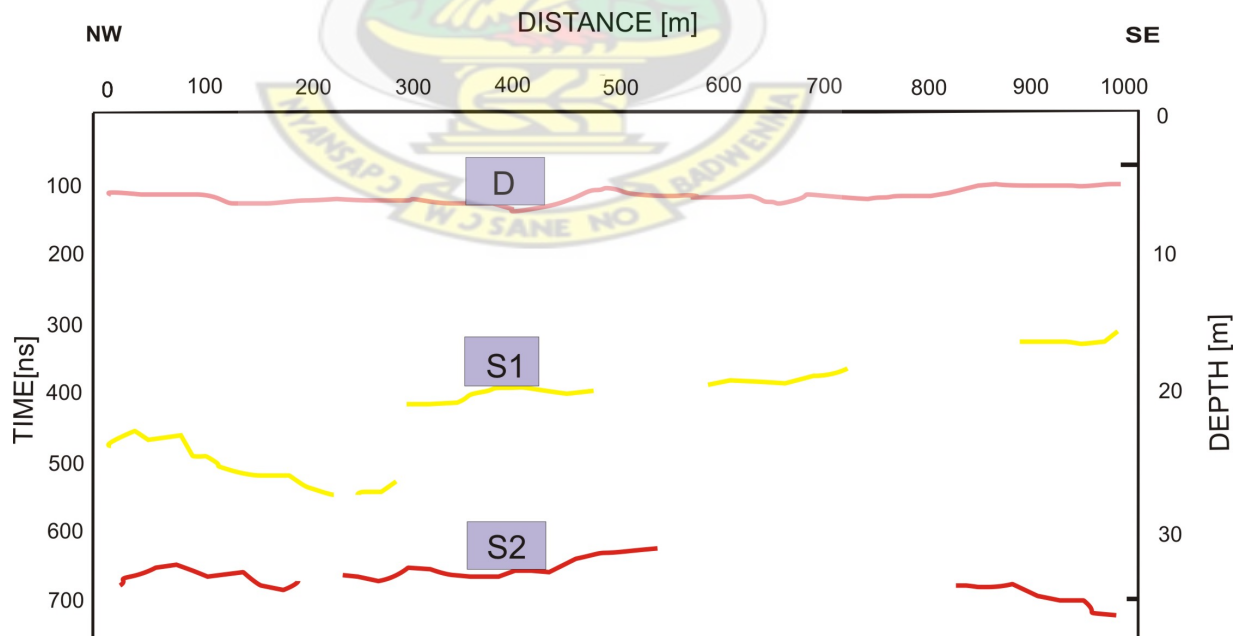


Figure A.22: Inferred structures hosting mineralization of profile 2700E/3000N

A.2 Interpretation of inferred S1 structural depth run for 25 MHz RTA

Figure A.23 shows the structures between the depth range of 15 m and 36 m. In general there is a clear evidence of possible structural deformation in the NW - SE direction which falls within the profile spacing of 300 m and 700 m. Within this range, there is a clear evidence of dipping structures labeled Z1 and Z2 which are real representation of the trend of mineralization as mapped with the resistivity and chargeability survey. These structures are inferred to be hosting gold mineralization.



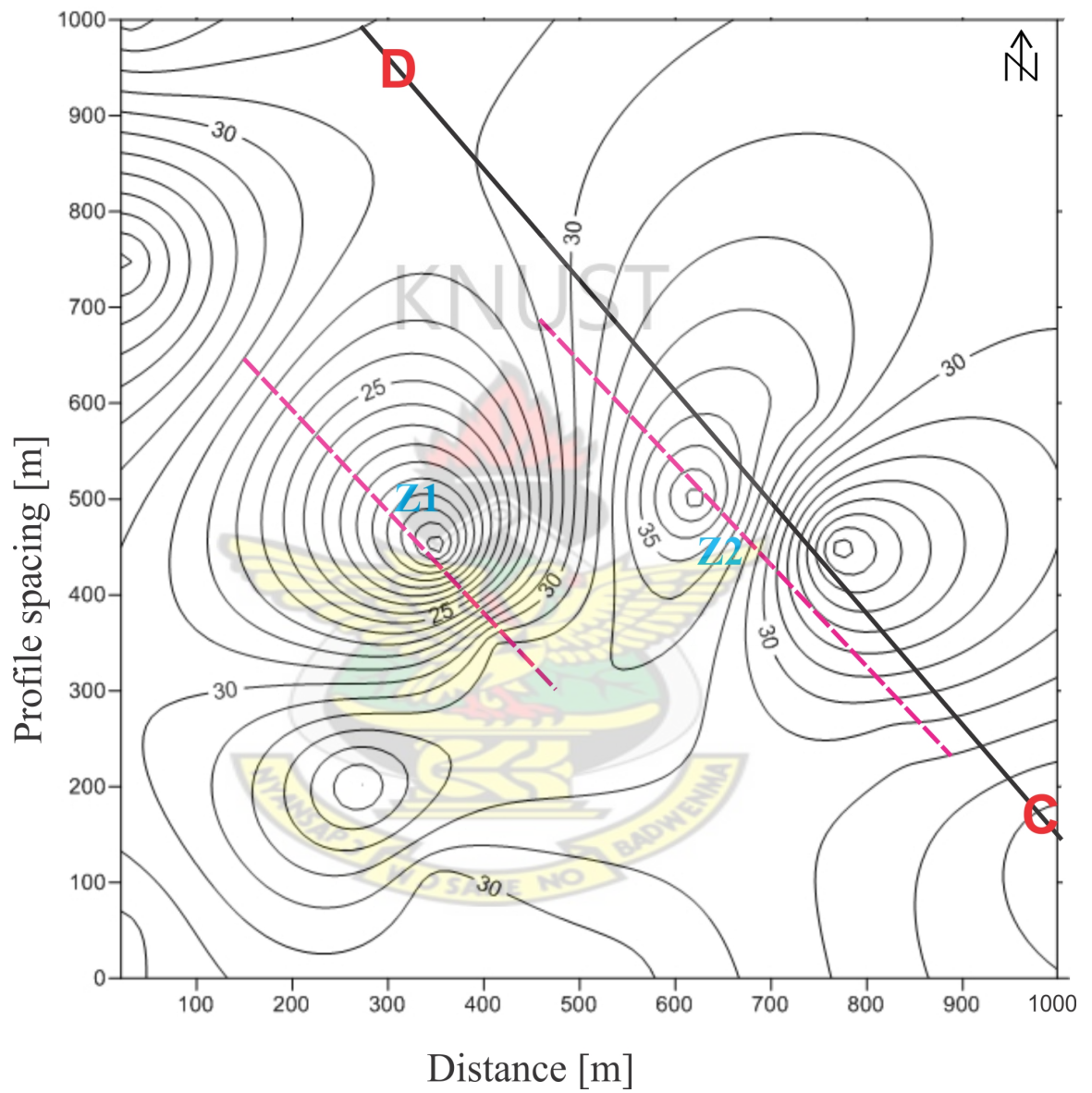


Figure A.23: A contour grid of inferred S1 structures for 25 MHz RTA

A.3 Interpretation of inferred S2 structural depth run for 50 MHz RTA

Figure A.24 presents the structural depth run between the depth range of 30.5 m and 36.5 m. Between the profile spacings of 0 m and 600 m there are some occurrences of dipping structures in the direction of NW - SE trend. These structures are marked Z1 and Z2 within the subsurface between the depths of (33.5 m and 36.5 m) and (30.5 m and 35.5 m) respectively. The Z1 inferred structure runs between the profile spacing of 0 m and 600 m. On the other hand, the Z2 structure also runs between the profile spacing of 500 m and 850 m within the subsurface. These sets of structures Z1 and Z2 clearly show the possible mineralization trend and are the potential zones of gold mineralization.

Lastly, Figure A.25 presents the structural depth run between the depth range of 21 m and 31 m. Four sets of structures were recognized in this grid. They are Z1, Z2, Z3 and Z4 showing sub-horizontal, sub-vertical, near-horizontal and vertical respectively. The structures are distributed over the entire grid and are said to be structures possibly hosting gold mineralization.

The general trend of inferred structures hosting gold mineralization for the for contour sections AB, CD, EF and GH are shown in Figures (A.26), (A.27), (A.28) and (A.29) respectively.

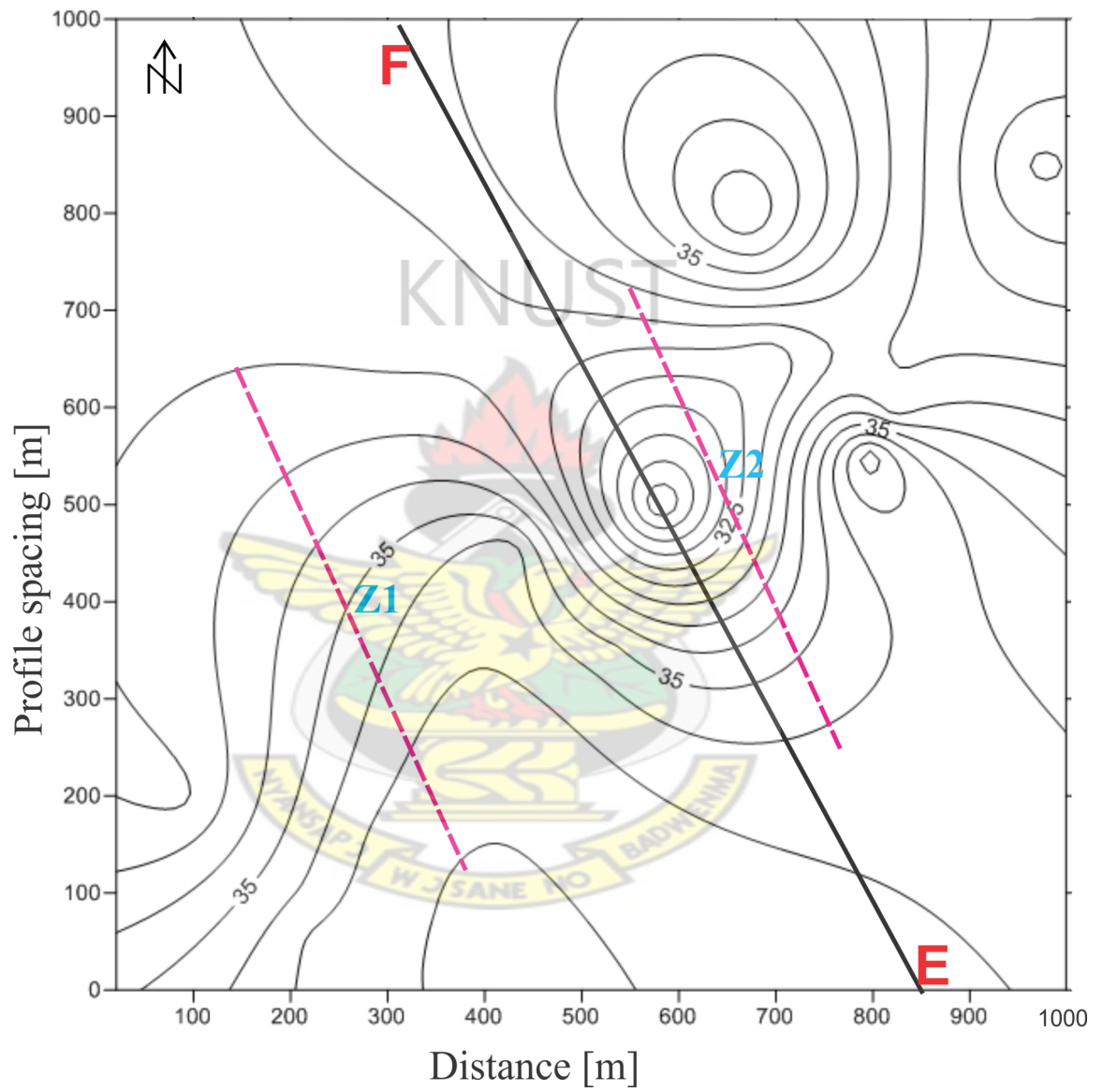


Figure A.24: A contour grid of inferred S2 structures for 50 MHz RTA

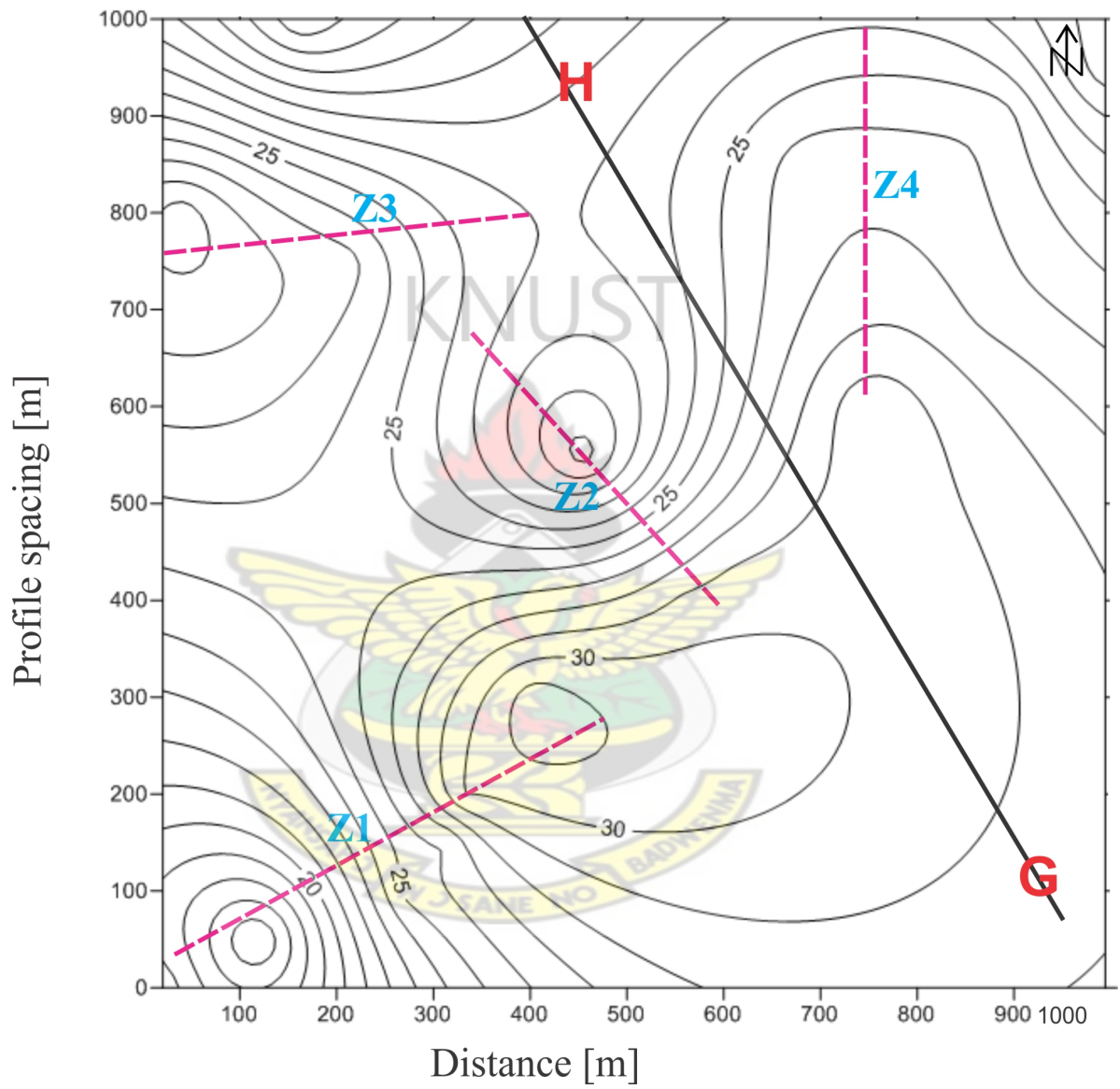


Figure A.25: A contour grid of inferred S1 structures for 50 MHz RTA

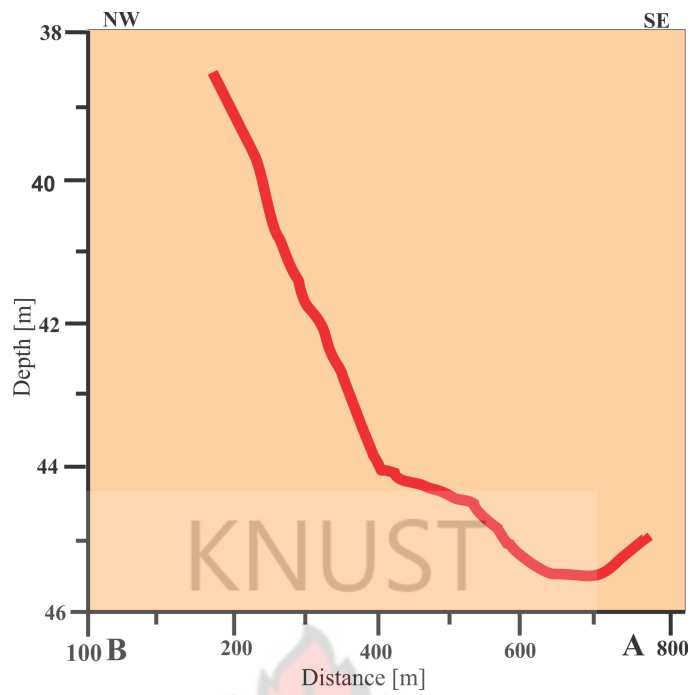


Figure A.26: Trend of an inferred S2 structure hosting gold mineralization for 25 MHz RTA

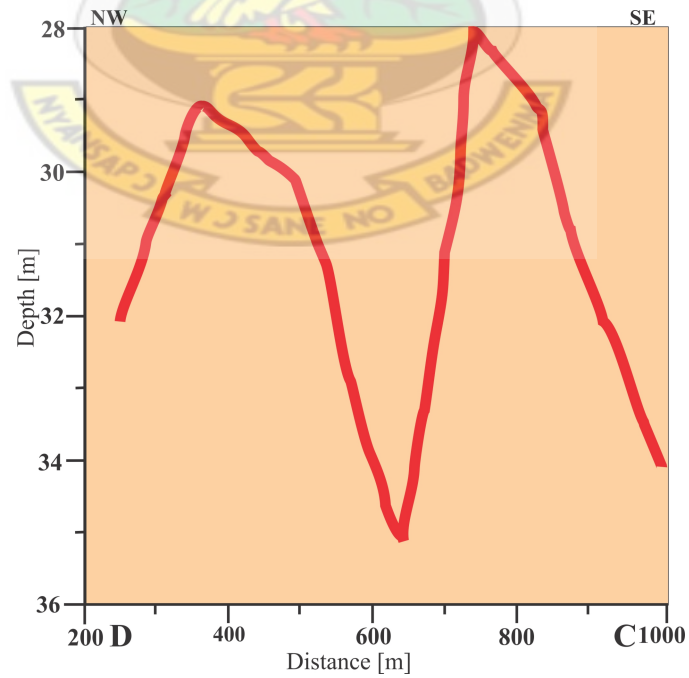


Figure A.27: Trend of an inferred S1 structure hosting gold mineralization for 25 MHz RTA

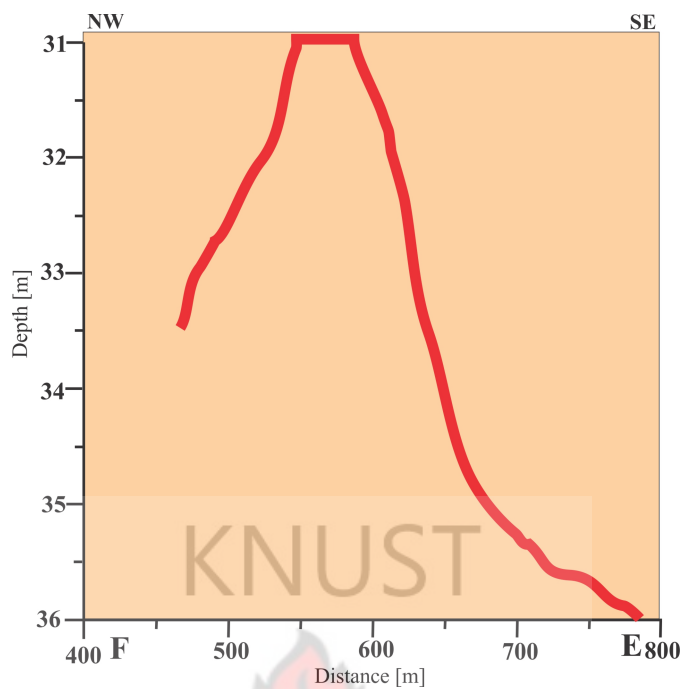


Figure A.28: Trend of an inferred S2 structure hosting gold mineralization for 50 MHz RTA

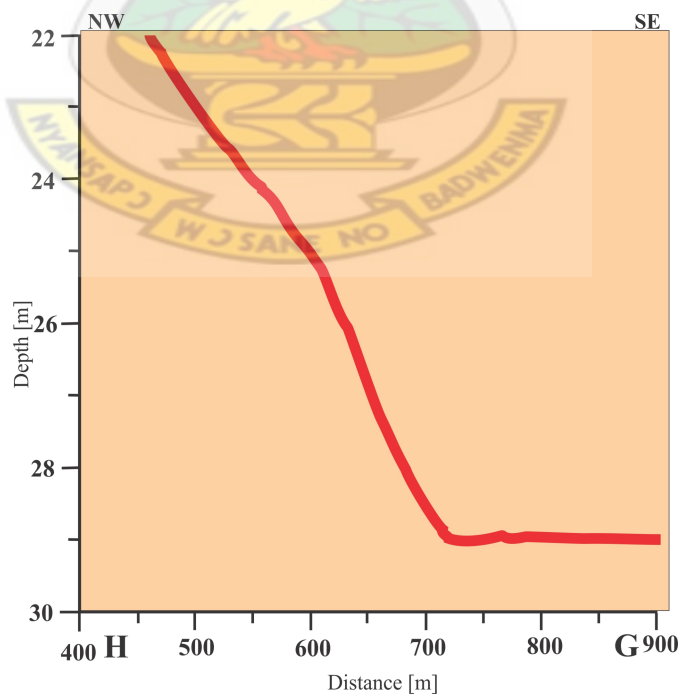


Figure A.29: Trend of an inferred S1 structure hosting gold mineralization for 50 MHz RTA

Appendix B

B.1 Used Software

- \LaTeX : typesetting and layout
- Coral Draw : graphics
- REFLEXW (Sandmeier, 2011) : The 2D processing and 2D/3D interpretation software for GPR, reflection seismics and refraction seismics.
- Golden Software Surfer 9 : contours
- Golden Software Grapher 8: plots

